

University of Louisville

## ThinkIR: The University of Louisville's Institutional Repository

---

Electronic Theses and Dissertations

---

5-2018

### Segmentation, tracking, and kinematics of lung parenchyma and lung tumors from 4D CT with application to radiation treatment planning.

Jungwon Cha  
*University of Louisville*

Follow this and additional works at: <https://ir.library.louisville.edu/etd>



Part of the [Biomedical Commons](#)

---

#### Recommended Citation

Cha, Jungwon, "Segmentation, tracking, and kinematics of lung parenchyma and lung tumors from 4D CT with application to radiation treatment planning." (2018). *Electronic Theses and Dissertations*. Paper 2938.

<https://doi.org/10.18297/etd/2938>

This Doctoral Dissertation is brought to you for free and open access by ThinkIR: The University of Louisville's Institutional Repository. It has been accepted for inclusion in Electronic Theses and Dissertations by an authorized administrator of ThinkIR: The University of Louisville's Institutional Repository. This title appears here courtesy of the author, who has retained all other copyrights. For more information, please contact [thinkir@louisville.edu](mailto:thinkir@louisville.edu).

SEGMENTATION, TRACKING, AND KINEMATICS OF LUNG  
PARENCHYMA AND LUNG TUMORS FROM 4D CT WITH  
APPLICATION TO RADIATION TREATMENT PLANNING

By

Jungwon Cha

A Dissertation

Submitted to the Faculty of the  
J. B. Speed School of Engineering of the University of Louisville  
in Partial Fulfillment of Requirements  
for the Degree of

Doctor of Philosophy in Electrical Engineering

Department of Electrical and Computer Engineering  
University of Louisville  
Louisville, Kentucky

May, 2018



SEGMENTATION, TRACKING, AND KINEMATICS OF LUNG  
PARENCHYMA AND LUNG TUMORS FROM 4D CT WITH  
APPLICATION TO RADIATION TREATMENT PLANNING

By

Jungwon Cha

A Dissertation Approved On

April 9, 2018

by the following Dissertation Committee:

---

Dissertation Director : Dr. Amir Amini

---

Dr. Jacek Zurada

---

Dr. Tamer Inanc

---

Dr. Hichem Frigui

---

Dr. Neal Dunlap

---

Dr. Brian Wang

## ACKNOWLEDGEMENTS

I am very grateful for the insightful guidance and leadership of my advisor, Dr. Amir A. Amini who has always been patient and willing to assist me with my research. In the Medical Imaging Lab, I have been provided many opportunities for joining MRI experiments and exploring the image processing research with financial support and advices, which help me prepare articles and papers and expand my research experiences.

I also would like to thank to Dr. Neal Dunlap and Dr. Brian Wang at Department of Radiation Oncology who collaborated with me and who provided clinical advices. I would also like to express my heartfelt thanks to the other members of my committee : Dr. Jacek M. Zurada, Dr. Tamer Inanc, and Dr. Hichem Frigui, for their invaluable time and great feedback on my dissertation.

I am grateful to Mehdi who collaborated in part of my research. He has taken his time to discuss and help my work be improved. In addition, I must express my gratitude to all other Medical Imaging Lab members for their supports and friendship.

I would like to thank my parents for their encouragement; without their love and supports, all this would be impossible. I want to express my sincere appreciation to my dear wife, Yongduk, who always trusts me and encourages me with her understanding. This thesis is dedicated to them.

Jungwon Cha

Louisville, Kentucky

April 2018

# ABSTRACT

## SEGMENTATION, TRACKING, AND KINEMATICS OF LUNG PARENCHYMA AND LUNG TUMORS FROM 4D CT WITH APPLICATION TO RADIATION TREATMENT PLANNING

Jungwon Cha

April 9, 2018

This thesis is concerned with development of techniques for efficient computerized analysis of 4-D CT data. The goal is to have a highly automated approach to segmentation of the lung boundary and lung nodules inside the lung. The determination of exact lung tumor location over space and time by image segmentation is an essential step to track thoracic malignancies. Accurate image segmentation helps clinical experts examine the anatomy and structure and determine the disease progress. Since 4-D CT provides structural and anatomical information during tidal breathing, we use the same data to also measure mechanical properties related to deformation of the lung tissue including Jacobian and strain at high resolutions and as a function of time. Radiation Treatment of patients with lung cancer can benefit from knowledge of these measures of regional ventilation.

Graph-cuts techniques have been popular for image segmentation since they are able to treat highly textured data via robust global optimization, avoiding local minima in graph based optimization. The graph-cuts methods have been used to extract globally optimal boundaries from images by  $s/t$  cut, with energy function based on model-specific visual cues, and useful topological constraints. The method makes N-dimensional globally optimal segmentation possible with good computational efficiency.

Even though the graph-cuts method can extract objects where there is a clear intensity

difference, segmentation of organs or tumors pose a challenge. For organ segmentation, many segmentation methods using a shape prior have been proposed. However, in the case of lung tumors, the shape varies from patient to patient, and with location. In this thesis, we use a shape prior for tumors through a training step and PCA analysis based on the Active Shape Model (ASM). The method has been tested on real patient data from the Brown Cancer Center at the University of Louisville. We performed temporal B-spline deformable registration of the 4-D CT data - this yielded 3-D deformation fields between successive respiratory phases from which measures of regional lung function were determined. During the respiratory cycle, the lung volume changes and five different lobes of the lung (two in the left and three in the right lung) show different deformation yielding different strain and Jacobian maps. In this thesis, we determine the regional lung mechanics in the Lagrangian frame of reference through different respiratory phases, for example, Phase10 to 20, Phase10 to 30, Phase10 to 40, and Phase10 to 50. Single photon emission computed tomography (SPECT) lung imaging using radioactive tracers with SPECT ventilation and SPECT perfusion imaging also provides functional information. As part of an IRB-approved study therefore, we registered the max-inhale CT volume to both  $V_{SPECT}$  and  $Q_{SPECT}$  data sets using the Demon's non-rigid registration algorithm in patient subjects. Subsequently, statistical correlation between CT ventilation images (Jacobian and strain values), with both  $V_{SPECT}$  and  $Q_{SPECT}$  was undertaken. Through statistical analysis with the Spearman's rank correlation coefficient ( $\rho$ ), we found that Jacobian values have the highest correlation with both  $V_{SPECT}$  and  $Q_{SPECT}$ .

# TABLE OF CONTENTS

LIST OF FIGURES	ix
LIST OF TABLES	xiv
<b>1 INTRODUCTION</b>	<b>1</b>
1.1 Lung Anatomy and Physiology . . . . .	1
1.2 Lung Cancer . . . . .	4
1.2.1 Nodule vs. Tumor . . . . .	4
1.2.2 Lung Cancer . . . . .	4
1.3 4-D CT Lung Imaging . . . . .	5
1.4 Single photon emission computed tomography (SPECT) . . . . .	7
1.5 Organization of the thesis . . . . .	7
<b>2 REVIEW OF LITERATURE ON PULMONARY IMAGE PROCESSING</b>	<b>10</b>
2.1 Pulmonary Image Segmentation . . . . .	10
2.1.1 Gray-level thresholding methods . . . . .	10
2.1.2 Region-based methods . . . . .	11
2.1.3 Shape-based methods . . . . .	12
2.2 Pulmonary Image motion tracking . . . . .	12
2.2.1 The transformation model . . . . .	14
2.2.2 The similarity measure . . . . .	18
<b>3 GRAPH-CUTS SEGMENTATION</b>	<b>20</b>
3.1 Introduction . . . . .	20
3.2 The Basic Concepts . . . . .	21
3.2.1 Graph Construction . . . . .	21
3.2.2 Energy Function . . . . .	22

3.3	Max-flow Algorithm . . . . .	24
3.3.1	Augmenting Path Algorithm (Ford-Fulkerson) . . . . .	24
3.3.2	Boykov's Maximum Flow = Minimum Cut algorithm . . . . .	27
3.4	Advantages of Graph-cuts . . . . .	30
3.5	3-D Lung Boundary Segmentation with Graph-cuts . . . . .	35
3.5.1	Lung segmentation with Graph-cuts . . . . .	35
3.5.2	Analysis of Parameter Sensitivities for Graph-cuts segmentation of Lung CT . . . . .	35
3.5.3	3-D Segmentation with Graph-cuts on the Lung CT image . . .	37
3.6	3-D tumor segmentation via Graph-cut Optimization Including Prior Trained Shape . . . . .	43
3.6.1	Active Shape Model (ASM) with Signed Distance Function . . .	45
3.6.2	3-D tumor segmentation with Prior Trained Shape . . . . .	48
3.7	4-D tumor segmentation via Graph-cut Optimization Including Prior Trained Shape and Motion . . . . .	51
3.7.1	Motion estimation by Optical Flow . . . . .	51
3.7.2	4-D Lung nodule segmentation . . . . .	53
3.7.3	Testing and Training Data . . . . .	53
3.7.4	Results of 4-D Lung Nodule Segmentation . . . . .	55
<b>4</b>	<b>STATISTICAL CORRELATION OF CT VENTILATION IMAGES WITH V/Q SPECT</b>	<b>68</b>
4.1	Introduction . . . . .	68
4.2	Deformable image registration : B-spline method . . . . .	69
4.3	CT Ventilation Images from Lung Deformation . . . . .	74
4.3.1	Measure of regional functions . . . . .	74
4.3.2	Data . . . . .	76
4.3.3	Results . . . . .	76

4.4	Statistical correlation of CT ventilation imaging and V/Q SPECT in patients with lung cancer . . . . .	82
4.4.1	Co-Registration of CT and SPECT . . . . .	82
4.4.2	Correlation between CT Ventilation Images and SPECT data . .	83
4.4.3	Data . . . . .	83
4.4.4	Results . . . . .	83
<b>5</b>	<b>CONCLUSIONS</b>	<b>89</b>
5.1	Motivations . . . . .	89
5.2	Contributions . . . . .	90
5.3	Future Research . . . . .	91
	REFERENCES	93
	CURRICULUM VITAE	111

## LIST OF FIGURES

1	The anatomy of the lungs [127]. . . . .	2
2	Static lung volumes and capacities based on a spirogram [3]. . . . .	3
3	Lung cancer incidence rates for United States 2008–2012 [107]. . . . .	5
4	Retrospective 4-D CT Lung Imaging. Images acquired with the aid of respiratory waveform from RPM respiratory gating system in order to bin the image data into phases. Figure taken from [110]. . . . .	6
5	Lung Ventilation-Perfusion Scan. First row : ventilation scan which shows uniform ventilation in both lungs. Second row : Perfusion scan. Representative SPECT images in patient with multiple pulmonary embolism. Several mismatched defects are evident (arrows). Figure taken from [118]. . . . .	8
6	Image registration is the task of finding a spatial transform $T$ mapping one image into another. . . . .	13
7	Graph construction . . . . .	22
8	Ford-Fulkerson Algorithm[105] . . . . .	26
9	Boykov Algorithm, Flow Chart(1) [105] . . . . .	32
10	Boykov Algorithm, Flow Chart(2) [105] . . . . .	33
11	Boykov Algorithm, Flow Chart(3) [105] . . . . .	34
12	Boykov Algorithm, Flow Chart(4)[105] . . . . .	35
13	Results of 3-D segmentation of Patient01. (a) Segmented image with two labels $K = 5, \lambda = 0.5, c = 1.5$ (b) Binary segmentation results with artifact due to bad parameters selection $K = 5, \lambda = 0.1, c = 1.5$ , (e) Binary segmentation results with artifact due to bad parameters selection $K = 5, \lambda = 0.01, c = 1.5$ [32]. . . . .	38

14	The histogram for the intensity range of seed points. The blue line plot represents the object and the red dot plot represents the background. . . . .	39
15	2-D axial and coronal slices of the lung . . . . .	40
16	The selection of seed points. Yellow circles: seed points for object (inside the lung), red crosses: Seed points for background (outside the lung). . . . .	41
17	The result of 3-D segmentation with binary graph-cuts method [32] . . . . .	42
18	Lung boundary embedded as the zero level set of signed distance function . . . . .	46
19	Deformations of the mean shape generated by varying the weight corresponding to the first four primary eigenvectors. . . . .	49
20	3-D visualization of nodule mean shape, determined from over 500+ training images from the LIDC Cancer Imaging Archive Data Sets [7]. . . . .	50
21	Visualization of the motion fields on 2-D axial slices. (a) Motion fields from phase 10 to phase 20 displayed at phase10, (b) from phase 20 to phase 30 at phase 20, (c) from phase 30 to phase 40 at phase 30, (d) from phase 40 to phase 50 at phase 40. . . . .	52
22	(a) 2-D axial slice and (b) 2-D coronal slice from 3-D image volume for phase 10 of data from a patient with a well-circumscribed nodule. The cross indicates the center of nodule which was manually selected. . . . .	56
23	Iterative segmentation of nodule in a single phase. (a) First row: refined mean shapes, second row: segmented nodule utilizing mean shapes from the first row, (b) Plot of the energy function as a function of iterations. . . . .	57
24	The motion field from the phase 10 to the phase 20 on the cropped 2-D axial slice on the phase 10, and the mean shape and the warped mean shape. . . . .	58
25	3-D visualization of well-circumscribed or vascularized nodules for nine patients through five phases. . . . .	59

26	Box plot of the volume of well-circumscribed or vascularized nodules for the nine patients. The bar in the box plot represents the mean volume through five volumetric phases. (a) Results from the proposed method, (b) Ground truth. . . . .	60
27	Comparison of nodule sizes in 2-D coronal slice between the segmentation result with the ground truth for Patient02. Nodule boundaries are delineated by red lines. The size of the nodules in patient02 from the ground truth is bigger than the same nodules from our segmentation results. (a) Results from the proposed method, (b) Ground truth. . . . .	61
28	Box plot for the Dice Similarity Coefficient of 4-D segmentation of well-circumscribed or vascularized nodules for nine patients. For each patient, the box plot represents the DSC for five phases through time. . . . .	62
29	2-D axial slice having a nodule embedded in surrounding tissues. The arrow indicates the nodule. . . . .	62
30	Comparison in 2-D between the segmentation result with shape prior (b) and without shape prior (c). (a) shows a cropped image slice with ground truth boundary. . . . .	63
31	Segmentation and shape prior evolution for a juxtapleural nodule. Columns 1-6 show iterations 1, 2, 6, 7, 10 and the final result in iteration 12 respectively. First row shows segmentation in 3-D and second row shows the zero level set of the signed distance function representation for the refined mean shape. The shape prior for iteration 1 is the mean shape while for subsequent iterations the shape prior used in the iterative graph cuts segmentation is the refined shape prior from the previous iteration. Please see description following Eq. (26) in the text. The third row plots the change in the Dice Similarity Coefficient through iterations showing effectiveness of the adaptive refinement of the shape prior. . . . .	64
32	3-D visualization of juxtapleural nodules for eight patients through five phases.	65

33	Box plot of the volume of juxtapleural nodules for eight patients. The bar in the box plot represents the mean volume through five volumetric phases. (a) Results from the proposed method, (b) Ground truth. . . . .	66
34	Box plot for the Dice Similarity Coefficient of 4-D segmentation of juxtapleural nodules for eight patients. For each patient, the box plot represents the DSC for five phases through time. . . . .	67
35	The range of polynomial basis functions. (a) degree $d = 0$ , (b) $d = 1$ , (c) $d = 2$ , (d) $d = 3$ . . . . .	71
36	Strain tensor ellipsoid. . . . .	75
37	The sectioning of lung volume to left upper lobe (LUL), left lower lobe (LLL), right upper lobe (RUL), right middle lobe (RML), and right lower lobe (RLL). Ideally, this should be done based on lung fissures and this was done as a rough approximation. . . . .	77
38	Average Jacobian measure over five lung lobes through respiratory phases, always relative to phase 10. (a) patient 01, (b) patient 02, (c) patient 03, (d) patient 04, (e) patient 05, (f) Average over 22 patients. . . . .	78
39	Average maximum strain value $\lambda_1$ over five lung lobes through respiratory phases, always relative to phase 10. (a) patient 01, (b) patient 02, (c) patient 03, (d) patient 04, (e) patient 05, (f) Average over 22 patients. . . . .	79
40	Average medium strain value $\lambda_1$ over five lung lobes through respiratory phases, always relative to phase 10. (a) patient 01, (b) patient 02, (c) patient 03, (d) patient 04, (e) patient 05, (f) Average over 22 patients. . . . .	80
41	Average minimum strain value $\lambda_1$ over five lung lobes through respiratory phases, always relative to phase 10. (a) patient 01, (b) patient 02, (c) patient 03, (d) patient 04, (e) patient 05, (f) Average over 22 patients. . . . .	81

42	2-D mid-coronal slices of CT Ventilation image volumes computed between Phase10 and Phase50 of 4-D lung CT data, compared with registered SPECT ventilation and perfusion. (a) The calculated Jacobian image, (b) the maximum principal strain image, (c) the medium principal strain image, (d) the minimum principal strain image, (e) SPECT ventilation image, (f) SPECT perfusion image . . . . .	84
43	The box plot of the Spearman's correlation coefficient ( $\rho$ ) between $V_{SPECT}$ and both Jacobian and principal strain values from 4-D CT data for all 11 lung cancer patients. . . . .	85
44	The box plot of the Spearman's correlation coefficient ( $\rho$ ) between $Q_{SPECT}$ and both Jacobian and principal strain values from 4-D CT data for all 11 lung cancer patients. . . . .	85

## LIST OF TABLES

1	Edge weights in graph-cuts segmentation [17] . . . . .	24
2	The parameter sensitivity for 3-D lung image segmentation [32] . . . . .	36
3	Validation results from applying 3-D graph-cuts segmentation to lung boundaries in four 3-D CT data sets, comparing automated segmentation with ground truth [32]. . . . .	43
4	The target registration error (TRE) of B-spline registration for POPI model and DIR-lab 4-D CT data (Case01 - Case10). TRE is averaged over all slices and all frames. Although more sophisticated methods as reported in EMPIRE10 Challenge [1] produce more accurate results (with the best approaches improving these TREs by $\sim 0.5\text{mm}$ ), the availability of code, ease of application and speed makes use of B-spline registration compelling. . . . .	86
5	The Spearman’s correlation coefficient ( $\rho$ ) between $V_{SPECT}$ and both Jacobian and principal strain values from 4-D CT data for all 11 lung cancer patients. The p-value for all cases is ‘ $< 0.005$ ’. . . . .	87
6	The Spearman’s correlation coefficient ( $\rho$ ) between $Q_{SPECT}$ and principal strain values from 4-D CT data for all 11 lung cancer patients. The p-value for all cases is ‘ $< 0.005$ ’. . . . .	88

# CHAPTER 1

## INTRODUCTION

### 1.1 Lung Anatomy and Physiology

The lung has a spongy texture weighing about  $500 \sim 600g$  which is filled with air, and protected by ribcage bones. The anatomy of lungs is shown in Figure 1. The lungs run as respiratory organs which bring oxygen( $O_2$ ) through the respiratory tract into the body, and remove and discharge carbon dioxide( $CO_2$ ). The trachea carries out inhalation of air into the lungs through its two hollow tubular branches (left and right), called bronchi. The bronchi themselves split into smaller branches which are called bronchioles. At the end of the smallest bronchioles are the smallest air sacs called alveoli. At the alveoli level,  $O_2$  from the air is absorbed into the blood and  $CO_2$  which is extracted from the venous blood to the alveoli is exhaled. During inhalation and the exhalation, the most important muscle is the diaphragm. The diaphragm is located under the lungs and separates lungs from the organs below, such as the stomach, liver, etc. The movement of the lungs is like balloons. When the diaphragm moves down, the ribs inflate outward to help lungs get the air in. Moreover, during exhalation, the diaphragm moves up to the original position and the air leaves the lungs. For breathing, in addition to the diaphragm, other muscles called the scalene muscles are used. The Scalene muscles are located at the neck level to the upper ribs and protect the cervical vertebra.

The lungs are covered by a thin membrane called the pleura. There are two kinds of pleura: ‘Parietal pleura’ which is attached to the chest wall, and ‘Visceral pleura’ which covers the lungs and separates the lungs into five lobes (three on the right and two on the left). These act as a lubricant allowing the lungs to slip smoothly on the chest wall and

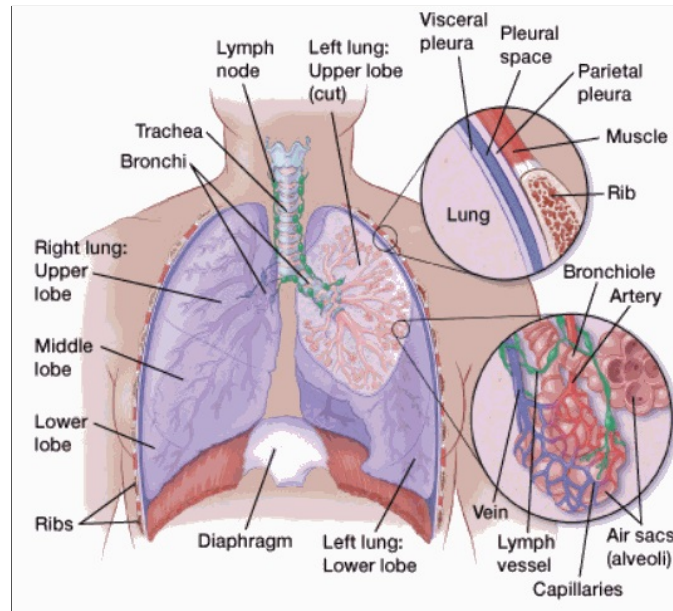


Figure 1. The anatomy of the lungs [127].

neighboring lobes during breathing. Each lung has an oblique fissure that partitions the upper lobes to the lower lobes and the right lung has another horizontal fissure separating the upper lobe from the middle lobe. Thus, the left lung has two lobes; left upper lobe (LUL) and left lower lobe (LLL) and the right lung has three lobes; right upper lobe (RUL), right middle lobe (RML), and right lower lobe (RLL).

Breathing occurs in defined cycles as the chest wall and the lungs move. This breathing cycle is defined by the change with the volumetrics of the lung which is occupied by air. Clearly the size of lungs vary with the degree of respiration, the ethnicity, the gender, and the age of the subject and in certain cases, the disease process. Thus, accurate pulmonary function testing leads to diagnosing pulmonary diseases. The most widely used pulmonary function test is the Spirometry. In order to describe lung volumes from the results of spirometry, the following terms are used and are also illustrated in Figure 2.

- \* Tidal Volume (TV): The volume of air breathed in and out during breathing.
- \* Inspiratory Reserve Volume (IRV): The additional volume of air that can be inhaled with maximum effort after normal inhalation.

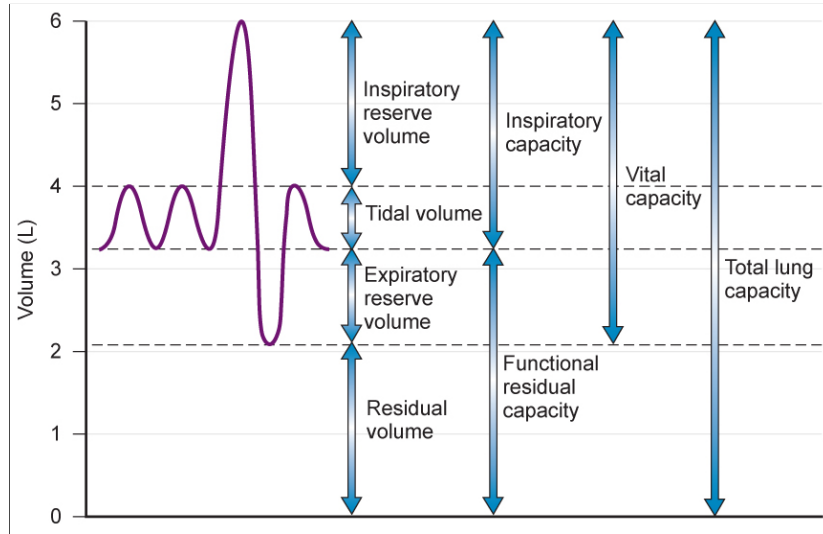


Figure 2. Static lung volumes and capacities based on a spirogram [3].

- \* Expiratory Reserve Volume (ERV): The additional volume of air that can be exhaled with maximum effort after normal exhalation.
- \* Vital Capacity (VC): The total volume of air that can be exhaled after maximum inhalation:  $= TV + IRV + ERV$
- \* Residual Volume (RV): The volume of air remaining in the lungs after maximum exhalation as the lungs cannot be emptied completely.
- \* Total Lung Capacity (TLC): The volume of the lung after maximal inhalation:  $= VC + RV$
- \* Minute Ventilation: The volume of air breathed in 1 minute:  $(TV)(\text{breaths/minute})$

The basic idea of spirometry is an expiratory maneuver, which measures exhaled air but does not measure residual volume or total lung capacity. Vital capacity is a good measure of lung volume in restrictive disorders such as pleural tumors, pulmonary fibrosis, and diaphragm weakness in which it will be reduced.

## 1.2 Lung Cancer

### 1.2.1 Nodule vs. Tumor

A nodule is called a “spot on the lung,” or “coin lesion” seen on an X-ray or computed tomography (CT) scan. A pulmonary nodule is a small round or oval-shaped growth in the lung. Pulmonary nodules are smaller than three centimeters in diameter, which is completely surrounded by pulmonary parenchyma and is not associated with adenopathy, atelectasis, or pleural effusion[109, 133]. If a nodule is larger than three centimeters in diameter, it is more likely to be a tumor than a nodule, and will be treated as malignancies and treated clinically. The nodule can occur as solitary or multiple depending on how many nodules are observed. The pulmonary nodules can be categorized into benign tumors or malignant tumors after pathologic diagnosis, which should be done to rule out cancer. Benign tumors are rarely life threatening, do not spread to other organs of the body and may be left untreated. On the other hand, malignant tumors can be life threatening, can metastasize to other organs and are often removed but may grow again. Most solitary pulmonary nodules are benign. In addition to size of nodule, other factors can help in the differential diagnosis, for example, that patients are younger than 40, they are nonsmokers or that calcium is present in the nodule. The benign pulmonary nodule may be an active inflammation or scar tissue caused by inflammation due to diseases or infections. Despite the fact that most of them are benign, nodules need to be regarded as early stage lung cancer since in time, 35% of solitary pulmonary nodules become malignant[131]. Thus, earlier detection of even small nodules may reduce mortality increase patients’ survival.

### 1.2.2 Lung Cancer

Lung cancer is the major cause of cancer death in the United States, constituting more deaths annually than breast, colon, ovarian and prostate cancers combined. According to statistics[64], the survival rates from lung cancer at 5 years is 17.8% lower than other kinds

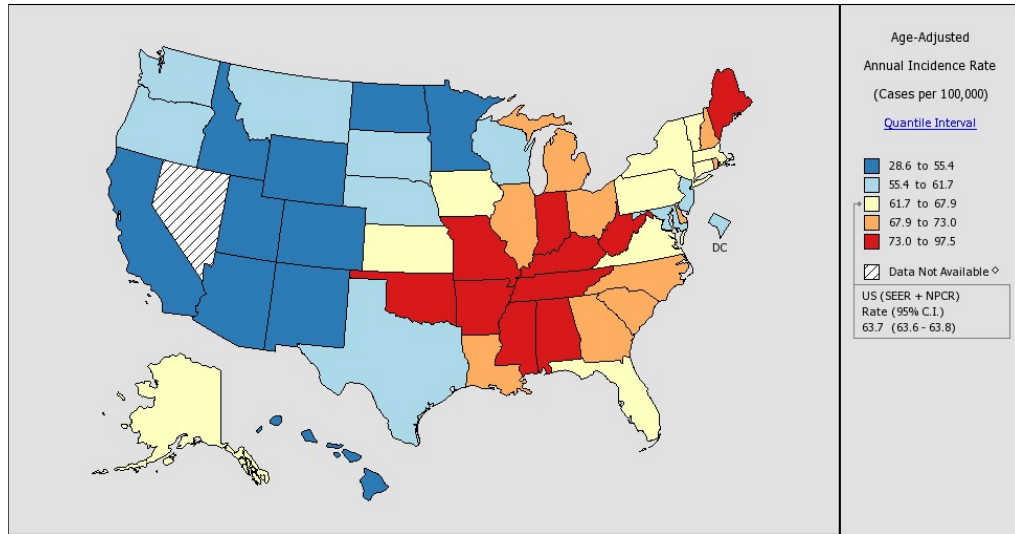


Figure 3. Lung cancer incidence rates for United States 2008–2012 [107].

of cancers, while the survival rates is 54% for cases without any metastasis. Moreover, only 15% of lung cancer cases are diagnosed at an early stage. In 2015, more than 221,200 cases of lung cancer were expected to be diagnosed. In 2011, Kentucky had the highest incidence of lung cancer rates at 112.2 males per 100,000 of population and 79.3 females per 100,000 of population. Utah had the lowest lung cancer incidence rates at 34.5 males per 100,000 of population and 25.0 females per 100,000 population. The incidence rates map of lung cancer for United States is shown in Figure 3. These rates are intimately related to prevalence of smoking.

### 1.3 4-D CT Lung Imaging

Respiratory lung motion can cause severe distortion of anatomical position in free breathing CT scanning. Distortions along the axis of motion could either lengthen or shorten the target. In addition to shape distortion, the center of the imaged target can be misplaced. This distortion can let radiologists set up larger margins than the actual lesion causing radiation dose to even healthy surrounding tissues during radiotherapy planning. In order to mitigate respiratory motion during CT scans, other scanning strategies are used. For example, breath-held CT requires volunteers to hold their breath during acquisition resulting

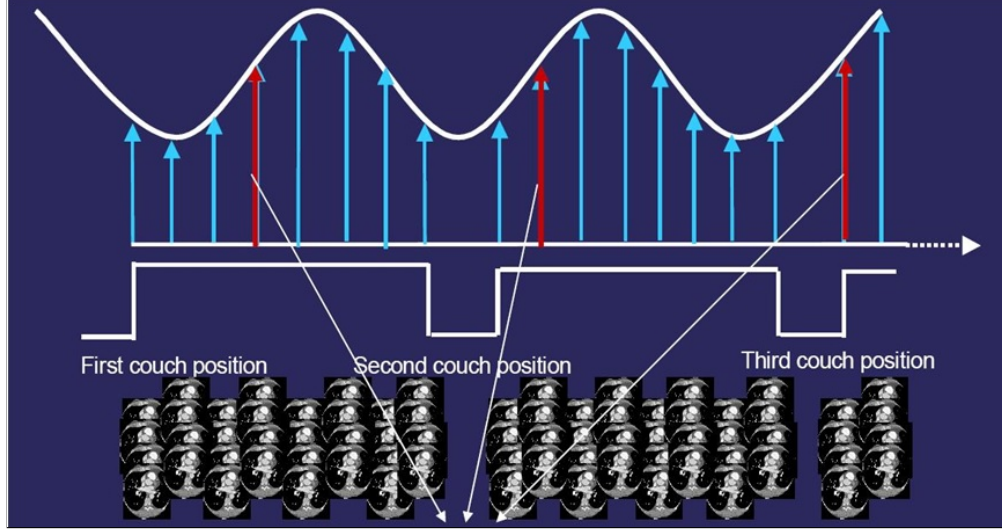


Figure 4. Retrospective 4-D CT Lung Imaging. Images acquired with the aid of respiratory waveform from RPM respiratory gating system in order to bin the image data into phases. Figure taken from [110].

in significantly reduced noise and motion artifacts. Even though breath-held CT images are relatively clean, but there is significantly less information available in them. Also the gated CT scan acquires CT images at only one phase, but the acquisition times is around five-times longer. 4-D CT performs 3-D scans at multiple phases.

4-D CT imaging [45, 75, 117] is the sequential acquisition of 3-D CT image volumes over consecutive phases of a respiratory cycle acquired during normal tidal breathing. During scans, the breathing index associated with each 3-D CT image is recorded by an external tracking device such as the real-time position management (RPM) [132]. RPM uses an infrared tracking camera and a reflective marker which is placed on the patient, and measures the patients respiratory pattern and motion. Each 3-D image volumes acquired at each location over the entire lung is sorted into corresponding respiratory phases, as shown in Figure 5.

Most 4-D CT lung imaging are constructed with ten respiratory phases which are typically referred to phases P00, P10, ..., P80, P90, where phase P00 corresponds to end-inhale which has maximum lung volume and phase P50 corresponds to end-exhale which has minimum lung volume. Through these phases, imaging provides a movie of the anatom-

ical motion of the lungs which can be used for radiation treatment planning and tumor targeting[91, 140].

#### **1.4 Single photon emission computed tomography (SPECT)**

Radiation treatment of patients with lung cancer can benefit from knowledge of regional lung function and the prevalent lung imaging method to achieve this is SPECT. SPECT is useful for measurement of perfusion when using intravenously injected radiotracers and ventilation when using aerosolized radiotracers. The images are acquired for these study by a gamma camera. In clinical SPECT studies, respiratory motion limits the performance of pulmonary region studies. Respiration affects SPECT acquisition since SPECT scans are acquired for longer time than the CT scans and respiration can cause image blurring along the axis of motion due to the fact that SPECT data are averaged over many respiratory cycles. The ventilation imaging detects the air flow to deliver to all parts of the lungs, while the perfusion imaging represents that the blood flow circulates the vessels in the lungs. Ventilation/Perfusion Lung SPECT imaging (better known as V/Q scans) is used to check for blood flow ventilation mismatch in the lung such as for example in the diagnosis of pulmonary emboli. In the case of patients with lung cancer, our goal is to develop machinery that uses CT directly to produce ventilation images. The advantage is that this information in CT is regional, at high resolution, and is obtained in a number of distinct respiratory phases.

#### **1.5 Organization of the thesis**

The rest of this thesis is organized as follows:

Chapter 2 provides a review of literature on Pulmonary Image processing. We review pulmonary image segmentation and pulmonary image motion tracking via deformable image registration.

Chapter 3 introduces the basic concepts of graph-cuts segmentation. We describe the

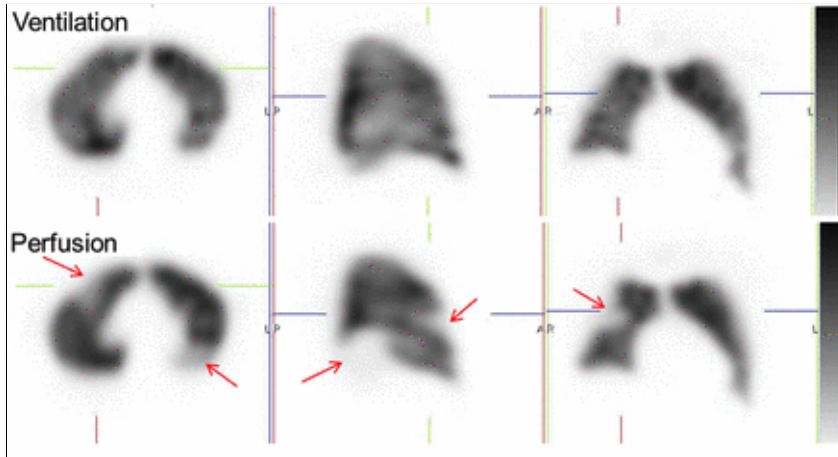


Figure 5. Lung Ventilation-Perfusion Scan. First row : ventilation scan which shows uniform ventilation in both lungs. Second row : Perfusion scan. Representative SPECT images in patient with multiple pulmonary embolism. Several mismatched defects are evident (arrows). Figure taken from [118].

most popular graph-cuts algorithm, i.e., the Max-flow/Min-cut algorithm, providing details on how the algorithm works for image segmentation. Subsequently, we describe segmentation of 3-D lung CT images with graph-cuts and report how to set up the parameters to obtain accurate results. We also show results of binary segmentation for extracting the lung boundary.

Secondly, we describe a framework for 3-D lung tumor segmentation via graph-cuts optimization which includes prior trained shapes. We discuss how prior shape information obtained by Active Shape Model (ASM) with signed distance function can be used for lung tumor segmentation.

Lastly, this chapter extends the method to 4-D where in addition to grey value information in 3-D, lung motion tracking via the optical flow method is incorporated for spatio-temporal segmentation of lung tumors, whole lung borders, and the surrounding tissue.

Chapter 4 discusses extraction of kinematic properties related to deformation of the lung tissue including Jacobian and Lagrangian strain of deformation as a function of time from 4-D lung CT. We perform B-spline deformable registration to obtain voxel-wise estimates of motion through out the lung parenchyma at different phases, for example, Phase

10 to 20 , Phase 10 to 30, Phase 10 to 40, and Phase 10 to 50.

During the respiratory cycle, the lung volume changes and five different fissures of the lung shows different deformation yielding different strain and Jacobian maps. In this work, we analyze the aspect of regional mechanics from the lung deformation over five lung lobes through different respiratory phases.

To validate CT ventilation images, we register the max-inhale CT volume to both  $V_{SPECT}$  and  $Q_{SPECT}$  data sets. Subsequently, results from statistical correlation between CT ventilation images, Jacobian and strain values, with both  $V_{SPECT}$  and  $Q_{SPECT}$  is illustrated.

Finally, Chapter 5 provides concluding remarks and directions for future research.

## CHAPTER 2

### REVIEW OF LITERATURE ON PULMONARY IMAGE PROCESSING

#### 2.1 Pulmonary Image Segmentation

Image segmentation is a critical step for medical image analysis, which often is the preprocessing step of medical imaging tasks. Segmentation can extract the organ of interest, or the tumor lesion in the organ. In this section, we focus on the lung segmentation, which includes finding the boundary of the lungs themselves, or with nodules in the lung. The lung image segmentation has been researched using several effective methods. Those methods can be categorized as follows. For example, gray-level thresholding, region-based, shape-based, path-based methods, etc. In CT scans, the lung which is occupied with air mostly shows up with very low intensities (dark regions) while the surrounding tissue, for example, the vessel, the muscles, the bones, and the fat display higher intensities (brighter regions). This contrast between the lung and surrounding tissues provides the basic idea for whole lung segmentation methods.

##### 2.1.1 Gray-level thresholding methods

One segmentation method using this scheme is gray-level thresholding [6, 65]. Hu et al.[65] used optimal thresholding to accommodate the small variations in expected tissue intensities across subjects. For this step, they assumed that the image volume contains only two classes of voxels: 1) relatively higher intensity voxels within the surrounding tissues (body voxels) and 2) low intensities voxels in the lungs or in the air surrounding the body (non-body voxels). The method selects a segmentation threshold to separate the lung from surrounding tissues. This type of method is fast, easily-implementable and intuitive, but has

the disadvantage that it fails to deal with attenuation variations, to categorize pathologic classifications, and is sensitive to noise. In order to set the threshold  $T^i$  at iteration  $i$  of segmentation, the average intensity value  $\mu_b$  in body voxels and  $\mu_n$  in non-body voxels should be calculated: Subsequently, the new threshold  $T^{i+1}$  for iteration  $i + 1$  becomes as follows,

$$T^{i+1} = \frac{\mu_b + \mu_n}{2}. \quad (1)$$

$T^{i+1}$  is updated in every iteration of segmentation until the threshold does not change. This intensity-based thresholding method may not be applicable to lung tumor segmentation since the contrast between tumor region and non-tumor region is low.

### 2.1.2 Region-based methods

Region-based methods are more widely used since they account more suitably to Hounsfield unit variations. This method relies on neighboring voxels in the same region having similar intensity. Region growing is a popular region-based technique for lung segmentation [2, 43, 62, 96, 137, 113, 130]. Region growing algorithms start with a seed pixel, examine other pixels that surround it, determine the most similar one, and, if they meet certain criteria, they are included in the region. This process is followed until no additional pixels can be added. A similarity measure calculates the difference between the intensity value of each voxel and the mean intensity value in the region. The region is grown by examining all 4-neighboring pixels or 8-neighboring pixels to the region in 2-D. In every iteration of region growing, all unallocated neighboring voxels is added to the region. The process continues until the similarity measure meets certain stopping criteria. Dehmeshki et. al. [43] used a combination of fuzzy connectivity, distance and intensity information peripheral contrast, which segmented the pulmonary nodules. Sun et al. [130] presented a 3-D segmentation method for extracting the lung volume using region growing algorithms with automatic seed-locating methods through fuzzy logic algorithms. However, the region growing technique would fail depending on the magnitude of noise and the precision of the neighborhood criteria. In

addition to region growing, many region-based segmentation methods have been researched. For example, Watershed transform[93, 124], Graph-cuts which will be discussed in details in Section 3.1, Random walks[54], and Fuzzy connectedness[139]. Watershed transform’s main idea is that of a topographic relief which is flooded by water, with watersheds being the segmentation lines of the regions of interest of rain falling over the region. This method used distance between voxels and local intensity gradient to find segmentation boundary of the VOI(Volume of Interest). Even though it has computational efficiency, it has not been widely used because of the problem of oversegmentation. Random walk[54, 149] is also a good lung segmentation method with high accuracy. In this method, neighborhood coherence and probability of intensities of voxels are used to find a segmentation boundary.

### **2.1.3 Shape-based methods**

Shape-based segmentation methods include prior shape information about the object for recognition and delineation. Some proposed techniques use an atlas for prior shape[82, 153]. This approaches when there is a well-aligned object with the atlas, however, they fail when there is a pathology. On the other hand, model-based segmentation can perform optimal fitting through a prior statistical shape model, which considers both global and local variation of the shape and texture. Such an approach would be effective for segmenting the pathologic lung. The disadvantages of shape-based segmentation may be 1) difficulty of getting a proper training set, 2) computational costs, and 3) high sensitivity to training data.

## **2.2 Pulmonary Image motion tracking**

Accurate estimation of breathing motion in the lung is an important task in radio-therapy treatment. For motion tracking, deformable image registration (DIR) methods find lung motion and use the obtained motion field for reduced radiation dose to normal tissue. Image registration is one of the most important techniques in medical image analysis that

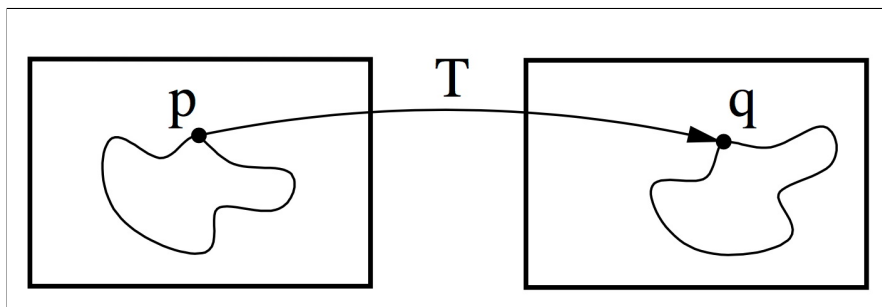


Figure 6. Image registration is the task of finding a spatial transform  $T$  mapping one image into another.

has been a significant area of activity for several decades [60, 128, 14, 101, 41, 108, 92]. In a nutshell, DIR determines the mapping of features between a source image and a target image obtained at different times or different imaging modalities. The deformation of the image can be classified as "rigid deformation" (where images need to be rotated and translated with respect to the pair to achieve correspondence) or "non-rigid deformation" (where correspondence between two images cannot be achieved without some localized stretching of the images). Rigid body registration considers only translation and rotation, which has 6 degrees of freedom, 3 translations, and 3 rotations. In early work [111, 61] and prior to the age of hybrid scanners, medical image registration was used for registering brain images of the same subject acquired with different scan modalities (e.g. MRI, CT or PET). For this application, a rigid body transformation suffices since there is little change in brain shape or the skull position between scans. To generalize, rigid body registration was extended to include affine registration which is non-rigid and includes scale factors and shears, is all having 12 degrees of freedom (3 translations, 3 rotations, 3 scalings, and 3 shears) for a 3-D volume.

However, motion for most parts of the human body can not be expressed precisely using a rigid or even an affine transformation. Thus, most recent developments in medical image registration involves development of non-rigid registration techniques. For lung motion tracking, non-rigid body registration can be performed through several methods which will be presented in this paper. An image registration technique is generally based upon the following three principal components;

- 1) **The transformation model:** specifies the way in which the source and the target image can be registered.
- 2) **The similarity(correspondence) measure:** is a metric that indicates how well the source image and the registered image match.
- 3) **The optimization process:** is the numerical method that minimizes an error criterion to arrive at parameters of the transformation model.

$I(x)$  is the intensity value at a position  $x$  in a fixed image  $I$  and  $J(T(x))$  is the intensity at the corresponding point given by the transformation  $T(x)$ .

### 2.2.1 The transformation model

The transformation model is required for two reasons, one of which is that it controls how image information in source would move relative to the target to improve the similarity of two images and another is that it interpolates features in space where there is no data. The motion field from the transformation model is updated iteratively after the maximization of the similarity measure between the source image and the target image by the motion fields. The typical input for lung CT DIR consists of two lung CT images at successive phases of the respiratory cycle. To track the lung motion a non-rigid transformation is required since it has more degrees of freedom. Often, an affine transformation is first performed before a more detailed non-rigid transformation with more degrees of freedom.

**Non-rigid transformation** A non-rigid transformation can describe more localized deformations than the rigid or affine transformations. There are numerous cases in which a non-rigid transformation is required, for example, 1) Cardiac motion tracking during the cardiac cycle and/or due to respiratory motion, 2) intra-operative deformation compensation for soft tissue tracking, 3) tracking shape or tissue longitudinal changes with time, for example, tumor growth, and 4) inter-subject organ registration due to differences in size, shape, and body habitus.

**Spline-based transformation** These are the most popular transformations which have been researched for around 20 years. Spline-based algorithms use control points to find correspondences in neighborhood of images using basis functions with local or global support.

The thin-plate spline (TPS)[15, 38, 98, 4] has been widely used for medical image registration. This method can make smooth deformations, can have a closed-form solution and needs few free parameters. Despite this, it has a limitation for modeling localized deformations or large transformations since each control point on a thin-plate spline has a global effect on the transformation.

In contrast to TPS, B-splines, an acronym for basis splines[42], are low order polynomial with local support. As a result, moving one control point only influences the transformation in the neighborhood of that point, having computational efficiency for a large number of control points. B-spline based techniques[121, 152] are very popular because of their general applicability, transparency and computational efficiency. They are mostly described by a free-form deformation (FFD) model[66, 88, 115, 121, 138]. Rueckert et al.[121] chose a Free-form deformation model(FFD) based on B-splines for breast MR Image registration. The basic concept of FFD is to deform an object by moving a mesh of control points. In order to formulate cubic B-splines under FFD, the set of control points  $\phi_{i,j,k}$  is set up on the  $n_x \times n_y \times n_z$  mesh with uniform spacing  $\delta$  in the domain of 3-D image volume  $\Omega = \{(x, y, z) | 0 \leq x < X, 0 \leq y < Y, 0 \leq z < Z\}$ . Subsequently, the 3-D tensor product of the familiar 1-D cubic B-splines is written as follows,

$$T_{local}(x, y, z) = \sum_{l=0}^3 \sum_{m=0}^3 \sum_{n=0}^3 B_l(u)B_m(v)B_n(w)\phi_{i+l,j+m,k+n}. \quad (2)$$

where  $i = \lfloor x/n_x \rfloor - 1$ ,  $j = \lfloor y/n_y \rfloor - 1$ ,  $k = \lfloor z/n_z \rfloor - 1$ ,  $u = x/n_x - \lfloor x/n_x \rfloor$ ,  $v = y/n_y - \lfloor y/n_y \rfloor$ ,  $w = z/n_z - \lfloor z/n_z \rfloor$ , and where  $B_l$ ,  $B_m$ ,  $B_n$  is the  $l_{th}$ ,  $m_{th}$ ,  $n_{th}$  cubic B-spline basis functions respectively.  $B_l$  is represented as follows.

$$\begin{aligned}
B_0(u) &= (1 - u)^3 / 6 \\
B_1(u) &= (3u^3 - 6u^2 + 4) / 6 \\
B_2(u) &= (-3u^3 + 3u^2 + 3u + 1) / 6 \\
B_3(u) &= u^3 / 6.
\end{aligned} \tag{3}$$

The spacing  $\delta$  of control points determines the scale of local deformations, For example, a large spacing  $\delta$  of control points provides more global non-rigid deformations, while a small spacing  $\delta$  of control points provides highly local non-rigid deformations. Even though there are some of FFD's disadvantages[138] , FFD is a popular choice in many applications since it can be easily implemented for B-spline function have relatively minor computational complexity.

**Optical Flow** Optical flow methods are based on the constant intensity assumption which requires that the gray value of a corresponding voxels not to change after displacement in a temporal sequence of images. Optical flow methods provide a good balance between computational costs and theoretical flexibility, and find voxel correspondences between two images by computing motion fields. Following equation is also known as the Horn-Schunck optical flow constraint or the brightness constancy constraint[63]. This imposes that the gray value of a voxel should not change after displacement:

$$I(\xi + W) = I(\xi). \tag{4}$$

where  $\xi$  represents a function of space and time,  $\xi := (x, y, z, t)^T$ , and  $W$  is the displacement vector field between two images,  $W := (u, v, w, 1)^T$ .

By the Taylor expansion,  $I(\xi + W)$  can also be expressed by Eq. (5).

$$I(\xi + W) = I(\xi) + \frac{\partial I}{\partial x}u + \frac{\partial I}{\partial y}v + \frac{\partial I}{\partial z}w + \frac{\partial I}{\partial t} + H.O.T. \tag{5}$$

Since Eq. (29) is identical to Eq. (5) and H.O.T. are the Higher Order Terms, which we assume are small and can safely be ignored, the formula is able to be re-organized as shown in Eq. (6)

$$\frac{\partial I}{\partial x}u + \frac{\partial I}{\partial y}v + \frac{\partial I}{\partial z}w + \frac{\partial I}{\partial t} = 0 \quad (6)$$

This yields the total energy function of optical flow:

$$\begin{aligned} E &= E_{total} = E_b^2 + \alpha^2 E_s^2 \\ &= \int \int \int (I_x u + I_y v + I_z w + I_t)^2 \\ &\quad + \alpha^2 (u_x^2 + u_y^2 + u_z^2 + v_x^2 + v_y^2 + v_z^2 + w_x^2 + w_y^2 + w_z^2) dx dy dz \end{aligned} \quad (7)$$

where  $E_b$  is the energy for the image brightness term,  $E_s$  is the energy for the smoothness term, and  $\alpha$  is the weighting factor.  $I_k$ ,  $u_k$ ,  $v_k$ , and  $w_k$  ( $k = x, y, z, t$ ) are the partial derivatives of image intensity  $I$  and displacement vectors  $u$ ,  $v$ , and  $w$  with respect to  $x$ ,  $y$ ,  $z$ , and  $t$ .

To solve the equation, we can compute a new set of motion fields ( $u^{n+1}, v^{n+1}, w^{n+1}$ ) iteratively from the estimated derivative using Gauss-Siedel method[57, 59].

$$\begin{aligned} u^{n+1} &= \bar{u}^n - \frac{I_x [I_x \bar{u}^n + I_y \bar{v}^n + I_z \bar{w}^n + I_t]}{(\alpha^2 + I_x^2 + I_y^2 + I_z^2)} \\ v^{n+1} &= \bar{v}^n - \frac{I_y [I_x \bar{u}^n + I_y \bar{v}^n + I_z \bar{w}^n + I_t]}{(\alpha^2 + I_x^2 + I_y^2 + I_z^2)} \\ w^{n+1} &= \bar{w}^n - \frac{I_z [I_x \bar{u}^n + I_y \bar{v}^n + I_z \bar{w}^n + I_t]}{(\alpha^2 + I_x^2 + I_y^2 + I_z^2)} \end{aligned} \quad (8)$$

$\bar{u}^n$ ,  $\bar{v}^n$ , and  $\bar{w}^n$  are the local average of the motion field in  $n$ th iteration in Eq. (8).

The optical flow equation itself is not sufficient to find motion fields due to the aperture problem, thus a regularization term as smoothness constraint is required. Moreover, optical flow methods work well when motion fields are small[11]. Many optical flow methods have been researched. In addition to Horn and Schunck method, Lucas et al.[89] introduced local energy optimization of optical flow so called Lucas-Kanade method, which has robustness to image noise, while it has the problem of not being able to produce dense flow. This local method makes assumption about motion fields valid only on a neighborhood of the image domain. Bruhn et al.[25] combined Horn-Schunck method with Lucas-Kanade and proposed the Combined Local-Global (CLG) method. This CLG optical flow method maintains robustness to image noise while being able to produce a dense motion field.

### 2.2.2 The similarity measure

The similarity measure between the source image  $I$  and the target image  $J$  is defined, and the transformation  $T$  will be adjusted when the similarity measure is maximized since two image would become very similar when aligned. The most popular similarity measures are introduced in this section. Following Eq. shows the similarity measure that will be maximized to find the optimal transformation  $\hat{T}$  between source and target.

$$\hat{T}(x) = \underset{T \in \text{searchspace}}{\operatorname{argmax}} \operatorname{Similarity}(I(x), J(T(x))) \quad (9)$$

**Sum of Squared Differences** The sum of squared differences(SSD) is the simplest similarity measure. Only when gaussian noise exists in the image, the result of registration will not be correct. This measure is however sensitive where there are a small number of voxels that have very large intensity differences.

$$SSD = \frac{1}{N} \sum_x (I(x) - J(T(x)))^2 \quad (10)$$

**Correlation coefficient** The correlation coefficient(CC) relies on the idea that the intensities of the corresponding voxels have a linear relationship. The CC and SSD are not

applicable to multi-modal registration but only for the images obtained by a single modality.

$$CC = \frac{\sum_x (I(x) - \bar{I}) \cdot (J(T(x)) - \bar{J})}{\sqrt{\sum_x (I(x) - \bar{I})^2 \cdot \sum_x (J(T(x)) - \bar{J})^2}} \quad (11)$$

where  $\bar{I}$ ,  $\bar{J}$  are the mean of the intensities in  $I$ ,  $J$  respectively.

**Mutual Information** The mutual Information(MI) assumes only entropies of the intensity distribution using a probabilistic relationship between intensities[144, 90, 112, 86, 90, 121]. The disadvantage of MI is that it is sensitive to interpolation artifacts[129], and that it examines joint and marginal intensity distributions only[8], that is “Locality” in the MI.

$$MI = H_I + H_J - H_{IJ}$$

$$\textit{Entropies of the intensity distribution :} \quad (12)$$

$$H_I = - \sum_i P_i \log P_i, \quad H_J = - \sum_j Q_j \log Q_j, \quad H_{IJ} = - \sum_{i,j} p_{ij} \log p_{ij}$$

where  $P$  and  $Q$  is the probability of intensity  $I$  and  $J$  occurring in target and source respectively and  $p_{ij}$  is the joint probability of both occurring at the same place. This measure works for multi modality system as well.

**Normalized Mutual Information** The normalized Mutual Information(NMI) is the normalized version of MI, which reduces the overlap problem[112]. The size of the overlapping area of two images can influence the mutual information measure. With decreasing overlap during registration, the mutual information measure can increase. This may occur when the relative areas of object and background and the sum of the marginal entropies increases faster than the joint entropy. Therefore, normalizations of joint entropy can be helpful to overcome this problem which is less sensitive to changes in overlap.

$$NMI = \frac{H_I + H_J}{H_{IJ}} \quad (13)$$

## CHAPTER 3

### GRAPH-CUTS SEGMENTATION

#### 3.1 Introduction

Graph-cuts have been researched on several fronts in image processing since they were first introduced in the late 1980s. Firstly, Greig et al.[55] addressed the energies for graph-cuts as shown in Eq. (14), and developed the minimization of the energy function by min-cut/max-flow algorithms; such energy functions have been widely used. Before this algorithm, the energy function could not be exactly minimized, and the global minimum was elusive. However, since binary image restoration which was considered by Greig was limited, the graph-cut method was not noticed for the next ten years as, in this formulation, the segmentation is biased to very small intensity range. Jianbo Shi et al. [123] tried to solve this problem by normalized cut, which is NP-hard using an approximation technique. In the 1990s, many computer vision methods used graph-cuts for non-binary problems. Roy et al. [120] used max-flow algorithms to perform multi-camera stereo matching. Shortly afterwards, Boykov et al. [18], and Ishikawa et al. [70] performed minimization of the energy function in the multi-label case with linear boundary terms for image segmentation.

Since, a large number of methods have utilized graph-cuts to minimize energies in many applications. Image segmentation [20, 70, 143], image restoration [55], shape reconstruction [126], image registration [52, 135] and so on. Our work is motivated by Boykov and Jolly[23] who first proposed how to use graph cuts to efficiently extract objects for  $N - D$  applications based on a wide range of visual cues, contextual information, and useful topological constraints. The graph cuts framework show implicit boundary representation that is considered as a discrete counterpart of the level-set method, whose relationship with the

level-set method is discussed in [22]. Graph-cuts have been extended in a large number of directions: geometric cues[16, 77](geo-cuts), regional cues based on Gaussian mixture models [13] for improved interactivity [119, 134] (grab-cuts), binary segmentation using stereo cues [78], extraction from  $2D + t$  video [84, 145], multiple objects segmentation[83], combining segmentation with 3-D pose estimation[24], and methods for solving surface evolution PDEs[21].

## 3.2 The Basic Concepts

### 3.2.1 Graph Construction

Given a 3-D image  $I$ , a graph= $\langle V, E \rangle$  can be constructed with  $V$  as a set of nodes comprising image voxels and  $E$  a set of edges which connect the nodes [17]. A set of all node pairs  $\{p, q\}$  of neighboring nodes in the set of image nodes. To find an optimal boundary with a graph-cuts algorithm, two additional special terminal nodes are needed: these are called the source node,  $S$ , and the sink node,  $T$ . In the case of binary image segmentation, the set of labels  $A_p = \{1, 2\}$  correspond to the object, placed inside the lung or tumor, for example, and the background, outside lung or non-tumor, respectively. Terminals correspond to the set of labels that can be assigned to nodes. The graph has two types of edges: n-link and t-link. The n-links connect pairs of neighboring nodes such as  $\{p, q\}$ . This neighboring system can be 4-(2D), 8-(2D), 6-(3D), 26-(3D) neighborhood in the image. The cost of n-links corresponds to similarity between the nodes. These values are usually obtained from the node interaction term  $B_{p,q}$  in Eq. (14). T-links connect pixels with terminals (labels). The cost of a t-link connecting a node and a terminal corresponds to a value for assigning the corresponding label to the node. This cost is normally derived from the data term  $R_p$  in Eq. (14) [17].

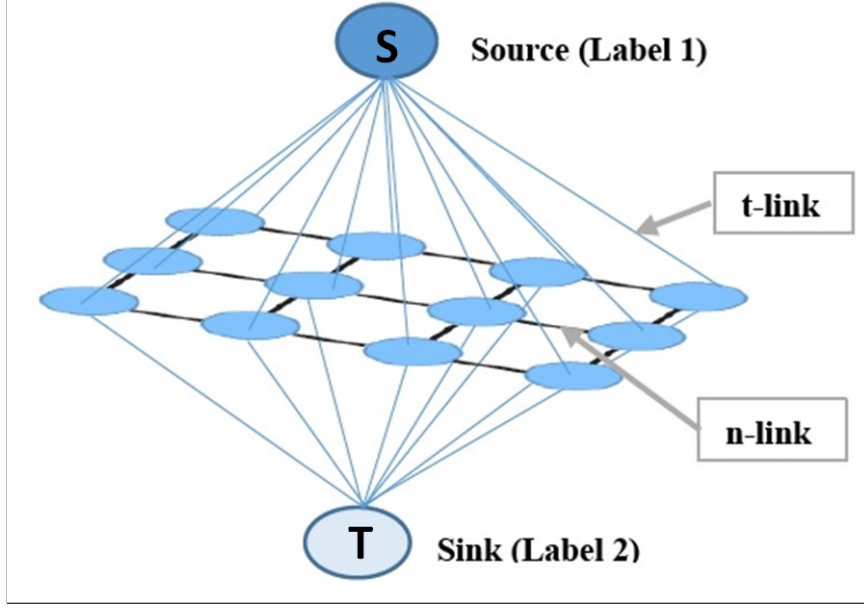


Figure 7. Graph construction

### 3.2.2 Energy Function

$$Energy(A) = \lambda \cdot \sum_{p \in P} R_p(A_p) + \sum_{\{p,q\} \in N} c \cdot B_{p,q}(A_p, A_q). \quad (14)$$

In order to find the minimum  $s/t$  cut which separate two image regions, object and background, the sum of edge weights along the cut is optimized through the max-flow algorithm. And we can find the minimum energy to cut the edges so that the “object“ is separated from the “background“. In the case of binary labeled segmentation (object and background), the standard max-flow algorithm is sufficient. In case where more than two labeled segmentation is required, the alpha-expansion algorithm is utilized.

**Regional Term** The regional term  $R_p$  assumes that the individual penalties for assigning voxel  $p$  to “object” and “background”, correspondingly  $\lambda \cdot R_p(“obj”)$  and  $\lambda \cdot R_p(“bkg”)$  are given. For example,  $R_p$  represents how well a voxel  $p$  is assigned to the object and background

intensity group, e.g., through using a probability density function expressed by a histogram.

$$R_p(A_p) = -\ln P(I_p|A_p) \quad (15)$$

The weight on the t-link  $\{p, S\}$  can be calculated as  $-\lambda \cdot \ln P(I_p | \text{"bkg"})$  and on the t-link  $\{p, T\}$ ,  $-\lambda \cdot \ln P(I_p | \text{"obj"})$  is the edge weight, where  $S$  is the source node, and  $T$  is the sink node.

**Boundary Term** The node interaction term  $B_{p,q}$  contains the “boundary“ properties of segmentation, and can increase as a function of similarity between  $p$  and  $q$ . When  $p$  and  $q$  have low contrast,  $B_{p,q}$  is large, while very different intensities between  $p$  and  $q$  result in  $B_{p,q} \approx 0$  as may be deduced from Eq. (16) where  $\delta_{A_p \neq A_q}$  is a Kronecker delta representing interaction potential,:

$$B_{p,q}(A_p, A_q) = \exp\left(-\frac{(I_p - I_q)^2}{2\sigma^2}\right) \cdot \delta_{A_p \neq A_q} \quad (16)$$

$$\text{where } \delta_{A_p \neq A_q} = \begin{cases} 1 & \text{if } A_p \neq A_q \\ 0 & \text{if } A_p = A_q \end{cases}$$

In order to find the minimum  $s/t$  cut which separates two image regions, object and background, the sum of edge weights along the cut is maximized through the max-flow algorithm. This results in maximum separates between object and background. For the weight setting of this algorithm, we will discuss about parameter sensitivities in Section 3.5.2 are used. And we can find the minimum energy cut through the graph which cuts the edges so that the “object“ is separated from the “background“. In the case of binary labeled segmentation (object, background), the standard max-flow algorithm [17, 19, 79] is sufficient.

TABLE 1

Edge weights in graph-cuts segmentation [17]

Edge	Weight (cost)	For
$\{p, q\}$	$c \cdot B_{p,q}$	$\{p, q\} \in N$
$\{p, S\}$	$\lambda \cdot R_p$ ("bkg")	$p \in P, p \notin O \cup B$
	$K$	$p \in O$
	$0$	$p \in B$
$\{p, T\}$	$\lambda \cdot R_p$ ("obj")	$p \in P, p \notin O \cup B$
	$0$	$p \in O$
	$K$	$p \in B$

### 3.3 Max-flow Algorithm

Most of the graph-cuts algorithms belong to straight-forward implementations, for example, Augmenting max-flow algorithm (Ford and Fulkerson[49]) or Push-Relabel algorithms (Goldberg and Tarjan [53]), which are slow in practice. Boykov et al.[17] have introduced the modified versions of these two algorithms, which is well-known for graph-cuts method and is relatively a fast algorithm.

#### 3.3.1 Augmenting Path Algorithm (Ford-Fulkerson)

The Ford-Fulkerson augmenting algorithm[49] was introduced in the mid-1950's. Standard augmenting paths based algorithms work by pushing flow along non-saturated paths from the source to the sink until the maximum flow in the graph  $G$  is reached. A typical augmenting path algorithm stores information about the distribution of the current  $s \rightarrow t$  flow  $f$  among the edges of  $G$  using a residual graph  $G_f$ . The topology of  $G_f$  is identical to  $G$  but capacity of an edge in  $G_f$  reflects the residual capacity of the same edge in  $G$  given the amount of flow already in the edge. At the initialization there is no flow from the source

to the sink ( $f = 0$ ) and edge capacities in the residual graph  $G_0$  are equal to the original capacities in  $G$ . At each new iteration the algorithm finds the shortest  $s \rightarrow t$  path along non-saturated edges of the residual graph. If a path is found then the algorithm *augments* it by pushing the maximum possible flow  $df$  that saturates at least one of the edges in the path. The residual capacities of edges in the path are reduced by  $df$  while the residual capacities of the reverse edges are increased by  $df$ . Each augmentation increases the total flow from the source to the sink  $f = f + df$ . The maximum flow is reached when any  $s \rightarrow t$  path crosses at least one saturated edge in the residual graph  $G_f$ [17].

Theorem: A flow  $f$  has maximum value if and only if there is no flow augmenting path with respect to  $f$ .

---

**Algorithm 1:** Ford-Fulkerson Algorithm [105]

---

```

1 for each edge  $f(u, v) \in f$  do
2   do
3      $f(u, v) \leftarrow 0$ 
4      $f(v, u) \leftarrow 0$ 
5     while there exists a path  $P$  from  $s$  to  $t$ 
6     in the residual network  $G_f$ 
7     do
8       for each edge  $(u, v)$  in  $P$  do
9         do
10         $f(u, v) \leftarrow f(u, v) + c_f(P)$ 
11         $f(v, u) \leftarrow -f(u, v)$ 
12      end
13 end

```

---

After the max-flow is found, the maximum cut is determined by:

$$S = \{\text{All vertices reachable from } s\}$$

$$T = G/S$$

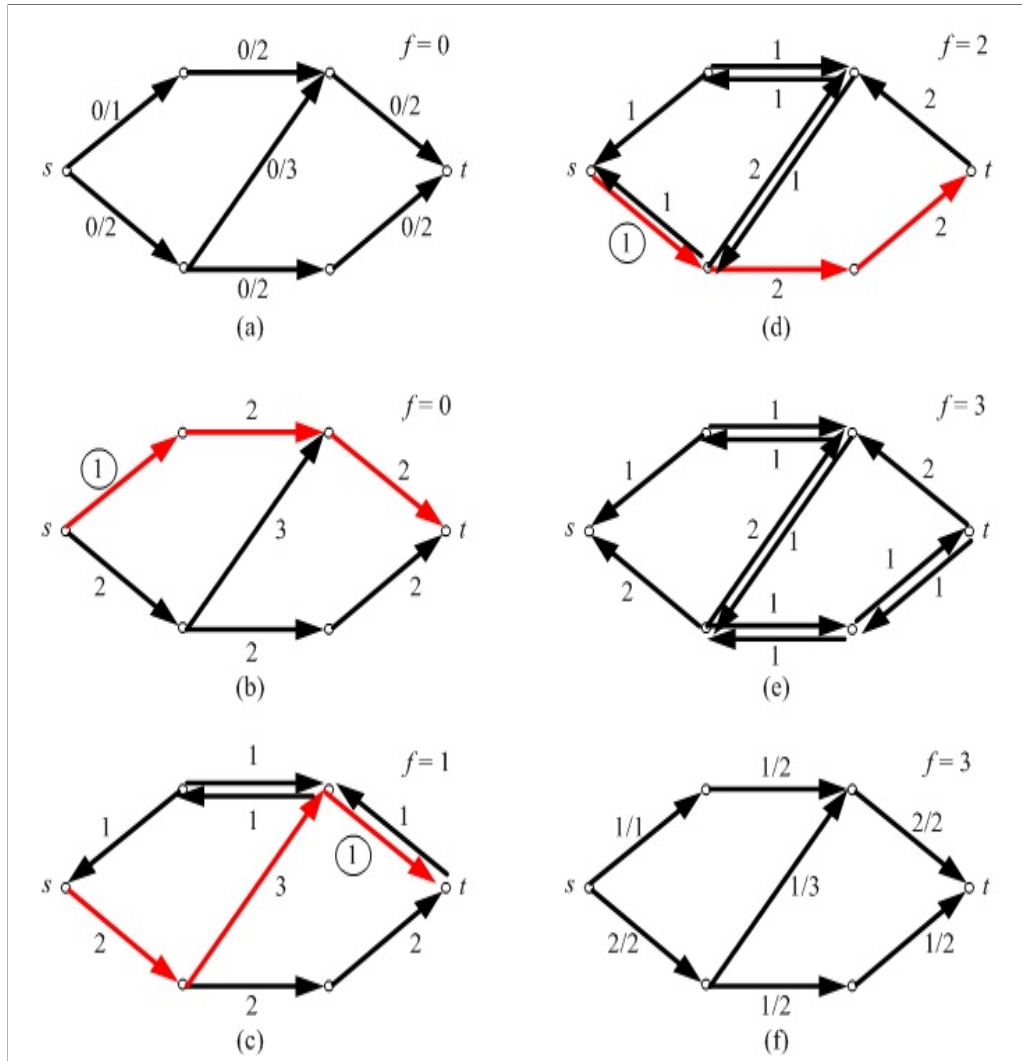


Figure 8. Ford-Fulkerson Algorithm[105]

The running time of the algorithm depends on how the augmenting path is determined, and if the searching for augmenting path is realized by a breath-first search, the algorithm runs in polynomial time  $O(E|f_{max}|)$ .

### 3.3.2 Boykov's Maximum Flow = Minimum Cut algorithm

The Max-flow/ Min-cut algorithm was developed by improving standard augmenting path algorithm. The augmenting path technique tries to find  $s/t$  cut until all given edges in the graph are saturated. In practice, it needs to scan most paths in the graph to build a breadth-first search trees, which means the computation of graph-cuts may be so expensive in the worst case scenario. Boykov's algorithm provided a pathway to solve this issue. This algorithm is similar to Dinic's augmenting algorithm[44], which builds two search trees for  $S$  from the source and  $T$  from the sink. Unlike Dinic's algorithm, these trees are reused and do not start building them from scratch. In theory, this seems to be worse in the time complexity than the standard algorithms discussed. In practice, Boykov's algorithm significantly outperforms standard algorithms.

**General Structure** At the beginning of the graph construction, two search trees  $S$  and  $T$  are not overlapped each of which has roots from the source  $s$  and  $t$  respectively, and all edges in search trees are non-saturated. All nodes in  $V$  can be defined as follows.

$$\begin{aligned} S \subset V, \quad s \in S, \quad T \subset V, \quad t \in T, \\ S \cap T = \emptyset \end{aligned} \tag{17}$$

The nodes defined as  $S \cap T = \emptyset$  are called 'free nodes' and all nodes in search trees become either 'active node' or 'passive node'. Algorithm 2 gives an overview of Boykov's algorithm which iteratively repeats three stages.

The iterations of three stage, 1) Growth stage, 2) Augmentation stage and 3) Adoption stage, keep processing until the search trees  $S$  and  $T$  can not grow any longer and those are divided by saturated edges, which means that a maximum flow and the corresponding

---

**Algorithm 2:** Boykov Algorithm\_General Structure [17]

---

```
1 Initialize:  $S = \{s\}, T = \{t\}, A = \{s, t\}, O = \emptyset$ 
2 while true do
3   grow  $S$  or  $T$  to find an augmenting path
4    $P$  from  $s$  to  $t$ 
5   if  $P = \emptyset$  then
6     augment on  $P$ 
7     adopt orphans
8   end
9 end
10 end while
```

---

minimum cut are determined.

**Growth Stage** At this stage, the search trees expand finding neighboring non-saturated edges to find another active nodes of the corresponding search trees from a set of free nodes. When all neighboring nodes of an active node are explored, the active nodes become passive nodes. This stage meet the stop criterion when an active node faces a node in the opposite tree.

**Augmentation Stage** At the augmentation stage, the path found at the growth stage will be augmented. In order to saturate some edges in the given path  $P$  from  $s$  to  $t$ , the largest flow possible is pushed through this path. The saturated edges linking the nodes to their parents become no longer valid, then the nodes may change to 'orphan nodes'

**Adoption Stage** The adoption stage adopts the orphan nodes occurred at the augment stage to a new valid parent.

**Flow chart with Simple Example for segmentation** The flow chart in Figure 9, 10, 11, 12 is showing the simple example of Boykov's algorithm through the growth stage, the augment stage and the adoption stage. Each character in the flow chart is defined as follows.

---

**Algorithm 3:** Boykov Algorithm\_Growth Stage [17]

---

```
1 At this stage, active nodes acquire new children from a set of free nodes.
2 while  $A \neq \emptyset$  do
3   pick an active node  $p \in A$ 
4   for every neighbor  $q$  such that  $tree\_cap(p \rightarrow q) > 0$  do
5     if  $TREE(q) \neq \emptyset$  then
6       then add  $q$  to search tree as an active node:
7        $TREE(q) := TREE(p), PARENT(q) := p, A := A \cup \{q\}$ 
8     end
9     if  $TREE(q) \neq \emptyset$ ; and  $TREE(q) \neq TREE(p)$  then
10      return  $P = PATHs \rightarrow t$ 
11    end
12  end
13  end for
14  remove  $p$  from  $A$ 
15 end
16 end while
17 return  $P \neq \emptyset$ 
```

---

$$Tree \Rightarrow Search\ trees \begin{cases} S \rightarrow Source \\ T \rightarrow Sink \end{cases}$$

$$Type \Rightarrow Types\ of\ nodes \begin{cases} A \rightarrow Active\ nodes \\ P \rightarrow Passive\ nodes \\ O \rightarrow Orphan\ nodes \\ \emptyset \rightarrow Free\ nodes \end{cases}$$

$$Parent \Rightarrow Parents\ of\ nodes \begin{cases} s \rightarrow The\ parent\ of\ the\ node\ is\ the\ source\ node. \\ p \rightarrow The\ parent\ of\ the\ node\ is\ the\ sink\ node. \\ \emptyset \rightarrow This\ node\ does\ not\ have\ any\ parent\ node. \end{cases}$$

As shown in Figure 12, some min-cuts are obtained when the max-flow algorithm stops. One of min-cuts which has the minimum sum of flow across the edges on the corresponding

---

**Algorithm 4:** Boykov Algorithm Augmentation Stage [17]

---

```
1 Input: A path  $P$  from  $s$  to  $t$ .
2 The orphan set is empty in the beginning of the stage, but there might be some
  orphans in the end since at least one edge in  $P$  becomes saturated.
3 find the minimum edge capacity  $\Delta$  on  $P$ 
4 update the residual graph by pushing flow  $\Delta$  through  $P$ 
5 for each edge  $(p, q) \in P$  that become saturated do
6   | if  $TREE(p) = TREE(q) = S$  then
7   |   | then set  $PARENT(q) := \neq \emptyset$  and  $O := O \cup \{q\}$ 
8   | end
9   | if  $TREE(p) = TREE(q) = T$  then
10  |   | then set  $PARENT(p) := \neq \emptyset$  and  $O := O \cup \{p\}$ 
11  | end
12 end
13 end for
```

---

---

**Algorithm 5:** Boykov Algorithm Adoption Stage [17]

---

```
1 During this stage, all orphan nodes  $\emptyset$  are processed until  $\emptyset$  becomes empty.
2 while  $O \neq \emptyset$  do
3   | pick an orphan node  $p \in \emptyset$  and remove it from  $\emptyset$ 
4   | scan all neighbors  $q$  of  $p$  such that  $TREE(q) = TREE(p)$ 
5   | if  $q$  is a valid parent ( $TREE(q) = TREE(p)$ ,  $tree\_cap(q \rightarrow p) > 0$ ) then
6   |   | set  $PARENT(p) = q$ 
7   | end
8 end
9 end while
```

---

min-cut becomes the optimal min-cut.

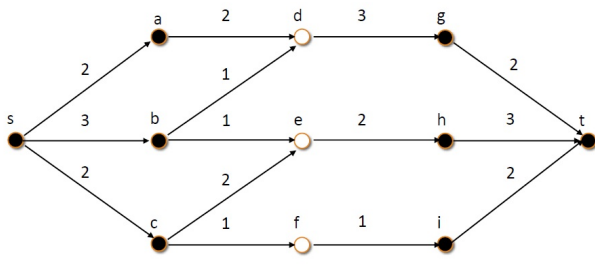
### 3.4 Advantages of Graph-cuts

**Global optima and applicability to N-D problems** One interesting feature of the graph-cuts method is that it is able to calculate a global minimum of the energy function for an N-dimensional segmentation[55, 147, 69, 23]. Since the global minimum provides potentially better stability, it is attractive. The main reason why global minima can not be found is very much related to the specific energy function given rather than the actual minimiza-

tion method. Many earlier segmentation techniques do not have a clear energy function[2], or only find an approximate solution, computing a local minimum very far from the global minimum. Before 2000s, some segmentation method[36, 99, 46, 39, 71] showed the possibility of finding the solution globally, but those could be computed only for two-dimensional applications. The  $s/t$  graph cuts technique gives a globally optimal object extraction method for N-dimensional images.

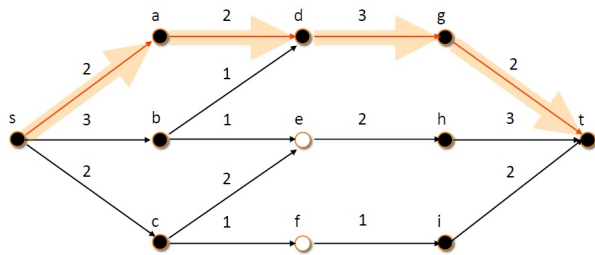
**Practical efficiency** Boykov and Kolmogorov[17] showed the practical efficiency of combinatorial max-flow algorithms for applications in computer vision, which showed that max-flow algorithms could extract the objects from 2-D and 3-D problems in nearly real-time using regular PCs. Further research has shown that there is significant speed-up for dynamic segmentation problems, for example, flow-recycling[76] and cut-recycling[72]. Running graph-cuts with parallel processors[68] is possible and enhance the segmentation performance. In order to reduce the memory consumption for 3-D applications, the multilevel banded techniques[87] was introduced.

**Numerical robustness** Graph-cuts image segmentation technique usually relies on the max-flow algorithm from combinatorial optimization, while Snake[148] and Finite elements technique[95] are usually optimized based on variational methods. Convergence in variational methods is non-trivial issue that has to be carefully designed[115]. Image segmentation results in variational methods may vary depend on how the algorithm is implemented, even though the same energy function may be used. Graph-cuts, however, has numerical robustness. When we use the same energy function, the identical segmentation results would always be obtained despite the fact that we can use a number of different max-flow/min-cut algorithms for image segmentation, such as Augmenting max-flow algorithm[49], Push-Relabel algorithms[53], and Boykov’s max-flow algorithm[17].



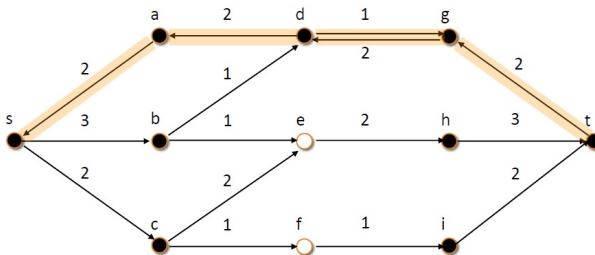
(a) Initialization

$Node(Tree, Type, Parent)$   
 $a(S, A, s)$   $d(\emptyset, \emptyset, \emptyset)$   $g(T, A, t)$   
 $b(S, A, s)$   $e(\emptyset, \emptyset, \emptyset)$   $h(T, A, t)$   
 $c(S, A, s)$   $f(\emptyset, \emptyset, \emptyset)$   $i(T, A, t)$



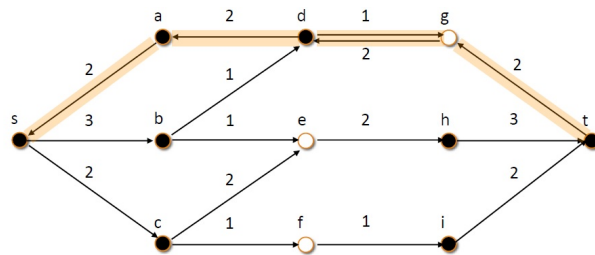
(b) 1stGrowth

$Node(Tree, Type, Parent)$   
 $a(S, P, s)$   $d(S, A, a)$   $g(T, A, t)$   
 $b(S, A, s)$   $e(\emptyset, \emptyset, \emptyset)$   $h(T, A, t)$   
 $c(S, A, s)$   $f(\emptyset, \emptyset, \emptyset)$   $i(T, A, t)$



(c) 1stAugment

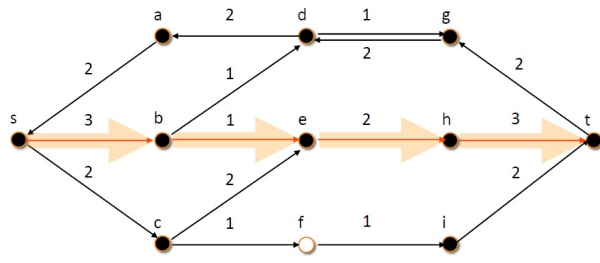
$Node(Tree, Type, Parent)$   
 $a(S, O, \emptyset)$   $d(S, O, \emptyset)$   $g(T, O, \emptyset)$   
 $b(S, A, s)$   $e(\emptyset, \emptyset, \emptyset)$   $h(T, A, t)$   
 $c(S, A, s)$   $f(\emptyset, \emptyset, \emptyset)$   $i(T, A, t)$



(d) 1stAdoption

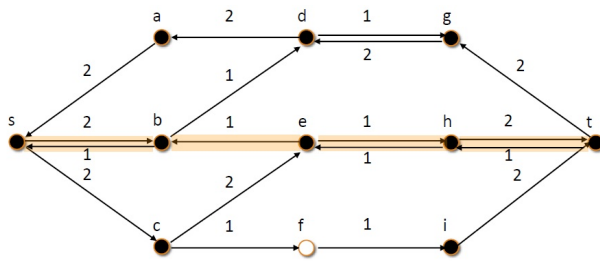
$Node(Tree, Type, Parent)$   
 $a(S, P, d)$   $d(S, A, b)$   $g(\emptyset, \emptyset, \emptyset)$   
 $b(S, A, s)$   $e(\emptyset, \emptyset, \emptyset)$   $h(T, A, t)$   
 $c(S, A, s)$   $f(\emptyset, \emptyset, \emptyset)$   $i(T, A, t)$

Figure 9. Boykov Algorithm, Flow Chart(1) [105]



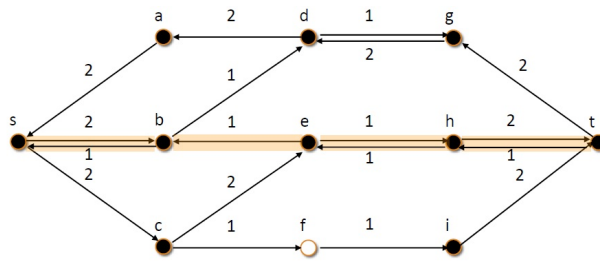
(a) 2ndGrowth

$Node(Tree, Type, Parent)$   
 $a(S, P, d) \quad d(S, P, b) \quad g(S, A, d)$   
 $b(S, P, s) \quad e(S, A, b) \quad h(T, A, t)$   
 $c(S, A, s) \quad f(\emptyset, \emptyset, \emptyset) \quad i(T, A, t)$



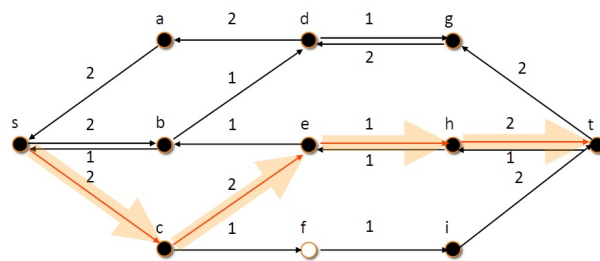
(b) 2ndAugment

$Node(Tree, Type, Parent)$   
 $a(S, P, d) \quad d(S, P, b) \quad g(S, A, d)$   
 $b(S, P, s) \quad e(S, O, \emptyset) \quad h(T, A, t)$   
 $c(S, A, s) \quad f(\emptyset, \emptyset, \emptyset) \quad i(T, A, t)$



(c) 2ndAdoption

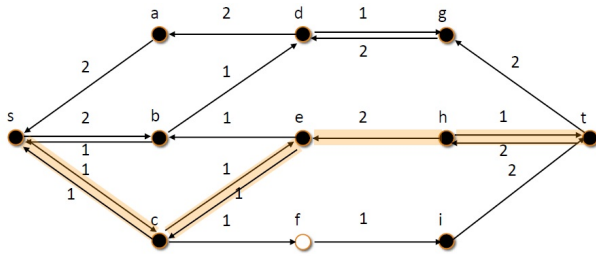
$Node(Tree, Type, Parent)$   
 $a(S, P, d) \quad d(S, P, b) \quad g(S, A, d)$   
 $b(S, P, s) \quad e(S, A, c) \quad h(T, A, t)$   
 $c(S, A, s) \quad f(\emptyset, \emptyset, \emptyset) \quad i(T, A, t)$



(d) 3rdGrowth

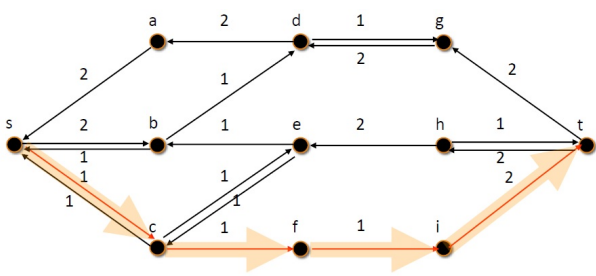
$Node(Tree, Type, Parent)$   
 $a(S, P, d) \quad d(S, P, b) \quad g(S, A, d)$   
 $b(S, P, s) \quad e(S, A, c) \quad h(T, A, t)$   
 $c(S, A, s) \quad f(\emptyset, \emptyset, \emptyset) \quad i(T, A, t)$

Figure 10. Boykov Algorithm, Flow Chart(2) [105]



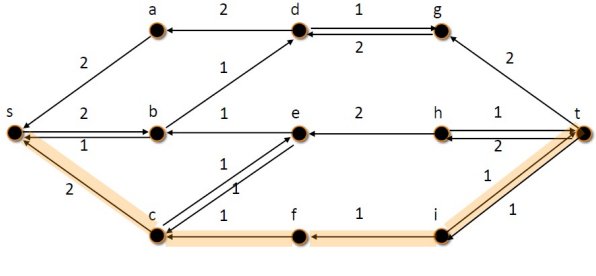
(a) 3rdAugmentAdoption

*Node (Tree, Type, Parent)*  
 $a(S, P, d)$   $d(S, P, b)$   $g(S, A, d)$   
 $b(S, P, s)$   $e(S, A, c)$   $h(T, A, t)$   
 $c(S, A, s)$   $f(\emptyset, \emptyset, \emptyset)$   $i(T, A, t)$



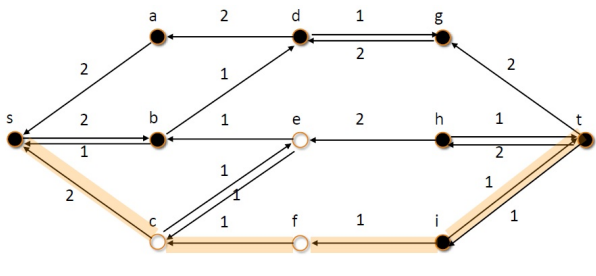
(b) 4thGrowth

*Node (Tree, Type, Parent)*  
 $a(S, P, d)$   $d(S, P, b)$   $g(S, A, d)$   
 $b(S, P, s)$   $e(S, A, c)$   $h(T, A, t)$   
 $c(S, P, s)$   $f(S, A, c)$   $i(T, A, t)$



(c) 4thAugment

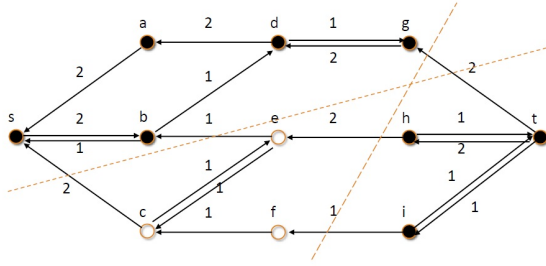
*Node (Tree, Type, Parent)*  
 $a(S, P, d)$   $d(S, P, b)$   $g(S, A, d)$   
 $b(S, P, s)$   $e(S, O, \emptyset)$   $h(T, A, t)$   
 $c(S, O, \emptyset)$   $f(S, O, \emptyset)$   $i(T, A, t)$



(d) 4thAdoption

*Node (Tree, Type, Parent)*  
 $a(S, P, d)$   $d(S, P, b)$   $g(S, A, d)$   
 $b(S, P, s)$   $e(\emptyset, \emptyset, \emptyset)$   $h(T, A, t)$   
 $c(\emptyset, \emptyset, \emptyset)$   $f(\emptyset, \emptyset, \emptyset)$   $i(T, A, t)$

Figure 11. Boykov Algorithm, Flow Chart(3) [105]



*Node (Tree, Type, Parent)*  
 $a(S, P, d)$   $d(S, P, b)$   $g(S, A, d)$   
 $b(S, P, s)$   $e(\emptyset, \emptyset, \emptyset)$   $h(T, A, t)$   
 $c(\emptyset, \emptyset, \emptyset)$   $f(\emptyset, \emptyset, \emptyset)$   $i(T, A, t)$

(a) STOP

Figure 12. Boykov Algorithm, Flow Chart(4)[105]

### 3.5 3-D Lung Boundary Segmentation with Graph-cuts

#### 3.5.1 Lung segmentation with Graph-cuts

Lung segmentation is important in clinical workflow. Segmentation can aid clinical experts to a more accurate diagnose without mistakes. The lung boundary information, the location and the shape information of organs, and bones around the lung can be obtained by graph-cuts segmentation. In order to extract the lung boundary, the binary graph-cuts may be used, and for extracting multi organs and bones, the multi-label graph-cuts is used. The graph-cut method is able to be extended to  $n$ -dimensional data, so graph-cut segmentation is flexible for 2-D, 3-D, and even 4-D lung data set.

#### 3.5.2 Analysis of Parameter Sensitivities for Graph-cuts segmentation of Lung CT

The energy function in Eq. (14) is dependent on the setting of parameters  $\lambda$ ,  $c$ . We performed strict comparison of automated segmentations introduced in Section 3.5.3 with expert traced boundaries and proposed empirical rules regarding how to set these parameters for 3-D CT lung segmentation for accurate results. The parameter settings for  $\lambda$ ,  $c$  and  $K$ , sensitively affects the 3-D segmentation results. Appropriate parameter settings lead to accurate lung boundary segmentation.

TABLE 2

The parameter sensitivity for 3-D lung image segmentation [32]

Parameters			Error Metrics		Results
$K$	$\lambda$	$c$	$\gamma_T$	$\tau_T$	
0.5	0.5	1.5	99.2540	0.8421	Good
3			99.2592	0.8483	Good
5			99.2723	0.8591	Good
30			99.2707	0.8591	Bad (artifacts)
5	5	1.5	99.2355	0.8606	Good
	0.1		99.2422	0.8591	Bad (artifacts)
	0.05		98.3911	0.8530	Bad (artifacts)
	0.01		38.6072	0.2496	Bad (wrong boundary)
5	0.5	1.7	99.2723	0.8591	Good
		0.7	99.2723	0.8591	Good
		0.1	99.2723	0.8591	Good

Utilizing error metrics introduced in Eq. (20) and Eq. (21) in Section 3.5.3, Table 2 illustrates how lung segmentation is dependent on parameters for a typical data set. The value of  $\gamma_T$  shows how much the segmentation result and the ground truth match each other, and the value of  $\tau_T$  indicates the discrepancy between the two. For comparisons, each parameter is varied while the other two are kept fixed. Through the results in Table 2, we are able to define the range of parameters for reliable 3-D CT lung image segmentation with the graph-cut method. First, the value of  $K$  has already been defined in previous research [17]; however, empirically, the following setting lead to good results.

$$K = \frac{c}{2} \times +m + 1. \quad (18)$$

In (18),  $c$  denotes the similarity coefficient, and  $m$  denotes the  $m$ -neighborhood system for calculating the  $n$ -links. For simplicity, the 4-neighborhood system in 2-D, and the 6-neighborhood system in 3-D was used. Further analysis lead to additional empirical relationships among parameters. Many artificial dots around seed points resulted when the value of  $K$  was much larger than  $\lambda$ . For example, in the case of  $K = 30$  when  $\lambda = 0.5$ , or

in the case of  $\lambda = 0.05$ , or  $0.01$  when  $K = 5$  some artifacts around the location of actual seed points occur, and this resulted in the wrong segmentation result since the region of seed points became dominant. Figure 13(b) show the segmentation results including artifactual dots in one 2-D slice of a 3-D image volume. The value of  $K$  that appeared to provide good segmentation results satisfied the condition that  $K < 20 * \lambda$ . Finally, the value of  $\lambda$  influences the balance between  $B_{p,q}$  and  $R_p$  and for good segmentations. A value obeying

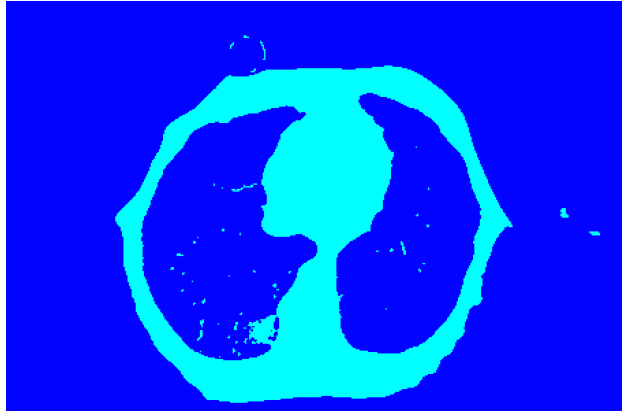
$$\lambda \approx \frac{c}{3}. \quad (19)$$

resulted in a good segmentation. Setting  $\lambda$  to a very small value caused the data term in the energy function to become much less important, resulting in the boundary term became primary. This caused the automatically detected lung boundary to cross over the actual lung boundary. Figure 13(c) shows that the method extracts the wrong lung boundary and includes artificial dots where  $\lambda$  is set to a very small value and the value of  $K$  is large.

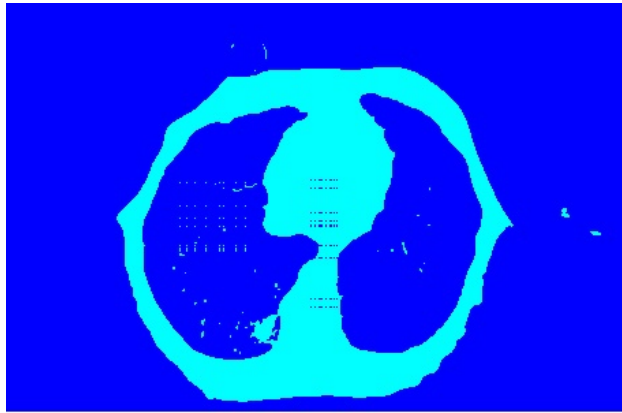
### 3.5.3 3-D Segmentation with Graph-cuts on the Lung CT image

#### Lung boundary case

Given the lung CT data provides the size of the image volume and the intensities of whole image voxel. We will accomplish the segmentation of lung boundary splitting the inside of lung and the outside of lung which is soft tissue and bone etc. The inside lung and the outside lung are set as 'the object' and 'the background' of graph-cuts method. The object is composed of voxels of low intensities compared to the background since inside lung is most occupied with air. The seed points for the hard constraint need to be selected on the object and the background separately as shown in Figure 16. From the seed points selection, the range of intensities of the object and the background can be defined, and we recognize these two parts have been distributed on the clearly different range of histogram as shown



(a)



(b)



(c)

Figure 13. Results of 3-D segmentation of Patient01. (a) Segmented image with two labels  $K = 5, \lambda = 0.5, c = 1.5$  (b) Binary segmentation results with artifact due to bad parameters selection  $K = 5, \lambda = 0.1, c = 1.5$ , (e) Binary segmentation results with artifact due to bad parameters selection  $K = 5, \lambda = 0.01, c = 1.5$  [32].

in Figure 14.

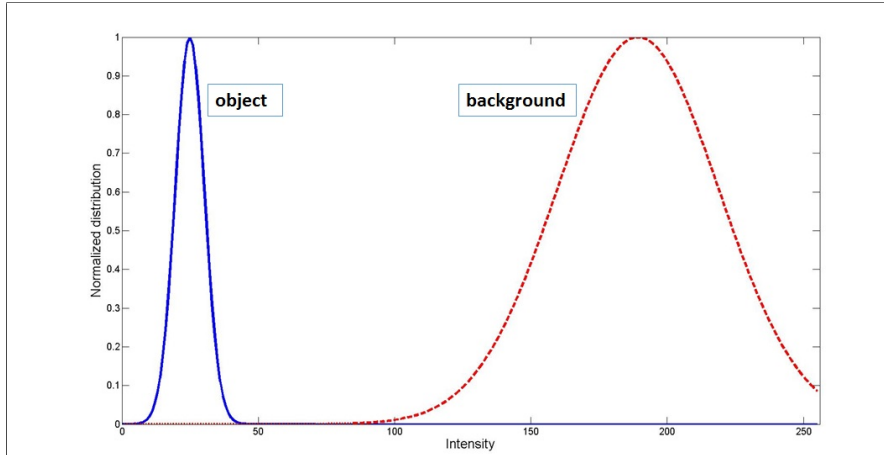
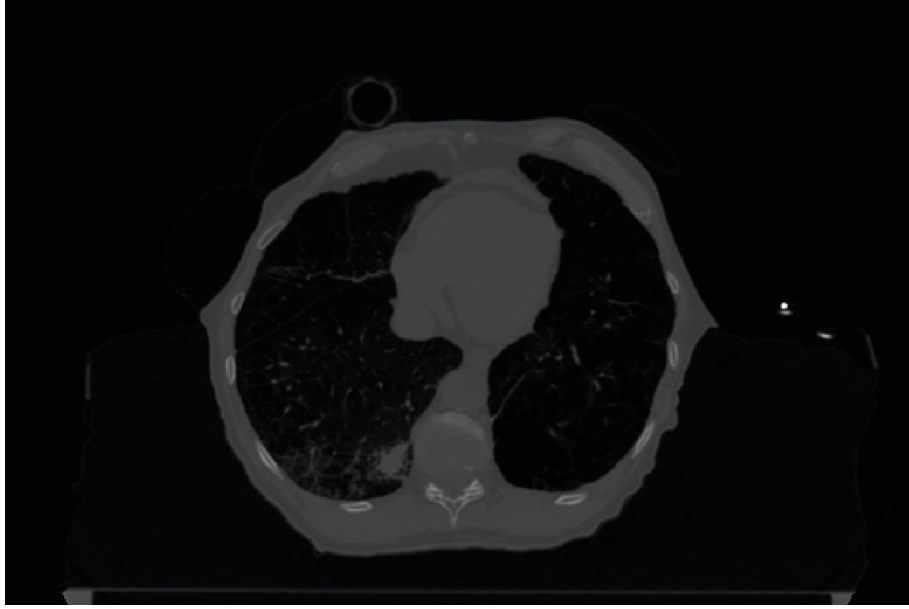


Figure 14. The histogram for the intensity range of seed points. The blue line plot represents the object and the red dot plot represents the background.

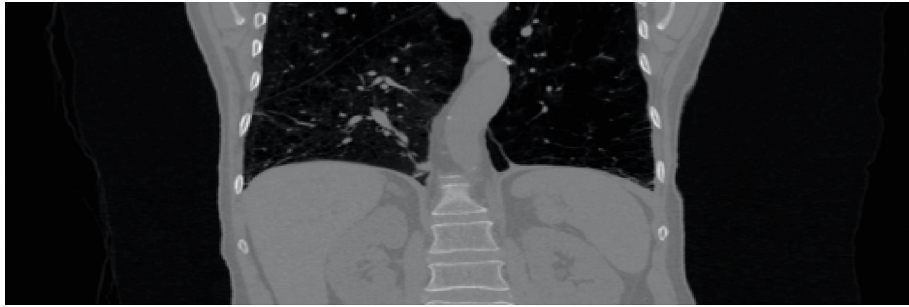
In graph-cuts segmentation weights for t-links are provided based on this histogram. Moreover, we can put another hard constraint to strengthen the labeled points. We give an appropriately large constant value to the actual seed points location so as to not miss these voxels. The weight for n-links is calculated based on how similar the intensities of two neighboring voxels are. If the neighboring voxels have very similar values, weights become larger. Otherwise, reduced weights close to zero are assigned. The max flow-min cut method is applied to segment the object from the background.

Four 3-D lung CT data were used for validation. Each CT volume contained from 118 to 197 axial slices with resolution  $1.1719 \times 1.1719 \times 1.5 \text{ mm}^3$ . Figure 17 shows results from the segmentation in 3-D. The segmentation results were validated using two error metrics, one of which is the error metric defined in Eq. (20) and Eq. (21) and another is the Dice similarity coefficient (DSC). The error metric in [33] compares the number of voxels in a segmented volume,  $V_{seg}$ , with the number of voxel in the ground-truth volume  $V$  as delineated by an expert. If  $V_{intersection}$  is used to denote the volume of intersection ( $V_{intersection} = V \cap V_{seg}$ ), the rate of correct voxel classification of the method is given by

$$\gamma^T = \frac{V_{intersection}}{V} \times 100\%. \quad (20)$$



(a) 2-D axial slice



(b) 2-D coronal slice

Figure 15. 2-D axial and coronal slices of the lung

With  $V \setminus V_{seg}$  representing  $V \cap V_{seg}^c$ , another metric proposed in [33] is

$$\tau^T = \frac{(V_{intersection})^2}{V(V \setminus V_{seg})} \times 100\%. \quad (21)$$

As mentioned in Section 3.5.2, the value of  $\gamma_T$  shows how much the segmentation result and

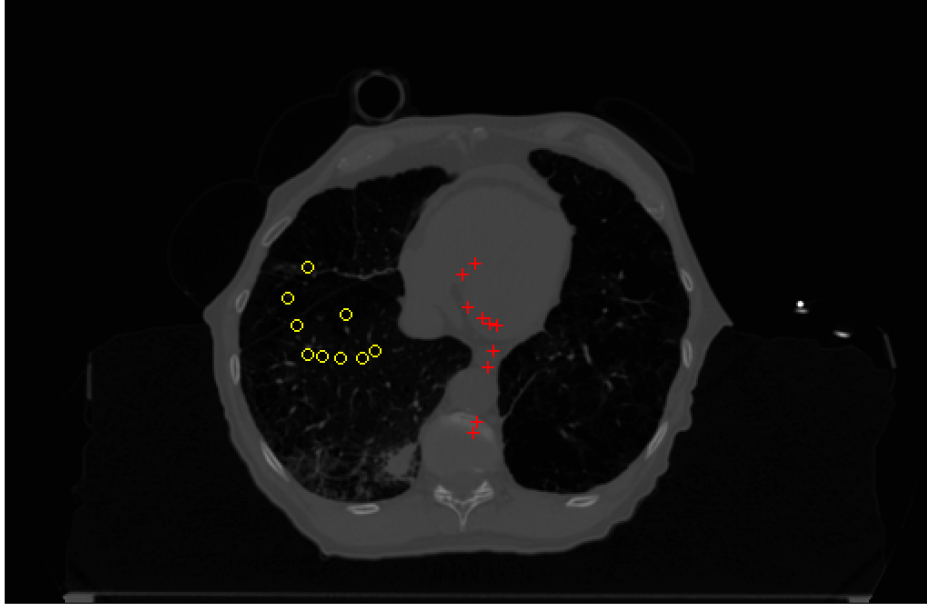


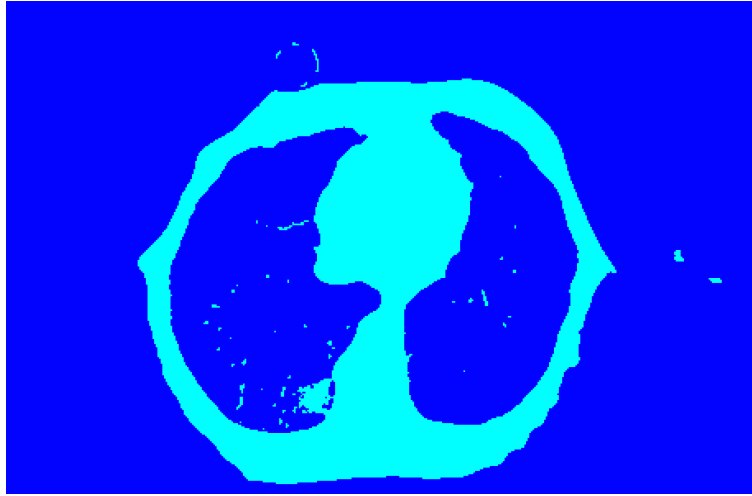
Figure 16. The selection of seed points. Yellow circles: seed points for object (inside the lung), red crosses: Seed points for background (outside the lung).

the ground truth result match, whereas  $\tau_T$  indicates the discrepancy between the two.

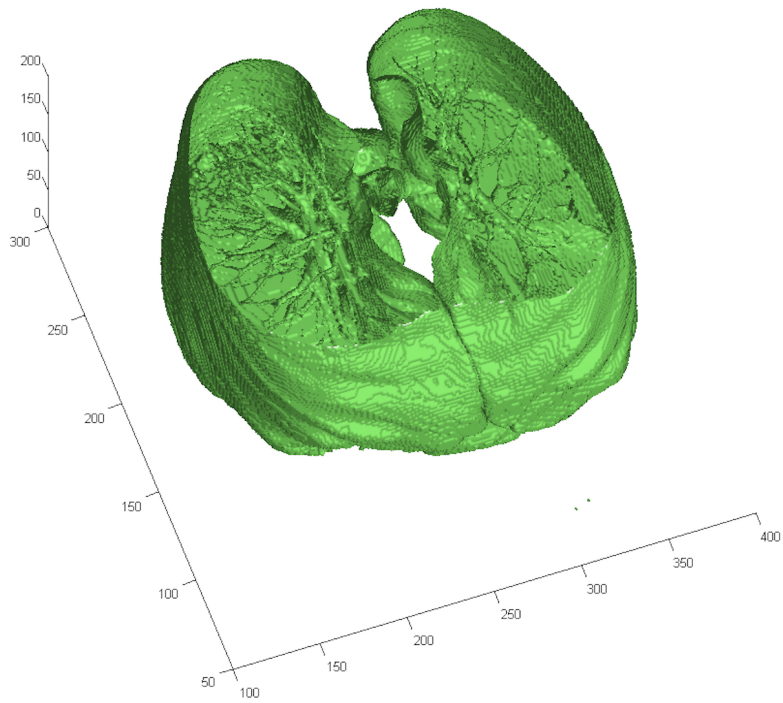
Another error metric, Dice similarity coefficient (DSC), is spatial overlap index and a reproducibility validation metric. The value of DSC ranges from 0, indicating no spatial overlap between two sets of binary segmentation results, to 1, indicating complete overlap. DSC is defined in Eq. (22).

$$DSC = \frac{2 \times |A \cap B|}{|A| + |B|}. \quad (22)$$

where  $|A|$  is the volume of true segmentation, and  $|B|$  is the volume of automated segmentation. Table 3 shows results for validation of the segmentation based on the four lung CT data.



(a) The visualization on the 2-D axial slice



(b) The visualization on the 3-D volume

Figure 17. The result of 3-D segmentation with binary graph-cuts method [32]

TABLE 3

Validation results from applying 3-D graph-cuts segmentation to lung boundaries in four 3-D CT data sets, comparing automated segmentation with ground truth [32].

Data	Error metric		
	Error metric		Dice similarity coefficient
	$\gamma^T$ (%)	$\tau^T$	
1	99.2723	0.8591	0.9521
2	98.4142	0.7806	0.9251
3	94.3130	0.8520	0.9391
4	93.4093	0.8460	0.9562

### 3.6 3-D tumor segmentation via Graph-cut Optimization Including Prior Trained Shape

CT lung scans are of a great use to analyze and track the lung nodules that might turn out to be cancer. An important step in this process is segmenting the nodule to locate and measure the volume of nodule in different periods of time. Previously, authors have proposed various approaches to segment lung nodules from CT scans. In summary, these methods can be categorized into four general approaches: thresholding methods [116, 103], region growing [43, 141], active contours [47, 48], and graph-cut methods [151, 30]. In early attempts Reeves *et al.* [116] performed segmentation by applying an adaptive threshold computed for each scan to compensate for the variations between two consecutive scans in conjunction with a geometrical constraint to favor spherical shape structures. Dehmeshki *et al.* [43] proposed a region growing approach where each neighboring voxel is added to the nodule region based on intensity contrast and distance to center of the region. Ginneken [141] also used region growing, however the regions were grown by a machine learning approach in which voxel features were fed to a classifier to predict its label as nodule or non-nodule. Some studies combined region growing and thresholding methods and presented a multilevel framework. Badura and Pietka [10] performed Otsu thresholding, region growing, morphological oper-

ations, and thickening to segment juxta vascular and juxta pleural nodules from attached organs. In another approach [146], authors extended the gradient, energy, and curvature concepts to 3-D volumes and segmented lung nodules in an active contour fashion [74]. Farag *et al.* [47] proposed another active contour framework to model intensity of nodules as nonparametric Gaussian distribution. 3-D segmentation was carried out by 2-D active contours slice by slice, subsequently stacking the resulting planes on top of each other to form the 3-D result. In another study in this domain [48], a sparse representation of training shapes were incorporated into active contours to contribute adaptively to the conventional active contour energy function. Graph-cuts segmentation, a method adopted in this thesis, is another approach to segment nodules in the lung. Cha *et al.* [30] revised the graph-cuts energy function to incorporate shape prior into graph-cuts energy function.

Indeed, graph-cuts techniques have been popular and have been applied to a variety of image segmentation tasks. Cha *et al.* [29] determined the optimal parameter settings of conventional graph-cuts segmentation for lung volumes. Massoptier and Casciaro [94] and Beichel *et al.* [12] performed 3-D liver segmentation in contrast enhanced CT data, or MRI data using graph cuts. Despite great usage of intensity-based techniques like graph-cuts, they may suffer from inaccurate extraction in case of low contrast between the object and the background. Therefore, a few publications have also proposed graph-cuts segmentation using shape prior to constrain a specific shape. Slabaugh and Unal [125] used an elliptical binary mask as shape prior for segmenting circular structures in blood vessel MRI. Funka-Lea *et al.* [51] proposed a blob term which gives weights depending on the distance from the center of seed points region, and modifies the regularization term of the energy function to segment the heart volume in CT scans. Freedman and Zhang [50] used a shape prior with signed distance function for segmentation, but they tried to empirically apply the fixed shape prior template without any shape refinement during segmentation. Grosgeorge *et al.* [56] performed graph-cuts segmentation using a shape prior which was generated by active shape model (*ASM*) from 3-D heart images, though they extracted the shape variations offline and built a fixed shape prior in the training step. Also their method first needed to register

the shape model to the image with a rigid motion, resulting in expensive computations. Nakagomi *et al.* [104] proposed 3-D lung segmentation with shape prior using statistical shape model (*SSM*) via graph-cuts.

Compared to previous research just described, our proposed algorithm performs shape refinement via principal component analysis (*PCA*) and incorporates the shape prior which is generated by *ASM* with signed distance function. The shape prior template is not fixed in our formulation and is based on training data which constrains the segmentation through iterative shape refinement. Our approach refines the shape prior through projection of the segmented region from each iteration into a valid shape space defined by principle components of the training data. More specifically, by bringing information from the segmented region into the statistical analysis, we are provided with a more adaptive and accurate shape prior. Finally, the method is applied in 4-D. In order to extend 3-D segmentation to 4-D, the warped refined shape is applied to each successive phase. A few publication have proposed graph-cuts segmentation in 4-D. Linguraru *et al.* [85] performed abdominal organ segmentation using 4-D graph-cuts with shape and location constraints for livers, spleens and kidneys. This method used Parzen windows to generate shape models, and modified the energy function by adding the enhance term obtained from contrast-enhanced CT data and the location term. However, as with 3-D segmentation, 4-D segmentation especially for nodules is still challenging due to existence of tissues surrounding the nodule which have similar Hounsfield units.

### 3.6.1 Active Shape Model (ASM) with Signed Distance Function

Medical image segmentation using *ASM* has been highly popular. General *ASM* methods finds the boundary of the objects via *PCA* with given landmark coordinate information based on a training set. However, as pointed out in previous research [40], there are some drawbacks to this approach : 1) Extension of explicit representations which are landmark-based to higher dimensions is not straightforward and requires tedious human effort. 2) Landmark-based representations do not permit to topological changes because they

rely on a labeling of space and as a result, require complicated splitting and merging techniques. In order to solve these problems, for boundary representation in 3-D, we chose an implicit shape representation wherein the shape boundary is represented as the zero level set of a signed distance function (*SDF*) in a higher dimensional space. The signed distance function  $\phi$  at the voxel  $(x, y, z)$  can be defined as the shortest distance between the voxel and the shape boundary, representing the zero level set. The value of the voxel inside the boundary is negative, and outside the boundary positive, while the shape boundary is located on the zero-crossing of the SDF. Figure 18 shows an example of a lung boundary modeled as the zero level set of a signed distance function.

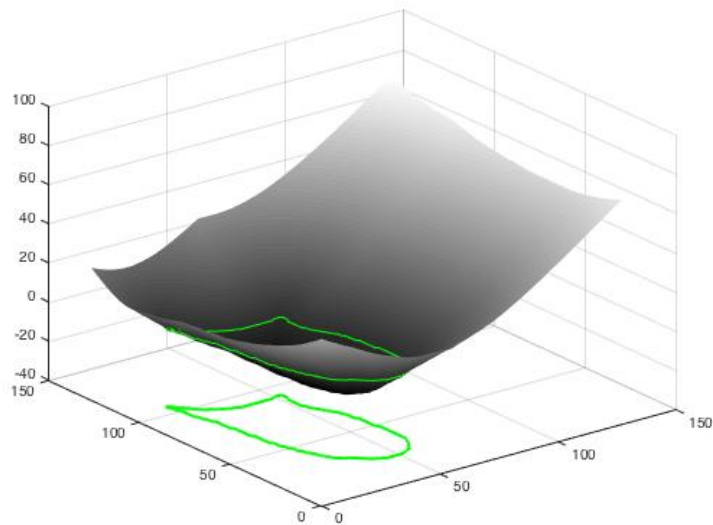


Figure 18. Lung boundary embedded as the zero level set of signed distance function

To compare like-parts of the shapes and obtain statistics from given training sets, exact shape alignment in most cases is demanding. However, SDFs provide tolerance to slight misalignments [81]. We chose to translate shapes to roughly align with a reference shape. Moreover, eigenvectors calculated by *PCA* from the training set can deform the mean shape in scale variations and curvature variations [81].

Let  $T$  be the training matrix which consists of vectorized training SDFs  $\phi_i$  in each

column. Given  $n$  shapes in the training set, the mean  $\bar{\phi}$  of all training SDFs is represented as follows:

$$\bar{\phi} = \frac{1}{n} \sum_{i=1}^n \phi_i. \quad (23)$$

In order to represent variations in the training set, PCA computes eigenvectors and eigenvalues of the training matrix. Let  $R$  be the residual matrix which is obtained from the difference between the mean signed distance function and each training signed distance function:

$$R = \{\phi_1 - \bar{\phi}, \phi_2 - \bar{\phi}, \dots, \phi_n - \bar{\phi}\}. \quad (24)$$

The matrix of eigenvectors,  $U$ , which is the direction of variations, and the diagonal matrix of eigenvalues,  $D$  can be calculated by Eq. (25).

$$UDU^T = \frac{1}{n} RR^T. \quad (25)$$

In fact, the eigenvalue decomposition is employed to factor  $\frac{1}{n}RR^T$  (as shown in Eq. (25)) as eigenvector and eigenvalue matrix. However, in this case, the dimension of  $\frac{1}{n}(RR^T)$  is large (Number of voxels \* Number of voxels) so the calculation of the eigenvectors and eigenvalues of this matrix is computationally expensive. In practice, according to reference [81], the eigenvectors and eigenvalues of  $\frac{1}{n}(RR^T)$  can be efficiently computed from a much smaller  $n*n$  matrix :  $\frac{1}{n}(R^T R)$  where  $n$  is the number of shapes in the training set. Indeed, this approach was adopted in our implementation for computing eigenvectors and eigenvalues.

In the proposed algorithm, the segmented image  $\phi(\tau)$  extracted in iteration  $\tau$  by graph-cuts is refined to the range of variations in the training database. The weight corresponding to the direction of variations is approximated by Eq. (26).

$$w(\tau) = U_k^T (\phi(\tau) - \bar{\phi}), \quad (26)$$

where  $U_k$  is the first  $k$  column of  $U$ , and  $w(\tau) \in \mathbb{R}^k$  is the weight vector calculated in iteration  $\tau$ , each entry of which weighs a single eigenvector. In previous work, authors [50, 56], used

a fixed shape prior template for graph-cuts segmentation, however the algorithm proposed herein refines the shape prior iteratively based on the segmented image  $\phi(\tau)$  obtained by graph-cuts. In each iteration  $\tau$  of graph-cuts, a shape prior is deformed to best approximate the segmented region while at the same time keeping the shape in the valid shape space through solution to Eq. (26), further refining the shape prior with the weight  $w(\tau)$  obtained from Eq. (27).

$$\tilde{\phi}(\tau) = \bar{\phi} + U_k w(\tau). \quad (27)$$

The refined shape prior  $\tilde{\phi}(\tau)$  is then used as prior information for the next iteration  $\tau + 1$  of graph-cuts. Clearly, in the first iteration ( $\tau = 1$ ), when there is no information about the shape of the nodule, the algorithm uses the mean shape  $\bar{\phi}$  obtained from the training step as the prior. The advantage of this approach is that it automatically captures and adapts the valid shape variations for each nodule in the testing step. That is, based on the current segmented data, the allowed shape variations are updated to best match shapes of nodule image. Also, we need another constraint on  $w$  wherein each  $w_i$  is restricted to lie in the range  $(-2\sqrt{\lambda_i}, 2\sqrt{\lambda_i})$  where  $\lambda_i$  is the  $i$ th ( $i = 1 \sim k$ ) eigenvalue [37].

The first three eigenvectors were employed to capture shape variations. We arrived at this number by visually investigating the changes in the shape while varying each eigenvector. This number (number of eigenvectors) accounts for the most important shape variations in the training set. As shown in Figure 19, the first eigenvector is best at capturing the variation in nodule size. While the second and third eigenvectors also seem to capture volume size, but in a smaller range and also in a different direction. As we can see, the shape variations corresponding to fourth eigenvector is not significant.

### 3.6.2 3-D tumor segmentation with Prior Trained Shape

Graph-cuts have been widely used for image segmentation due to their advantage of global optimization and computational speed. However, the intensity-based nature of graph-cuts makes their use difficult for foreground/ background segmentation in low contrast

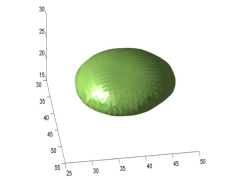
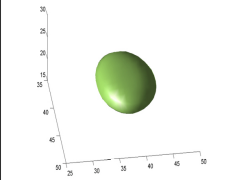
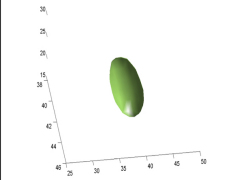
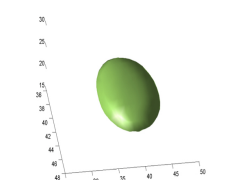
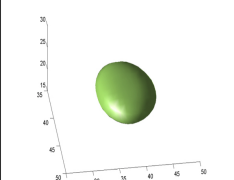
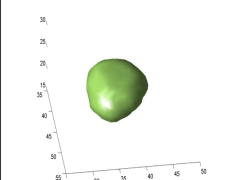
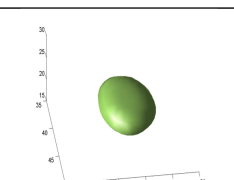
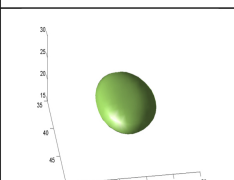
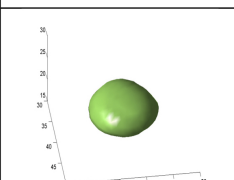
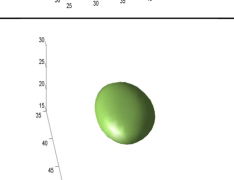
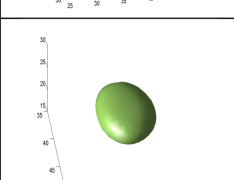
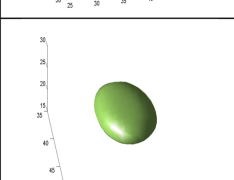
	$-2\sqrt{\lambda}$	Mean shape	$+2\sqrt{\lambda}$
Eigenvector 1			
Eigenvector 2			
Eigenvector 3			
Eigenvector 4			

Figure 19. Deformations of the mean shape generated by varying the weight corresponding to the first four primary eigenvectors.

images. To help the segmentation process, we need shape prior information. Eq. (28) is the modified version of Eq. (14), which is the graph-cuts energy function using the shape prior from ASM [81, 34].

$$\begin{aligned}
 Energy(A) = & \sum_{p \in P} (\lambda \cdot R_p(A_p) + \alpha \cdot S_p(A_p)) \\
 & + \sum_{\{p,q\} \in N} c \cdot B_{p,q}(A_p, A_q)
 \end{aligned} \tag{28}$$

$S_p$  is the shape prior term represented by the signed distance function which is the distance from voxel  $p$  to the boundary of the shape.  $\lambda$ ,  $\alpha$  and  $c$  are the weights for the regional term, shape prior term, and boundary term, respectively. Chen and Bagci [34] introduced

iterative graph-cuts and ASM which uses landmarks during PCA analysis to perform 3-D anatomical segmentation of organs (liver, left and right kidneys, spleen, and foot bones). As noted earlier, in this paper, we adopt a *SDF* representation. This is an improvement since SDF does not require explicit correspondence of landmark points and furthermore is a whole boundary representation.

For the training step of the proposed algorithm, 3-D nodule shapes from ground-truth patient data are aligned using nodule centroids and are translated accordingly. Based on the translated shapes, signed distance function of training shapes are derived and are stored in a matrix. PCA analysis is then applied on this matrix representation and the mean shape and corresponding eigenvectors are computed. These eigenvectors are used during an iterative shape refinement procedure which progresses until an optimal segmentation is reached. Algorithm 6 is the pseudo-code for the algorithm’s training step.

---

**Algorithm 6:** Training Step

---

**input** : n shapes represented as binary masks.

**output:** The mean shape, and the eigenvalues and eigenvectors from PCA analysis.

- 1 Align all nodule training shapes according to a reference mask centroid.
  - 2 Extract signed distance function for all training shapes.
  - 3 Store all signed distance functions in a matrix. Find the mean shape, as vectorized signed distance function.
  - 4 Apply PCA analysis on training data and compute the eigenvalues and eigenvectors.
- 

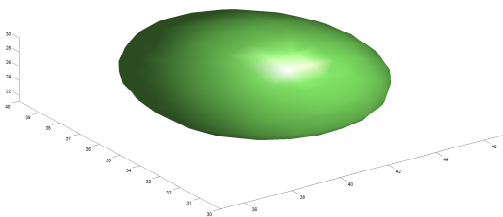


Figure 20. 3-D visualization of nodule mean shape, determined from over 500+ training images from the LIDC Cancer Imaging Archive Data Sets [7].

### 3.7 4-D tumor segmentation via Graph-cut Optimization Including Prior Trained Shape and Motion

4-D lung nodule segmentation is accomplished by graph cuts using a prior shape model, image intensity information, and estimates of local motion. When we run the optical flow method, the motion fields  $u, v, w$  for  $x, y, z$  coordinates can be calculated between successive phases.

#### 3.7.1 Motion estimation by Optical Flow

The optical flow technique finds voxel correspondences between two images by computing image displacements fields. With  $I$  denoting the intensity of the image voxels, the constant intensity assumption yields a differential equation commonly referred to as the optical flow constraint equation (also known as the Horn-Schunck optical flow constraint) [63]. This imposes that the gray value of a voxel should not change after displacement:

$$I(\xi + W) = I(\xi). \quad (29)$$

where  $\xi$  represents a function of space and time,  $\xi := (x, y, z, t)^T$ , and  $W$  is the displacement vector field between two images,  $W := (u, v, w, 1)^T$ .

#### 4-D (3-D + t) motion estimation with Optical Flow

In order to extend 3-D segmentation to 4-D (3-D+ t), we use optical flow [63] for motion estimation between successive phases (e.g. phase 10-phase 20, phase 20-phase 30,...). Motion fields then warp the mean shape in time on a point by point basis. Figure 21 briefly presents the visualization of motion fields on the 2-D axial slices from 3-D volumes of interest around the nodule shapes. From the results of motion estimation over consecutive phases in the testing data, we realized that tumor regions from our testing data do not have large motion to move the center of tumors a lot. For these case, it is true that warping the shape prior over consecutive phases does not highly affect the segmentation results. However, if we perform 4-D nodule segmentation with other testing data which include nodules which have large motion during respiratory cycle since PCA analysis itself can not obtain the

translational motion of nodules, the motion estimation over consecutive phases would be necessary. During breathing, the largest motion appears on the diaphragm. When the nodule is located near the diaphragm, the nodule may have more motion and deformation during respiratory cycle. In this case, motion estimation between successive phases would be more necessary. From the review of our testing nodule data, we confirmed that no nodule is located near the diaphragm.

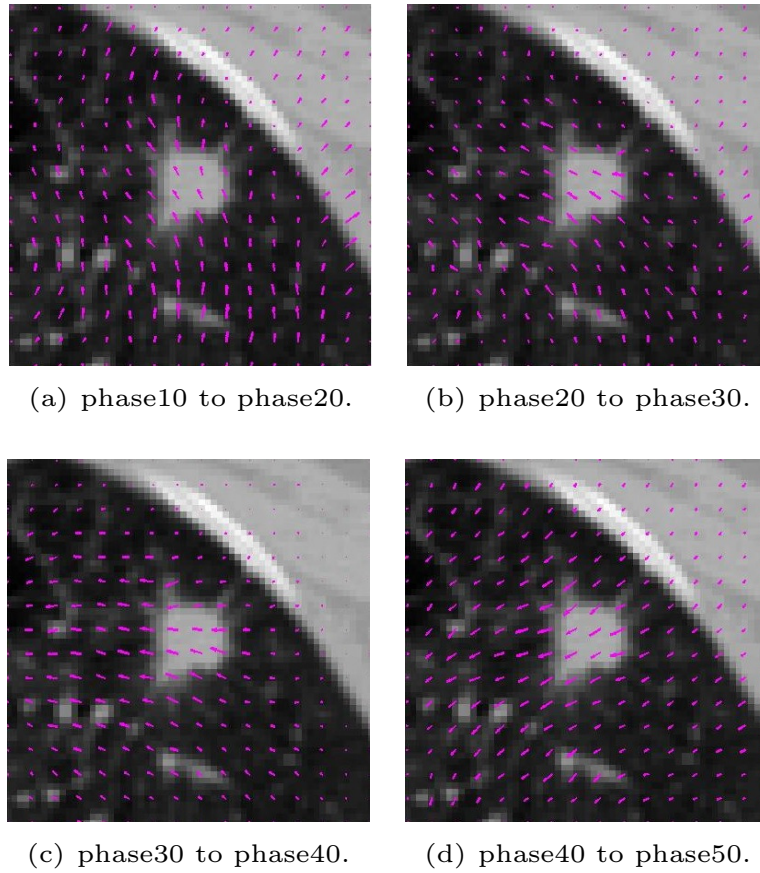


Figure 21. Visualization of the motion fields on 2-D axial slices. (a) Motion fields from phase 10 to phase 20 displayed at phase10, (b) from phase 20 to phase 30 at phase 20, (c) from phase 30 to phase 40 at phase 30, (d) from phase 40 to phase 50 at phase 40.

### 3.7.2 4-D Lung nodule segmentation

**Testing step** After obtaining the warped mean shape, we perform 4-D (3-D+t) segmentation via graph cuts through five phases with shape refinement via PCA analysis [30, 31]. The training step was discussed in Section 3.6.2.

For the testing step, we are given 4-D lung data sets each of which consists of five phases during the respiratory cycle (from a phase 10 which is max-inhale to a phase 50 which is max-exhale). During the testing step, for each phase, graph-cuts and ASM (with signed distance function) is performed. To apply the algorithm, the initialized mean shape from the training step is used as the shape prior. The PCA analysis refines the shape through several iterations in order to find feasible fitting with the segmented image until the energy value become stable.

Algorithm 7 describes the computational steps for 4-D image segmentation via graph-cuts including prior trained shape and motion fields.

### 3.7.3 Testing and Training Data

Following IRB approval, 50 3-D lung CT volumetric frames in ten 4-D CT data (five respiratory phases in 10 subjects) collected with  $3mm$  slice thickness were used for algorithm validations. In addition, 75 3-D lung CT volumes in 15 4-D lung CT data (five phases in 15 patients), also with  $3mm$  slice thickness were downloaded from the Cancer Imaging Archive [67]. Between the two data sources, the size of 4-D lung CT data size ranged from  $512 \times 512 \times 85$  to  $512 \times 512 \times 141$ . All these data were used for the testing. For training, which has the goal of finding the mean and shape variations through PCA analysis, 500 3-D lung nodule CT data sets from the LIDC Cancer Imaging Archive [7] which consist of diagnostic and lung cancer screening thoracic CT scans with marked-up annotated lesions were downloaded and processed to yield mean shapes and the associated eigenvalues and eigenvectors. Since the resolution of the data in LIDC data are different from the spatial resolution of CT data, all data (for both training and testing) was transformed from voxel coordinates to spatial length coordinates.

---

**Algorithm 7: Testing Step**

---

**Input :**

- Parameter settings for graph-cut segmentation,
- Seed points for nodule region and background to perform regional term in graph cut segmentation,
- Volume of interest bounding box initialization,
- Initialized mean shape from training data set.

**Output:**

- 3-D segmented nodule shapes through all respiratory phases.

```
1 for phase10~phase 50 do
2   if phase 10, then
3     Use the initialized mean shape from the training step as a shape prior.
4   else
5     Find the motion field between successive phases (e.g. phase 10 and
6     phase 20)
7     Warp the refined shape obtained from previous phase with the motion
8     field.
9   end
10  end
11  while  $\tau$ (The number of iteration) < Iter do
12    if  $\tau=1$ , then
13      Perform signed distance graph-cuts ASM segmentation incorporating
14      shape prior
15    else
16      Perform segmentation using the refined shape obtained from
17      previous iteration (see equations (26) and (27), and their
18      description for details)
19    end
20    end
21    Shape refinement yields segmented nodule boundaries and refined shape
22    of the 3-D volume
23    if The change in the Energy function between iterations  $\tau$  and  $\tau + 1$  is
24    less than a threshold then
25      STOP
26    end
27  end
28 end
```

---

### 3.7.4 Results of 4-D Lung Nodule Segmentation

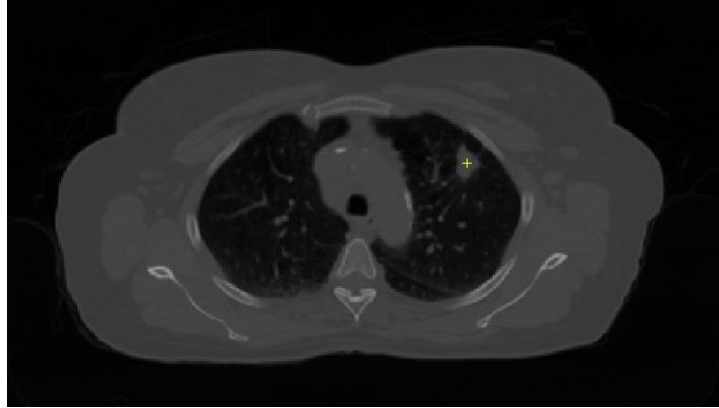
Some nodules occur in the middle of the lung, away from the lung boundary, while others are connected to the surrounding tissues. Kostis et. al defined four classes of pulmonary nodules [80]: Well-circumscribed (located medially in the lung with no significant connections to adjacent vessels), Vascularized (located in the center of the lung with significant connections to neighboring vessels), Juxtapleural (located near the pleural surface, with the major proportion of the nodule periphery connected to the pleural surface), and Pleural tail (located close to the pleural surface with connections through a thin structure to the pleural surface). A review of 25 nodules in our test data showed that nine nodules were vascularized or well-circumscribed, eight were juxtapleural, while the rest were embedded in the heart. Following sections show segmentation results and volumetric analysis as the type of nodules.

#### Well-circumscribed or Vascularized nodules

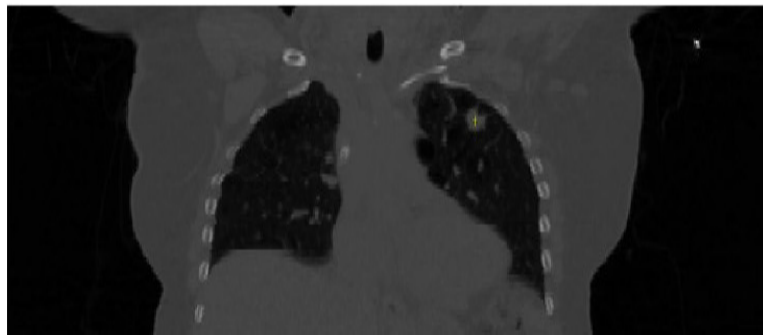
**Results** We performed segmentation of nine 4-D patient data with well-circumscribed or vascularized lung nodules [30, 31]. Figure 22 shows a 2-D axial slice and a 2-D coronal slice for phase 10 of a patient from this category. As maybe seen, the nodule is located in the lung without significant connections to surrounding tissues leading to good contrast between foreground and background.

The first row of Figure 23(a) shows refinement of the mean shape through iterations, and the second row of Figure 23(a) shows evolution of segmentation results for the phase 10 volumes. After the fourth iteration, the energy function (Figure 23(b)) converges.

In accordance with Algorithm 2, we calculate the motion field between times  $t$  and  $t+1$  via the optical flow method (Figure 24) and apply this motion field to warp the mean shape in time. Figure 25 displays 3-D segmented nodule volumes for nine patients through five respiratory phases. Figure 26 shows box plot of the segmented nodule volume for each patient, where the bar represents the mean volume through time. While the nodule volume in patient03 is around  $1cm^3$ , the nodule in patient06 is around  $9cm^3$ . Nodule volumes do



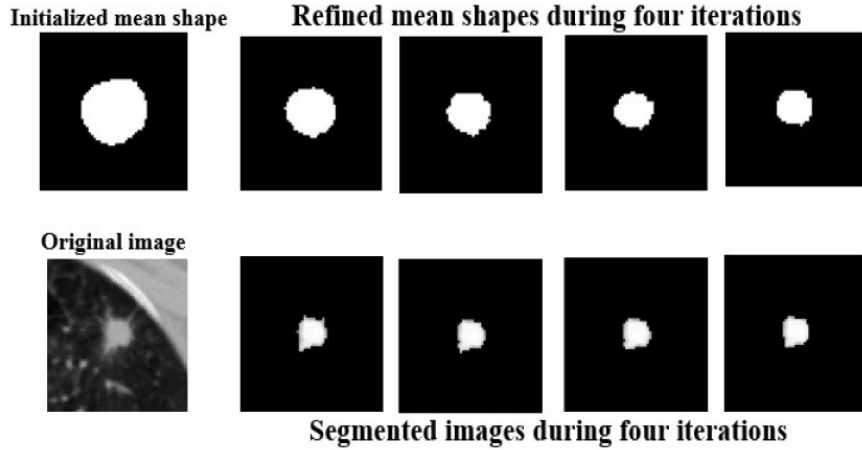
(a) 2D axial slice



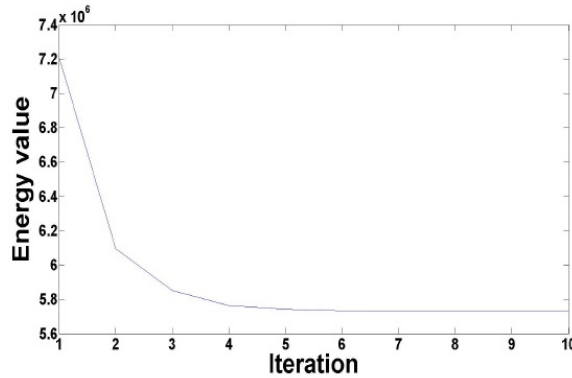
(b) 2D coronal slice

Figure 22. (a) 2-D axial slice and (b) 2-D coronal slice from 3-D image volume for phase 10 of data from a patient with a well-circumscribed nodule. The cross indicates the center of nodule which was manually selected.

not vary greatly through phases. The nodules in patient02 and patient06 are showing larger ranges of the volume size over respiratory phases than other patients since these nodules are located near pleural surface, which can be easily deformed by the lung motion during breathing. Moreover, as shown in Figure 27, the size of the nodules in patient02 from the ground truth is much bigger than the same nodules from our segmentation results because the small proportion of these nodule is connected to pleural surface, so the ground truth include some parts of pleural surface and some adjacent vessels but our segmentation results did not extract parts of pleural surface and adjacent vessels at all.



(a) Shape refinement



(b) Energy

Figure 23. Iterative segmentation of nodule in a single phase. (a) First row: refined mean shapes, second row: segmented nodule utilizing mean shapes from the first row, (b) Plot of the energy function as a function of iterations.

**Metric** To validate our results, we used the Dice Similarity Coefficient (DSC) as introduced in Eq. (22). As may be seen in Figure 28, DSC has a value in the range  $0.5 \sim 0.8$  for each patient and for all phases. Previous authors have proposed techniques which have been performed on 3-D CT data and have reported DSC values in the  $0.8+$  range (see for example, Temesguen *et al.* [97]). An important difference which should be considered is that 3-D CT data (such as for example data in the LIDC Cancer Imaging Archive data sets [7]) have far better spatial resolution than 4-D CT data. Due to the low resolution, the number of voxels making up nodules in 4-D CT data are significantly smaller than that of the LIDC

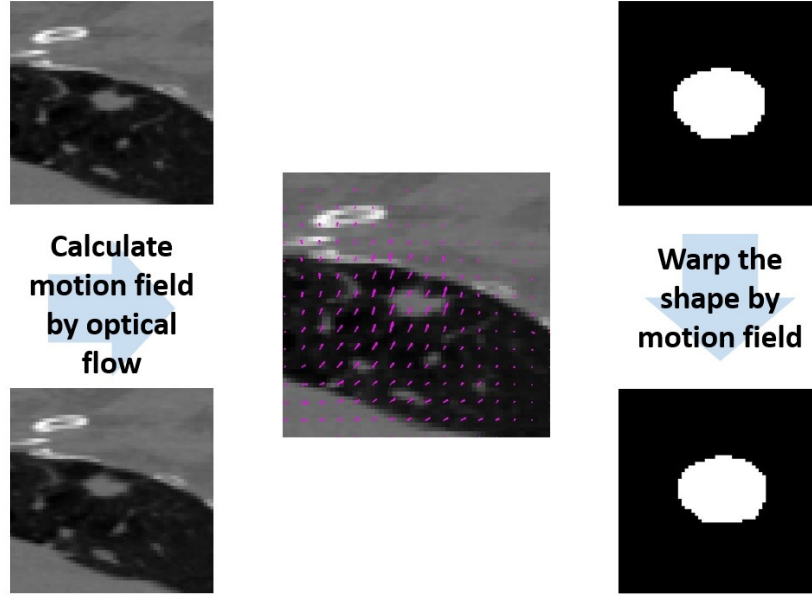


Figure 24. The motion field from the phase 10 to the phase 20 on the cropped 2-D axial slice on the phase 10, and the mean shape and the warped mean shape.

data. Therefore, even a small set of non-matched voxels between the segmented image and ground truth can significantly affect the value of the DSC.

### Juxtapleural nodules

**Results** We also performed 4-D nodule segmentation of eight patients with juxtapleural lung nodules. These nodules are hard to extract with intensity based methods since there is little contrast between nodules and surrounding tissues. For this type of nodule, prior shape information was found to be necessary and effective. Figure 30 shows how the prior shape information affects the segmentation result. For these nodules, it is hard to extract nodules via segmentation technique without prior shape model.

Figure 31 shows evolution of segmentation results for phase 10 volume and refinement of the mean shape through iterations. As shown in Figure 32, we obtain 40 3-D segmented nodule volumes for eight patients through five phases. Figure 33 shows box plot of the nodule volume in  $cm^3$  for each patient. While the nodule in patient11 is around  $12cm^3$ , the nodule in patient16 is around  $3cm^3$ .

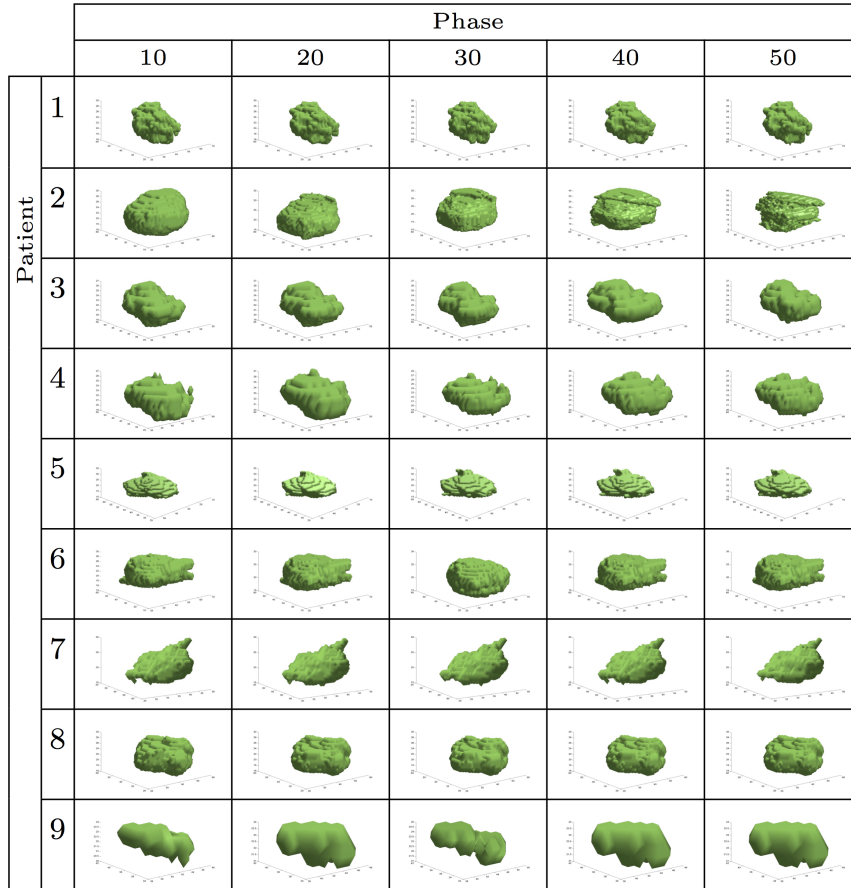
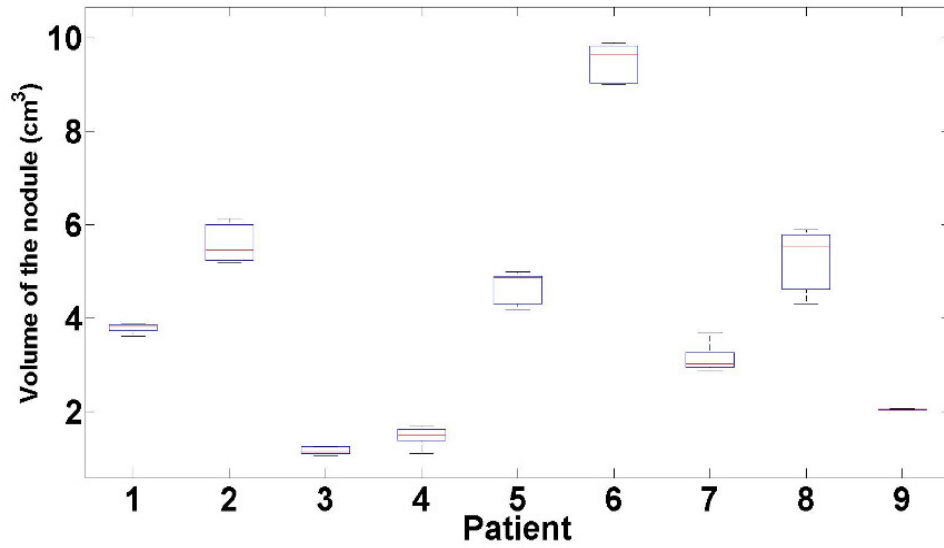
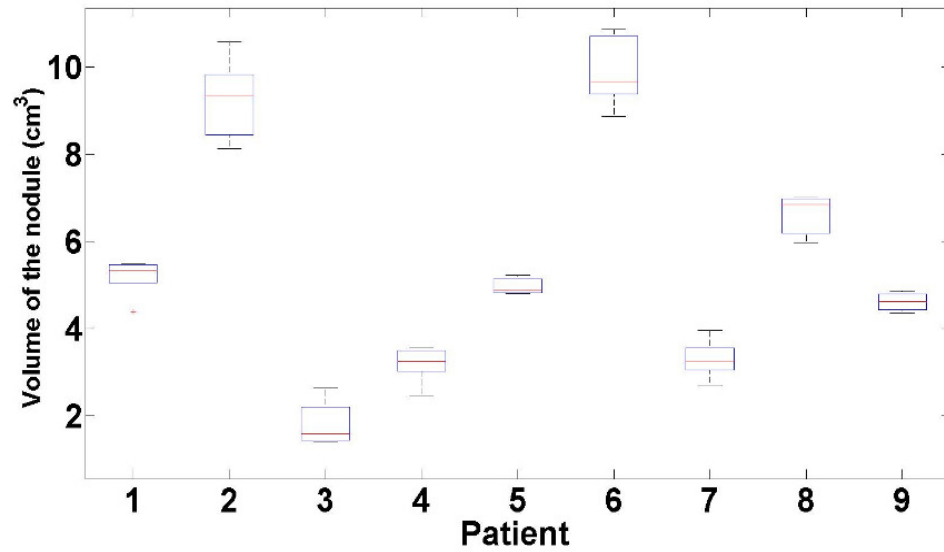


Figure 25. 3-D visualization of well-circumscribed or vascularized nodules for nine patients through five phases.

**Metric** We also determined the *DSC* for validation. For juxtapleural nodules, the values of *DSC* are distributed between 0.55~0.75. This validation suggests that even for the case of juxtapleural nodules, and despite the reduced spatial resolution of the 4-D CT data when compared with previous methods applied to high resolution 3-D CT data (e.g., LIDC data [7]), the proposed 4-D lung nodule segmentation and tracking method works quite well.

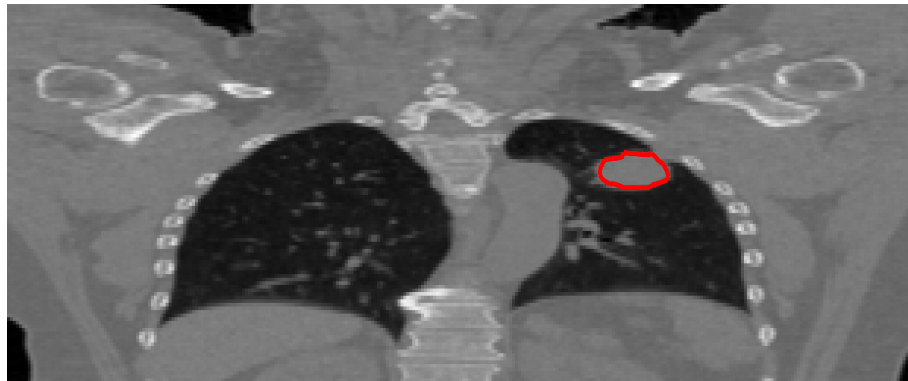


(a) The proposed method

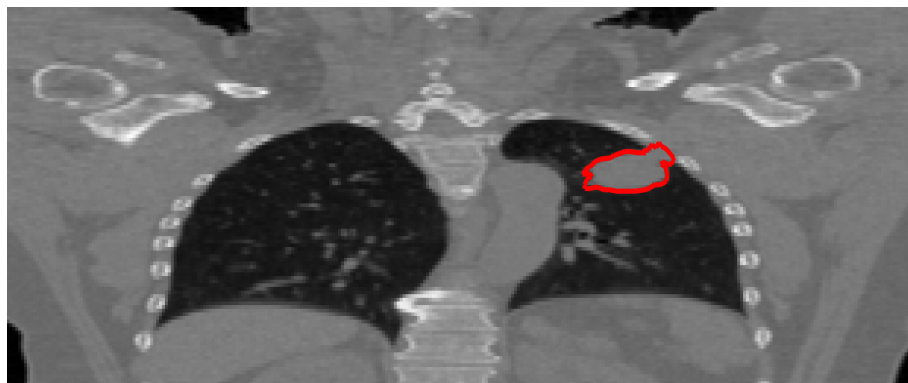


(b) Ground truth

Figure 26. Box plot of the volume of well-circumscribed or vascularized nodules for the nine patients. The bar in the box plot represents the mean volume through five volumetric phases. (a) Results from the proposed method, (b) Ground truth.



(a) Results from the proposed method



(b) Ground truth

Figure 27. Comparison of nodule sizes in 2-D coronal slice between the segmentation result with the ground truth for Patient02. Nodule boundaries are delineated by red lines. The size of the nodules in patient02 from the ground truth is bigger than the same nodules from our segmentation results. (a) Results from the proposed method, (b) Ground truth.

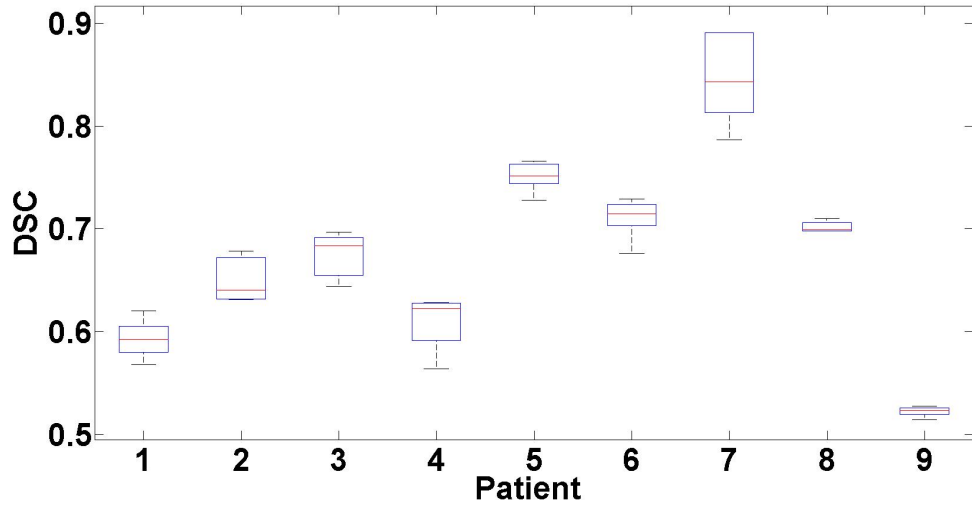
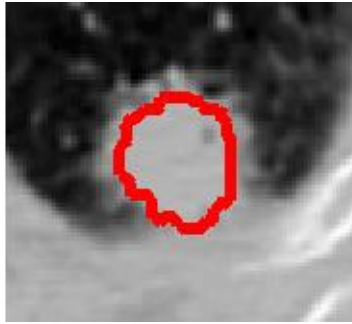


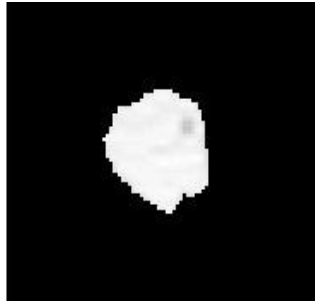
Figure 28. Box plot for the Dice Similarity Coefficient of 4-D segmentation of well-circumscribed or vascularized nodules for nine patients. For each patient, the box plot represents the DSC for five phases through time.



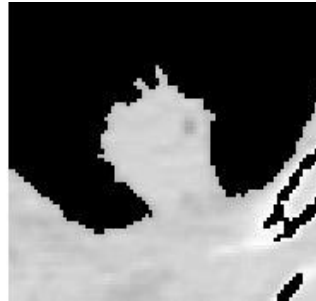
Figure 29. 2-D axial slice having a nodule embedded in surrounding tissues. The arrow indicates the nodule.



(a) Cropped image slice



(b) with shape prior



(c) without shape prior

Figure 30. Comparison in 2-D between the segmentation result with shape prior (b) and without shape prior (c). (a) shows a cropped image slice with ground truth boundary.

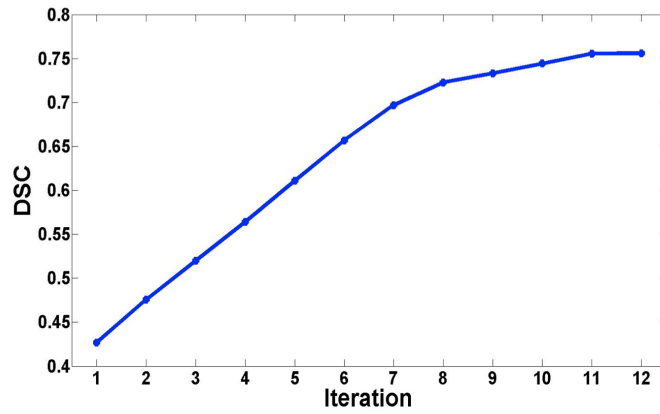
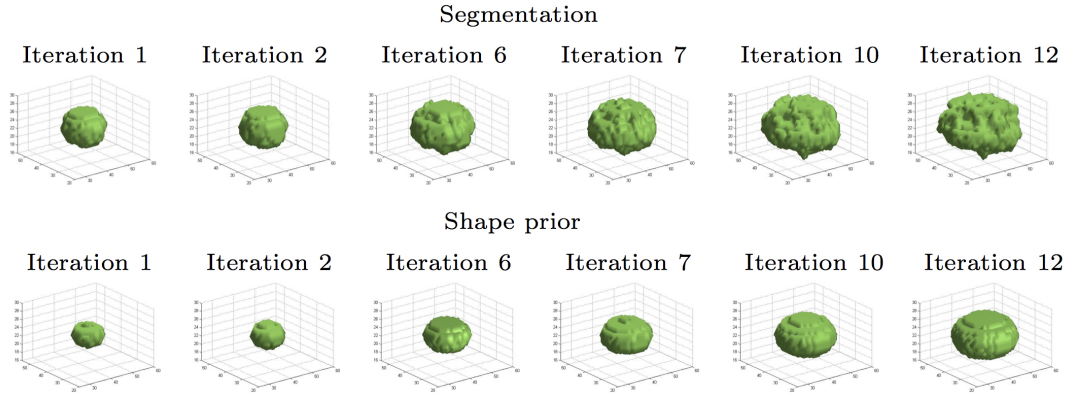


Figure 31. Segmentation and shape prior evolution for a juxtapleural nodule. Columns 1-6 show iterations 1, 2, 6, 7, 10 and the final result in iteration 12 respectively. First row shows segmentation in 3-D and second row shows the zero level set of the signed distance function representation for the refined mean shape. The shape prior for iteration 1 is the mean shape while for subsequent iterations the shape prior used in the iterative graph cuts segmentation is the refined shape prior from the previous iteration. Please see description following Eq. (26) in the text. The third row plots the change in the Dice Similarity Coefficient through iterations showing effectiveness of the adaptive refinement of the shape prior.

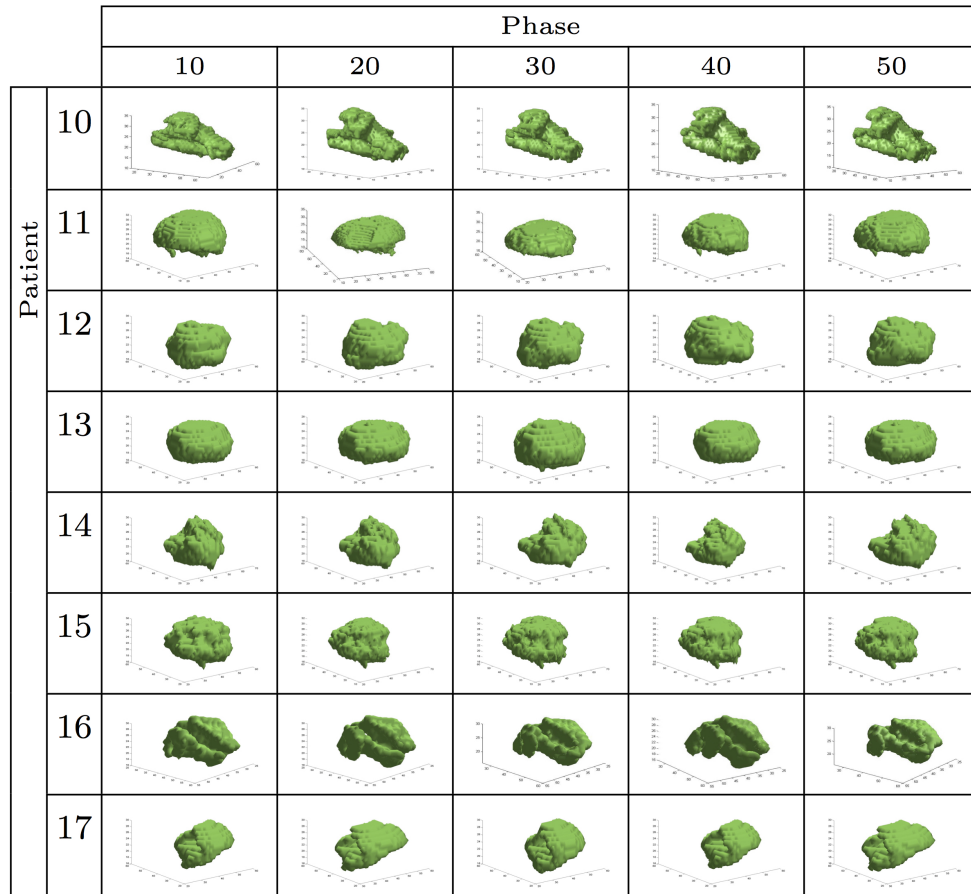
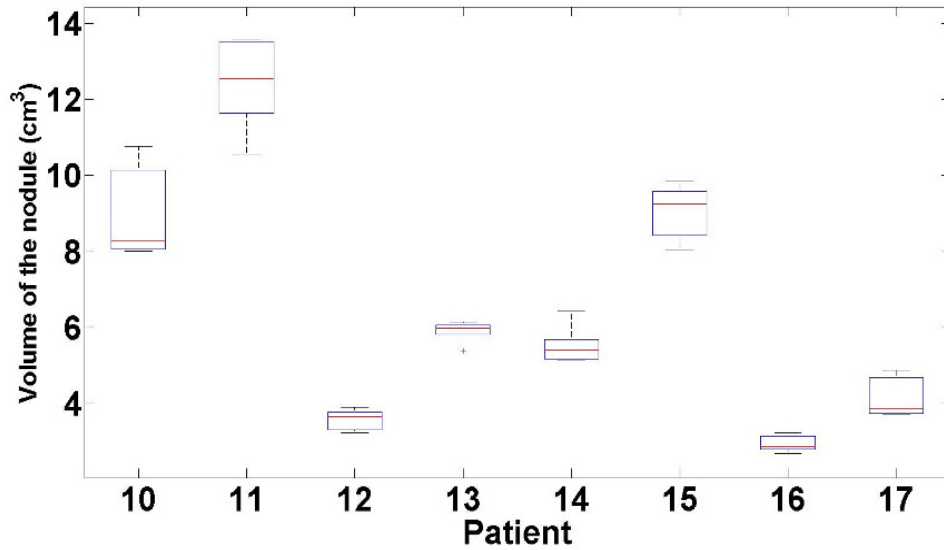
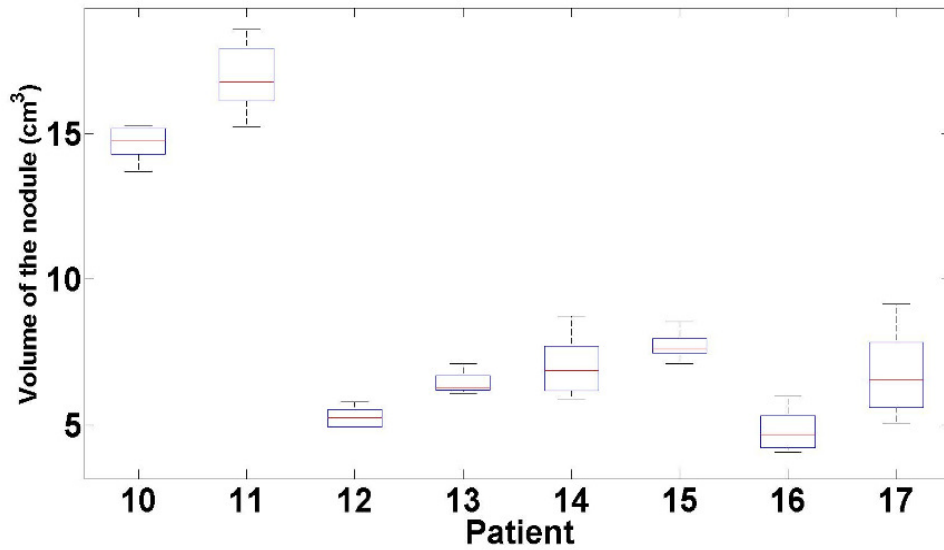


Figure 32. 3-D visualization of juxtapleural nodules for eight patients through five phases.



(a) The proposed method



(b) Ground truth

Figure 33. Box plot of the volume of juxtaleural nodules for eight patients. The bar in the box plot represents the mean volume through five volumetric phases. (a) Results from the proposed method, (b) Ground truth.

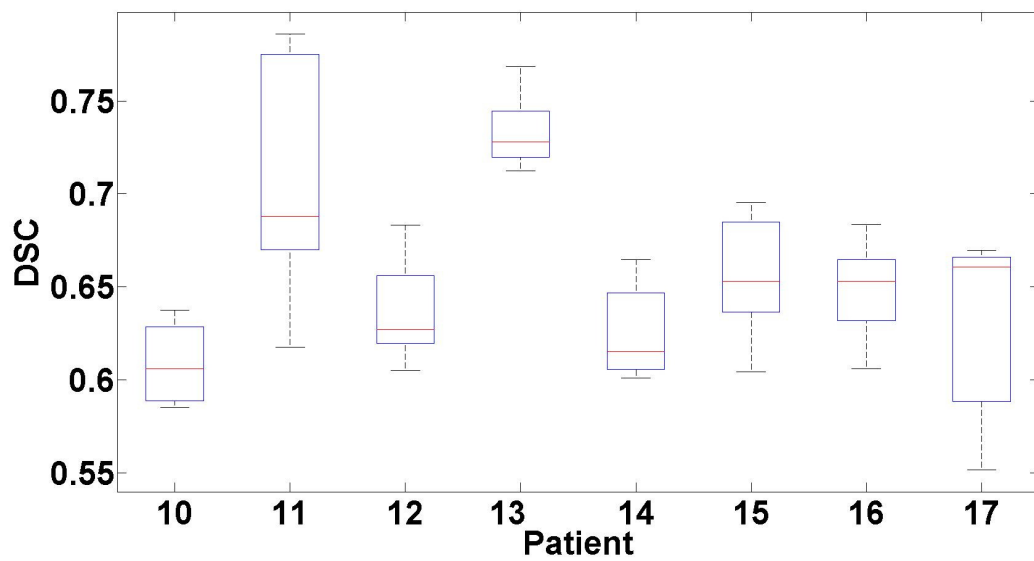


Figure 34. Box plot for the Dice Similarity Coefficient of 4-D segmentation of juxtapleural nodules for eight patients. For each patient, the box plot represents the DSC for five phases through time.

## CHAPTER 4

# STATISTICAL CORRELATION OF CT VENTILATION IMAGES WITH V/Q SPECT

### 4.1 Introduction

Accurate estimation of inter-phase breathing motion in the lung is an important task in radiotherapy treatment. For motion tracking from 4-D CT, deformable image registration (DIR) methods find lung motions. In previous research, quality of a variety of DIR methods for lung CT images has been evaluated. Murphy et al. [102] organized the EMPIRE10 Challenge where several lung image registration algorithms for 4-D lung CT data were evaluated. Although more sophisticated methods as reported in EMPIRE10 Challenge [1] produce more accurate results (with the best approaches improving the TREs in Table 1 by 0.5mm), the availability of code, ease of application, and speed makes use of B-spline registration compelling. In this challenge, methods using Diffeomorphic Transformations [128] and B-spline [26] were highly ranked. Cao et al. [26] performed cubic B-spline registration using Laplacian Regularization Constraint by preserving both tissue volume and vesselness measure. Antink et al. [5] applied Lucas-Kanade optical flow algorithm to evaluate the accuracy of lung registration for DIR-labs data [27]. Song et al. [128] performed lung CT registration by using diffeomorphism for the transformation model and cross correlation for the similarity measure which ran via ANTS [9]. Ruhaak et al. [122] estimated large motion in lung CT by integrating keypoint correspondences into dense deformation. Results from EMPIRE10 challenge may be found on-line [1].

The study of regional pulmonary function to compare 4-D CT ventilation with Single photon emission computed tomography (SPECT) data has received some attention previ-

ously [28, 106, 150, 58]. Castillo et al. [28] studied the correlation of 3-D ventilation from SPECT data with Jacobian-based ventilation or density-based ventilation from 4-D lung CT with DIR method using 4-D local trajectory modeling (4DLTM) [27]. Negahdar et al. [106] used a 3-D optical flow technique (MOFID) to calculate lung deformation fields, and determined regional lung function and correlated with SPECT ventilation  $V_{SPECT}$  and SPECT perfusion  $Q_{SPECT}$ . Yamamoto et al. [150] compared 4-D CT ventilation imaging with SPECT and PET data. They used DIR method regularized based on *Navier – Lamé* equation[73] and found the correlation between Jacobian from 4-D CT and both SPECT and PET data by using Dice similarity coefficient (DSC). Hegi-Johnson et al. [58] determined the correlation of both Jacobian and lung density changes with SPECT images.

In this chapter, we obtained deformation fields during the respiratory cycle from 4-D lung CT by the B-spline registration technique. Moreover, we analyze the aspect of regional functions, Jacobian and principal strain, from the lung deformation over five lung fissures through different respiratory time frame, for example, Phase 10 to 20, Phase 10 to 30, Phase 10 to 40, and Phase 10 to 50, and studied the correlation between both Jacobian and principal strain of deformation images and 3-D V/Q SPECT.

## 4.2 Deformable image registration : B-spline method

Image registration is one of the most important techniques in medical image analysis and has been a significant area of activity for many years [60, 128, 14, 102].

B-spline based techniques [121, 152] are very popular because of their general applicability, ease of use, and computational efficiency. Rueckert et al. [121] used a free-form deformation (FFD) model based on cubic B-splines. B-spline registration has also seen significant application in the area of temporal registration of cardiac images [114, 66].

B-spline based motion estimation has seen much success in other domains as it supports local deformation and can find dense motion fields based on the setting of a control point grid. In the more typical case, motion estimation via B-splines use uniformly spaced control point grids in Cartesian coordinates.

B-splines, which stands for 'basis splines', are the locally supported functions using defined set of control points as mentioned in Section 2.2.1. These are usually described by a free-form deformation (FFD) for image registration. The concept of FFD via B-spline is to deform an object by moving a mesh of control points using B-spline basis functions[66, 114, 121]. B-spline curves consist of several polynomially parametrized pieces sutured together and produced by the summed weighted combination of control points and B-spline basis functions which is a basis for the vector space of piecewise polynomials of a defined degree and continuity[100].

$$C(u) = \sum_{i=0}^{n-1} B_i(u) P_i \quad (30)$$

where  $B_i$  are piecewise polynomial functions and  $P_i$  are control points. We also need to define the knot vector  $U = \{u_0, \dots, u_{m-1}\}$ . B-spline basis functions can then be calculated via Cox-deBoor recurrence relations[42] defining degree  $d$ .

$$B_{i,d}(u) = \frac{u - u_i}{u_{i+d} - u_i} B_{i,d-1}(u) + \frac{u_{i+d+1} - u}{u_{i+d+1} - u_{i+1}} B_{i+1,d-1}(u) \quad (31)$$

$$B_{i,0}(u) = \begin{cases} 1 & u_i \leq u < u_{i+1} \\ 0 & \text{otherwise} \end{cases} \quad (32)$$

with  $\frac{0}{0}$  defined to be 0.  $B_{i,d}$  is a polynomial of order  $d$  (degree) on each interval  $u_i \leq u < u_{i+1}$ . If the degree is zero ( $d = 0$ ), the basis functions are step functions. If the degree is larger than zero, the basis function with degree one ( $d = 1$ ) is a tent function, and the higher the degree as displayed in Figure 35, the smoother the basis functions.

Let knot vector  $U$  be a set of  $m$  non-decreasing numbers,  $u_0 \leq u_1 \leq u_2 \leq \dots \leq u_{m-1}$ . Each  $u_i$  is called knot, and the half-open interval  $[u_i, u_{i+1})$  is referred as the  $i$ -th knot span. If the same value of knot  $u_i$  appear  $k$  times, for example,  $u_i = u_{i+1} = \dots = u_{i+k-1}$ ,  $u_i$  is said

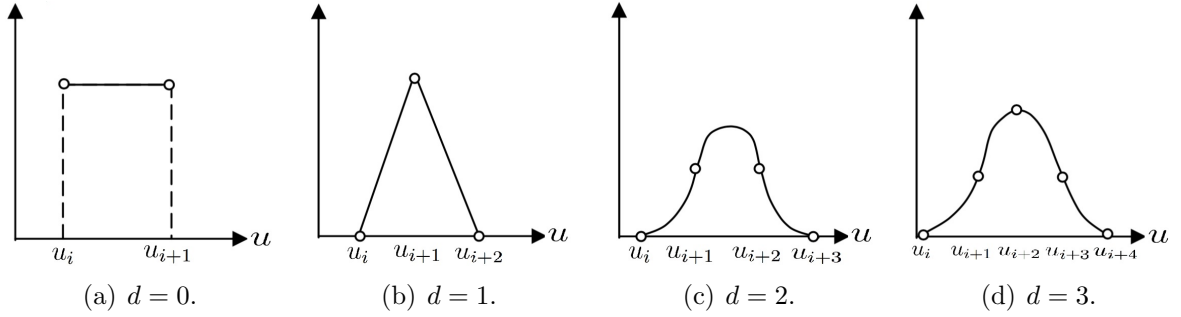


Figure 35. The range of polynomial basis functions. (a) degree  $d = 0$ , (b)  $d = 1$ , (c)  $d = 2$ , (d)  $d = 3$ .

to be a multiple knot of multiplicity  $k$ . If the knots are equally spaced (uniform), B-spline has the uniform basis function, otherwise, it has non-uniform basis function.

A linear basis function (Figure 35 (b)) provides only positional continuity, which is called  $C^0$  continuity. A quadratic basis function (Figure 35 (c)) gives positional and slope continuity, which is called  $C^1$  continuity. For a cubic basis function (Figure 35 (d)),  $C^2$  continuity is provided and it has positional, slope and curvature continuity.

Consider the cubic B-spline functions which we use for motion estimation. The cubic B-spline functions will have four segments defined over five control points. In the range of  $u \in [0, 1]$ , we define the cubic basis functions for each segment. By calculating Eq. (32), we can obtain cubic B-spline basis functions already stated in Eq. (3),

$$\begin{aligned}
 B_0(u) &= (1 - u)^3 / 6 \\
 B_1(u) &= (3u^3 - 6u^2 + 4) / 6 \\
 B_2(u) &= (-3u^3 + 3u^2 + 3u + 1) / 6 \\
 B_3(u) &= u^3 / 6.
 \end{aligned} \tag{33}$$

These function can be written in matrix notation as well.

$$\mathbf{B}(u) = [B_0(u) \ B_1(u) \ B_2(u) \ B_3(u)] = \mathbf{UM} = [u^3 \ u^2 \ u^1 \ u^0] \frac{1}{6} \begin{bmatrix} 1 & -3 & 3 & 1 \\ 0 & 3 & -6 & 3 \\ 0 & 3 & 0 & -3 \\ 0 & 1 & 4 & 1 \end{bmatrix} \quad (34)$$

In order to draw each segments of a 2-D curve (Eq. (30)), we need to calculate  $C(u)$  as weighted combination of the basis functions. When we have the  $i_{th}$  control point  $p_i$

$$\mathbf{C}(u) = \mathbf{UMP} = [u^3 \ u^2 \ u^1 \ u^0] \frac{1}{6} \begin{bmatrix} 1 & -3 & 3 & 1 \\ 0 & 3 & -6 & 3 \\ 0 & 3 & 0 & -3 \\ 0 & 1 & 4 & 1 \end{bmatrix} [p_i \ p_{i+1} \ p_{i+2} \ p_{i+3}] \quad (35)$$

As was mentioned in Section 2.2.1, in order to formulate cubic B-spline parametrized volumes under Free Form Deformation (FFD), the set of control points  $P_{i,j,k}$  is set up on the  $n_x \times n_y \times n_z$  mesh with uniform spacing  $\delta$  in the domain of 3-D image volume  $\Omega = \{(x, y, z) | 0 \leq x < X, 0 \leq y < Y, 0 \leq z < Z\}$ . And then, the 3-D tensor product of 1-D cubic B-splines parametrizing the volume is written as follows,

$$T_{local}(x, y, z) = \sum_{l=0}^3 \sum_{m=0}^3 \sum_{n=0}^3 B_l(u) B_m(v) B_n(w) P_{i+l, j+m, k+n}. \quad (36)$$

where  $i = \lfloor x/n_x \rfloor - 1$ ,  $j = \lfloor y/n_y \rfloor - 1$ ,  $k = \lfloor z/n_z \rfloor - 1$ ,  $u = x/n_x - \lfloor x/n_x \rfloor$ ,  $v = y/n_y - \lfloor y/n_y \rfloor$ ,  $w = z/n_z - \lfloor z/n_z \rfloor$ .

The spacing  $\delta$  of control points determines the scale of local deformations. The larger the spacing  $\delta$  of control points, the more global the generated non-rigid deformations, in order to compute the motion fields between the source image  $I$  and the target image  $J$  via 3-D cubic B-splines, the energy function should be defined and minimized with optimization scheme as follows.

$$E_{total}(T) = -E_{similarity}(I(t), T(J(t))) + \lambda E_{smooth}(T). \quad (37)$$

where  $T$  is the local transformation via 3-D cubic B-splines and  $\lambda$  is the weight which defines the tradeoff between the alignment  $E_{similarity}$  of the two image volumes  $I(t)$  and  $T(J(t))$  and the smoothness  $E_{smooth}(T)$  of the transformation.

The smoothness term  $E_{smooth}(T)$  is required to constrain the spline-based FFD transformation to be smooth. Several kinds of penalty term can be used for this. Rueckert et al.[121] applied the 3-D version of a thin-plate of metal bending energy.

$$E_{smooth}(T) = \frac{1}{V} \int_0^X \int_0^Y \int_0^Z \left[ \left( \frac{\partial^2 T}{\partial x^2} \right)^2 + \left( \frac{\partial^2 T}{\partial y^2} \right)^2 + \left( \frac{\partial^2 T}{\partial z^2} \right)^2 + 2 \left( \frac{\partial^2 T}{\partial xy} \right)^2 + 2 \left( \frac{\partial^2 T}{\partial yz} \right)^2 + 2 \left( \frac{\partial^2 T}{\partial xz} \right)^2 \right] dx dy dz. \quad (38)$$

For the  $E_{similarity}$ , as we mentioned in Section 2.2.2, Sum of squared difference (SSD), Correlation coefficient (CC), Mutual information (MI), etc. can be used. And then, by the optimization of the total energy function, the optimal transformation will be calculated, which makes the source image  $I(t)$  and registered image  $T(J(t))$  into the best possible alignment. This transformation  $T$  will be considered as the motion field between the two image volumes.

Since the B-spline method requires parameter settings, e.g., control point spacing, and a regularization weight, we performed a number of experiments on limited data sets to determine the optimal parameter settings for the B-spline registration algorithm and arrived at five voxel spacing for the distance between the control points and 0.03 for the regularization weight (we used cubic B-splines). In order to measure the quality of B-spline registration for 4-D thoracic CT, we computed the target registration error (TRE) for DIR-lab [27] and POPI model [142] data between Phase 10 (end-inhale) and Phase 50 (end-exhale). The value of TRE for POPI model and DIR-labs data all with identical B-spline control point grid density and parameter setting is shown in Table 4.

With parameter settings as stated above, we calculated motion fields between Phase 10 and Phase 50 of 11 4-D lung CT data with the B-spline registration method employing SSD as the intensity matching constraint.

### 4.3 CT Ventilation Images from Lung Deformation

4-D CT provides structural and anatomical information during tidal breathing which maybe used to quantify deformation fields via DIR methods and subsequently to measure mechanical properties of the lung tissue including Jacobian and strain of deformation at voxel resolutions and as a function of time. Subsequent to B-spline deformable registration - 3-D deformation fields between successive respiratory phases of the 4-D CT data were determined and subsequently measures of regional lung function were computed.

#### 4.3.1 Measure of regional functions

Subsequent to estimation of the motion fields  $(u, v, w)$  between phase 10 and any other phase during the respiratory cycle (this approach, the so called Lagrangian frame of reference, assumes phase 10 to be the undeformed state and later phases to be deformed states), the deformation gradient tensor,  $F$ , maybe calculated for each 3-D voxel location based on partial derivatives of the components of the computed displacement field.

$$F = \begin{bmatrix} 1 + u_x & u_y & u_z \\ v_x & 1 + v_y & v_z \\ w_x & w_y & 1 + w_z \end{bmatrix}. \quad (39)$$

The Lagrangian strain tensor,  $E$ , can then be determined,

$$E = \frac{1}{2} (F^T F - I). \quad (40)$$

where  $I$  is the identity matrix. Diagonalizing the strain tensor yields the principal strain values  $(\lambda_1, \lambda_2, \lambda_3)$  and directions  $(V_1, V_2, V_3)$ .

$$E = R\Lambda R^{-1} = \begin{bmatrix} V_1 & V_2 & V_3 \end{bmatrix} \begin{bmatrix} \lambda_1 & 0 & 0 \\ 0 & \lambda_2 & 0 \\ 0 & 0 & \lambda_3 \end{bmatrix} \begin{bmatrix} V_1 \\ V_2 \\ V_3 \end{bmatrix}, \quad (41)$$

where  $R$  is a rotation matrix, and  $\Lambda$  is a diagonal matrix. The principal strain values,  $\lambda_1$ ,  $\lambda_2$ , and  $\lambda_3$ , correspond to the maximum stretch ( $\lambda_1$ ), medium stretch values ( $\lambda_2$ ) and minimum stretch values ( $\lambda_3$ ) respectively. The principal strain vectors,  $V_1$ ,  $V_2$ , and  $V_3$ , correspond to the directions of the principal axes of strain tensor ellipsoid as shown in Figure 36.

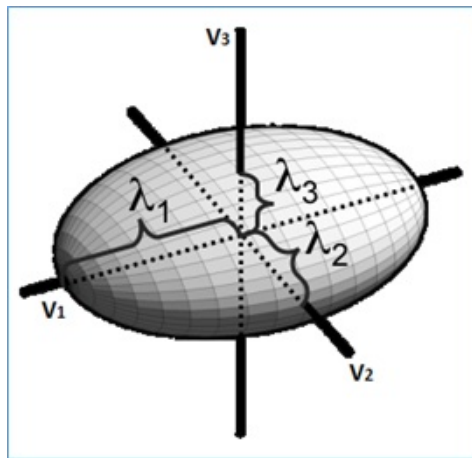


Figure 36. Strain tensor ellipsoid.

Moreover, Jacobian ( $J$ ) of the deformation can be calculated as the determinant of  $F$ .

$$J = \det(F) \quad (42)$$

The value of Jacobian is directly related to the local change in the lung volume, which is one when there is no deformation, less than one for contraction, and larger than one when there is local expansion of volume. The Jacobian determinant can never be negative with zero being a point of singularity.

Since  $R^{-1} = R^T$ , Eq. (40) and Eq. (41) can be rewritten as follows,

$$E = \frac{1}{2} (F^T F - I) = R \Lambda R^T \quad (43)$$

$$F^T F = 2 \left( R \Lambda R^T + \frac{1}{2} R R^T \right) = 2 \left( R \left( \Lambda + \frac{1}{2} I \right) R^T \right) \quad (44)$$

Since  $F$  is a  $3 \times 3$  tensor, applying the determinant to both sides of the Eq. (44) yields:

$$(\det(F))^2 = 8 \det \left( \Lambda + \frac{1}{2} I \right) \quad (45)$$

As Eq. (42),

$$J = \sqrt{(2\lambda_1 + 1)(2\lambda_2 + 1)(2\lambda_3 + 1)} \quad (46)$$

### 4.3.2 Data

Following IRB approval, 22 patients were enrolled in the study. The 11 CT data had 3mm slice thickness and were collected on a Philips Brilliance Big Bore CT scanner at the James Graham Brown Cancer Center at the University of Louisville. The size of 4-D data ranged from  $512 \times 512 \times 85$  to  $512 \times 512 \times 100$  through five phases. Moreover, 10 lung CT data were used from DIR-lab (Case01 - Case10) [27]. The size of 4-D data ranged from  $256 \times 256 \times 94$  to  $512 \times 512 \times 136$  through five phases which had 2.5mm slice thickness. Also one lung CT data were used from POPI-model [142]. The size of 4-D data are  $512 \times 512 \times 141$  through five phases which had 2mm slice thickness.

### 4.3.3 Results

We computed the principal strain values,  $\lambda_1$ ,  $\lambda_2$ , and  $\lambda_3$ , the principal strain vectors,  $V_1$ ,  $V_2$ , and  $V_3$ , and Jacobian  $J$  from lung deformation derived by B-spline registration on 4-D CT data for all 22 subjects. The 3-D scalar ventilation images volume mapping regional

mechanics of the lung is masked by the segmented lung volume calculated by Graph-cuts segmentation [32]. Moreover, in order to analyze the aspect of regional mechanics over five lung lobes namely the left upper lobe (LUL), left lower lobe (LLL), right upper lobe (RUL), right middle lobe (RML), and right lower lobe (RLL), we divided each ventilation image volume to five volumes on the coronal orientation as shown in Figure 37.

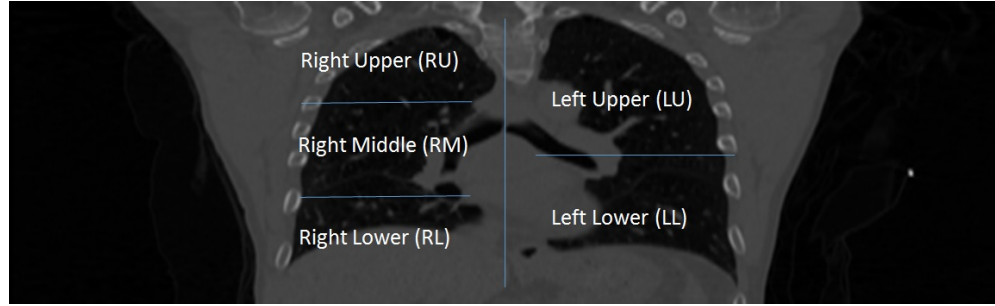
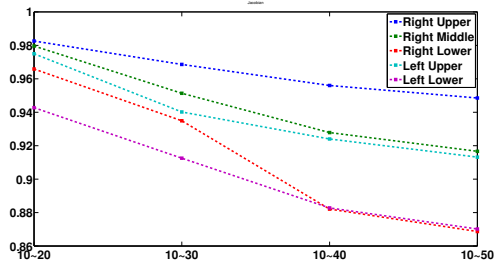


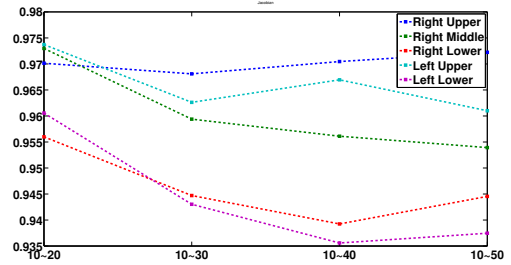
Figure 37. The sectioning of lung volume to left upper lobe (LUL), left lower lobe (LLL), right upper lobe (RUL), right middle lobe (RML), and right lower lobe (RLL). Ideally, this should be done based on lung fissures and this was done as a rough approximation.

Figure 38 shows the Jacobian ventilation image over five fissures through different respiratory phases. Figure 38(a) ~ 38(e) display plot of the average Jacobian values for five patients. Right lower and left lower parts of the lungs have smaller Jacobian values at the end-expiratory phase which means that for these regions there is more contraction. Also, with increasing time, from Phase10~20 to Phase10~50, the magnitude of contraction becomes larger. The overall result of Jacobian plot can be seen in Figure 38(f) – averaged over 22 patients. Even though we studied over all 22 patients, since some patients do not have intact lung volume, for example, almost half of left lung, or of both lungs is occupied by the mass of another tissues, those cases are ignored to calculate the average of regional lung functions.

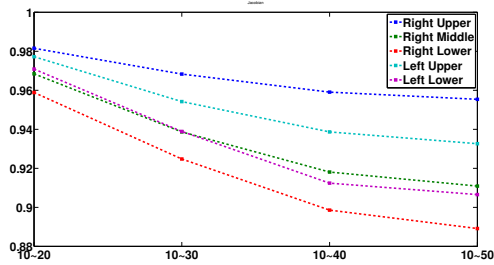
As shown in Figures 39, 40, and 41, we also plot the principal strain values,  $\lambda_1$ ,  $\lambda_2$ , and  $\lambda_3$ , through different respiratory phases as well.



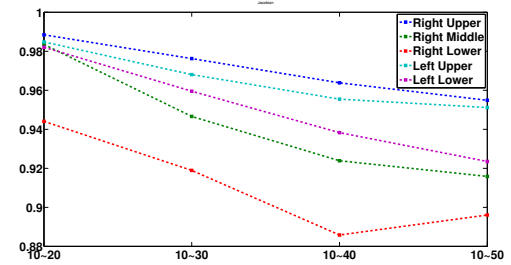
(a) Patient 01



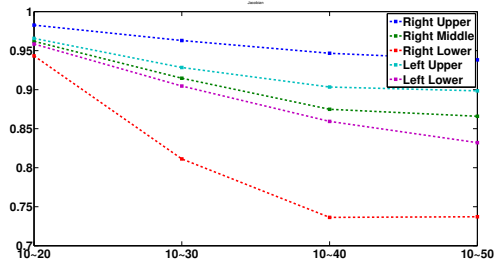
(b) Patient 02



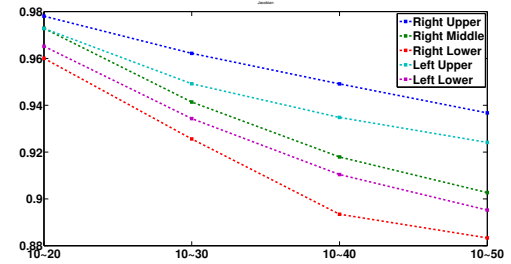
(c) Patient 03



(d) Patient 04

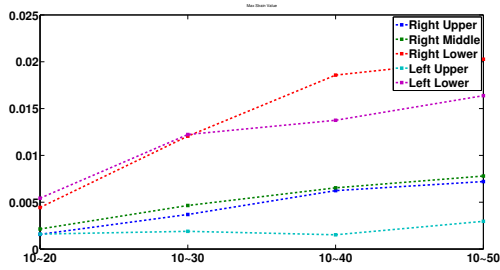


(e) Patient 05

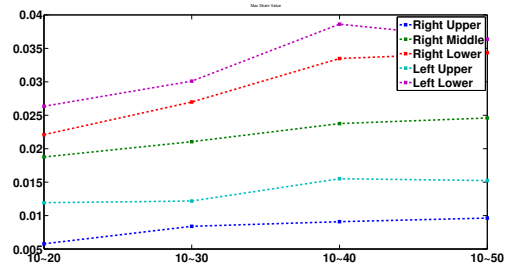


(f) Average over all patients

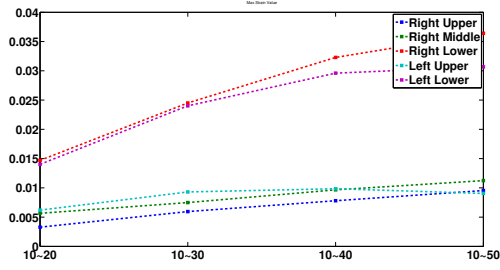
Figure 38. Average Jacobian measure over five lung lobes through respiratory phases, always relative to phase 10. (a) patient 01, (b) patient 02, (c) patient 03, (d) patient 04, (e) patient 05, (f) Average over 22 patients.



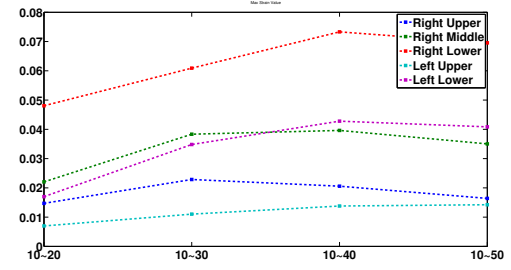
(a) Patient 01



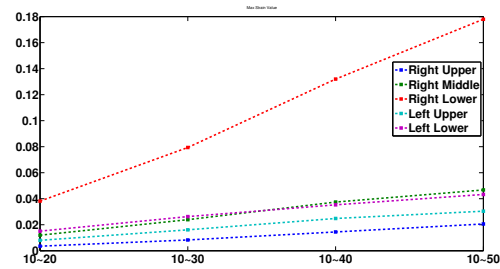
(b) Patient 02



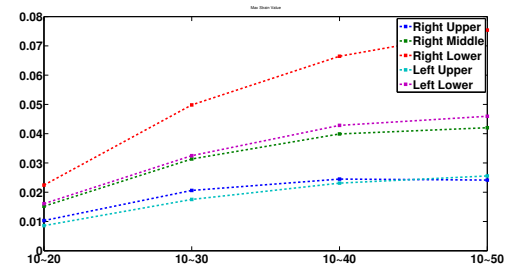
(c) Patient 03



(d) Patient 04

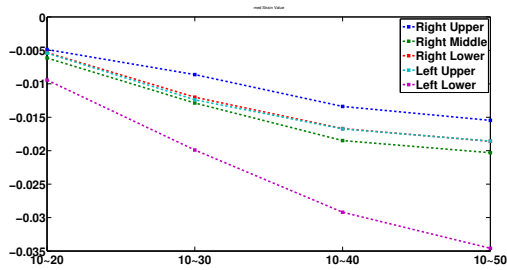


(e) Patient 05

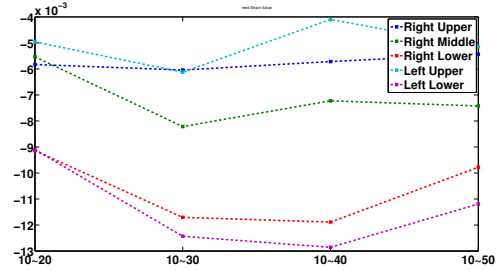


(f) Average over all patients

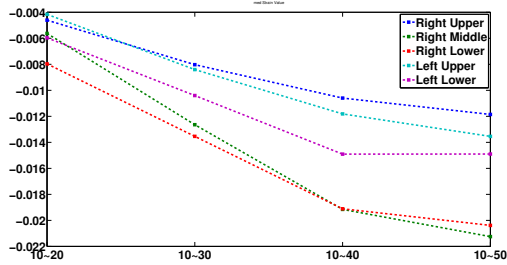
Figure 39. Average maximum strain value  $\lambda_1$  over five lung lobes through respiratory phases, always relative to phase 10. (a) patient 01, (b) patient 02, (c) patient 03, (d) patient 04, (e) patient 05, (f) Average over 22 patients.



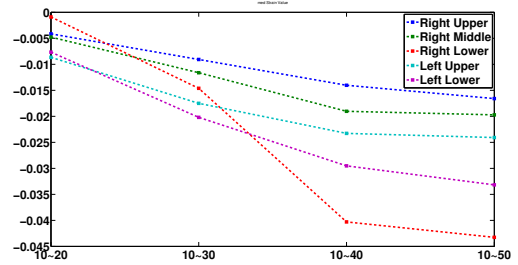
(a) Patient 01



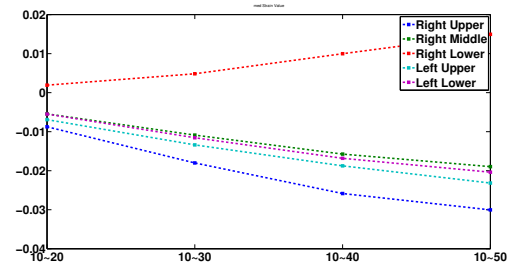
(b) Patient 02



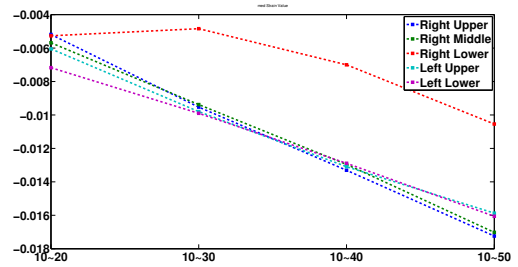
(c) Patient 03



(d) Patient 04

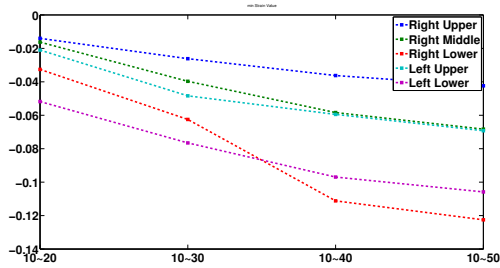


(e) Patient 05

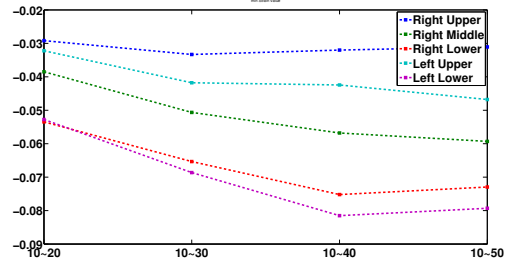


(f) Average over all patients

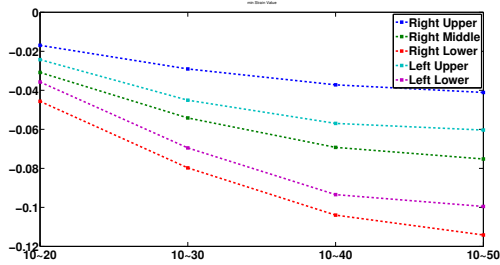
Figure 40. Average minimum strain value  $\lambda_1$  over five lung lobes through respiratory phases, always relative to phase 10. (a) patient 01, (b) patient 02, (c) patient 03, (d) patient 04, (e) patient 05, (f) Average over 22 patients.



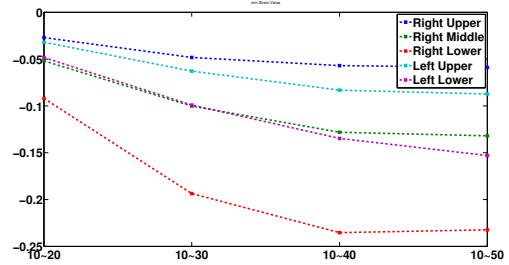
(a) Patient 01



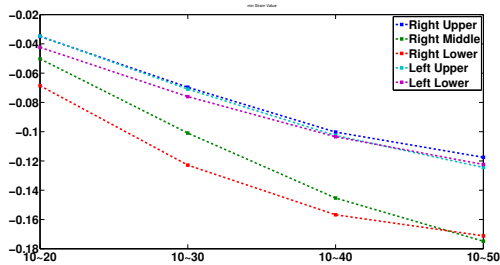
(b) Patient 02



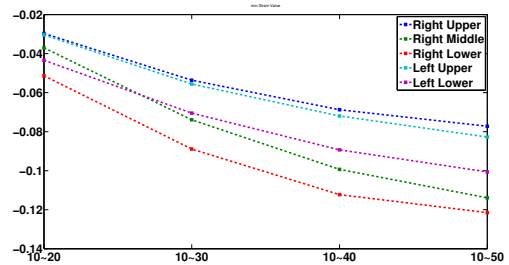
(c) Patient 03



(d) Patient 04



(e) Patient 05



(f) Average over all patients

Figure 41. Average minimum strain value  $\lambda_1$  over five lung lobes through respiratory phases, always relative to phase 10. (a) patient 01, (b) patient 02, (c) patient 03, (d) patient 04, (e) patient 05, (f) Average over 22 patients.

#### 4.4 Statistical correlation of CT ventilation imaging and V/Q SPECT in patients with lung cancer

Single photon emission computed tomography (SPECT) lung imaging provides functional information using radioactive tracers with SPECT ventilation and SPECT perfusion imaging. We performed B-spline deformable registration and measured regional lung function in 11 lung cancer patients. Furthermore, in all subjects, we registered the max-inhale CT volume to both  $V_{SPECT}$  and  $Q_{SPECT}$  data sets using the Demon's non-rigid registration algorithm. Subsequently, statistical correlation between CT ventilation images, Jacobian and strain values, with both  $V_{SPECT}$  and  $Q_{SPECT}$  was undertaken. Through statistical analysis with the Spearman's rank correlation coefficient ( $\rho$ ), we found that Jacobian values have the highest correlation with both  $V_{SPECT}$  and  $Q_{SPECT}$ .

##### 4.4.1 Co-Registration of CT and SPECT

In order to perform co-registration of SPECT and CT, we used the Demons algorithm [136] using MATITK [35]. The Demons algorithm is a popular for non-rigid image registration due to effective computation and easy implementation. This algorithm is based on deformation caused by force vectors and regularized by a Gaussian convolution. This force vector was derived from the optical flow equations. Before applying the Demons algorithm, we upsampled the SPECT data to match the 3-D CT image matrix size with tricubic interpolation. We also performed Graph-cuts segmentation [29] to extract 3-D lung volume for phase 10 of the 4-D CT data since phase 10 (maximum lung volume) is to be the undeformed state and Phase 50 (minimum lung volume) is to be deformed states. This was done to improve the registration of SPECT with CT as segmented masks provide clearer lung boundary information than the original image volume. Figure 42 (e), and (f) show registered  $V_{SPECT}$  and  $Q_{SPECT}$  as 2-D mid-coronal slices from 3-D volumes for one data set.

#### 4.4.2 Correlation between CT Ventilation Images and SPECT data

The principal strain values,  $\lambda_1$ , and  $\lambda_3$ , correspond to the maximum stretch ( $\lambda_1$ ) and minimum stretch values ( $\lambda_3$ ) respectively. Figure 42 (b), (c), and (d) show the principal strain value images on 2-D mid-coronal slices calculated from motion fields between Phase 10 (end-inhale) and Phase 50 (end-exhale). Moreover, the Jacobian map is shown in Figure 42 (a).

Having principal strain values, we then determined how principal strains correlated on a point-by-point basis with both  $V_{SPECT}$  and  $Q_{SPECT}$  scans. For statistical analysis, we used the Spearman's rank correlation coefficient ( $\rho$ ) which is a non-parametric measure of statistical dependence between two variables. The value of  $\rho$  is in the range  $[-1, 1]$ .

#### 4.4.3 Data

Following IRB approval, 11 patients were enrolled in the study. The CT data had 3mm slice thickness and were collected on a Philips Brilliance Big Bore CT scanner at the James Graham Brown Cancer Center at the University of Louisville. The size of 4-D data ranged from  $512 \times 512 \times 85$  to  $512 \times 512 \times 100$  through five phases. Moreover, in the same subjects 11 lung SPECT data were also obtained on a Philips ADAC SPECT scanner at the James Graham Brown Cancer Center. The size of SPECT data ranged from  $128 \times 128 \times 53$  to  $128 \times 128 \times 92$  with 4.64mm slice thickness.

#### 4.4.4 Results

We computed the Spearman's correlation coefficient ( $\rho$ ) and p-value for all 11 subjects as shown in Table 5 and Figure 43 - the correlation was carried out on a point by point basis subsequent to upsampling the SPECT data. Overall,  $V_J$  shows the strongest correlation with  $V_{SPECT}$ . Moreover, among strain values,  $V_{\lambda_3}$  had higher correlation with  $V_{SPECT}$  than  $V_{\lambda_1}$  or  $V_{\lambda_2}$ .

Table 6 shows the Spearman's correlation coefficient ( $\rho$ ) and p-value between  $Q_{SPECT}$ , and principal strain values and Jacobian from 4-D CT data once again for all 11 subjects.

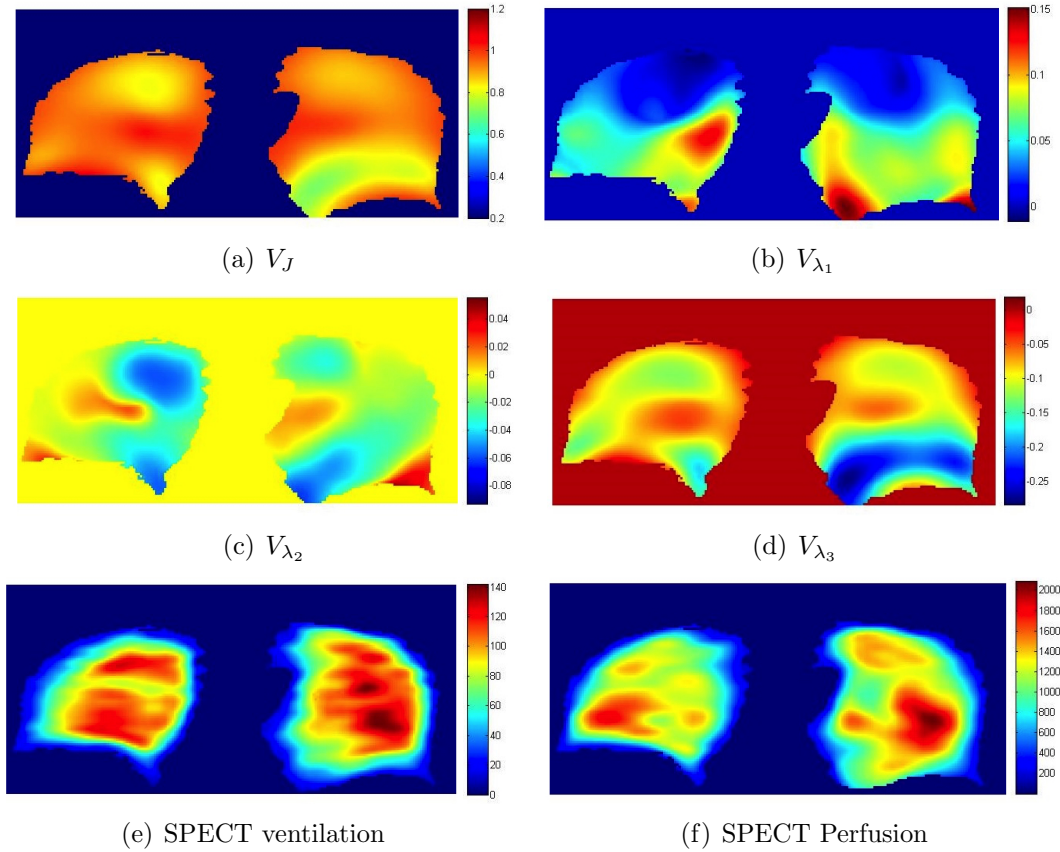


Figure 42. 2-D mid-coronal slices of CT Ventilation image volumes computed between Phase10 and Phase50 of 4-D lung CT data, compared with registered SPECT ventilation and perfusion. (a) The calculated Jacobian image, (b) the maximum principal strain image, (c) the medium principal strain image, (d) the minimum principal strain image, (e) SPECT ventilation image, (f) SPECT perfusion image

This table shows that  $V_J$  shows the strongest correlation with  $Q_{SPECT}$ . The Jacobian is strongly related to both SPECT ventilation and perfusion. The value of  $V_{\lambda_3}$  also had higher correlation with SPECT perfusion data than  $V_{\lambda_1}$  or  $V_{\lambda_2}$ . Most  $\rho$  in the Table 5 and 6 show negative values, which means that the values of CT ventilation maps tend to decrease, the values of  $V_{SPECT}$  or  $Q_{SPECT}$  maps increase. Figure 44 shows the box plot for the data in Table 6.

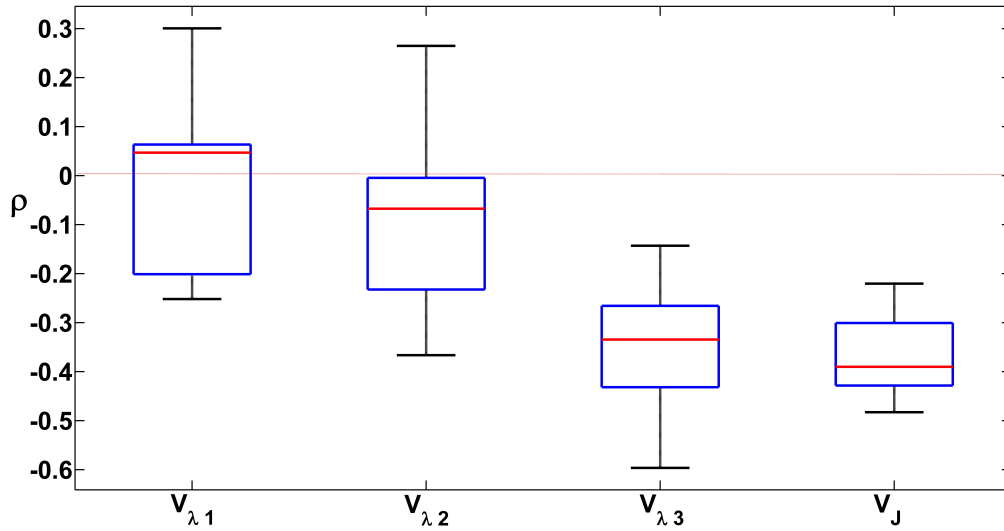


Figure 43. The box plot of the Spearman's correlation coefficient ( $\rho$ ) between  $V_{SPECT}$  and both Jacobian and principal strain values from 4-D CT data for all 11 lung cancer patients.

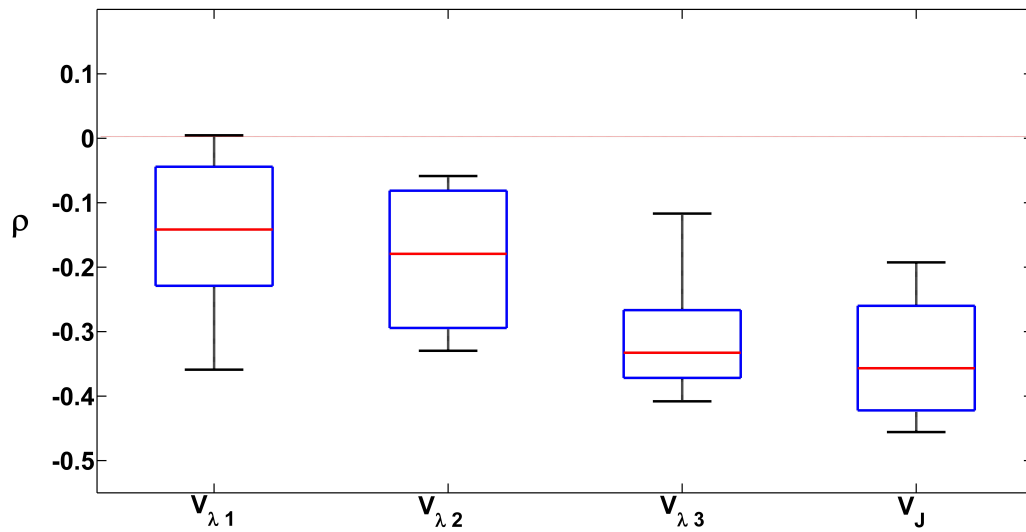


Figure 44. The box plot of the Spearman's correlation coefficient ( $\rho$ ) between  $Q_{SPECT}$  and both Jacobian and principal strain values from 4-D CT data for all 11 lung cancer patients.

TABLE 4

The target registration error (TRE) of B-spline registration for POPI model and DIR-lab 4-D CT data (Case01 - Case10). TRE is averaged over all slices and all frames. Although more sophisticated methods as reported in EMPIRE10 Challenge [1] produce more accurate results (with the best approaches improving these TREs by  $\sim 0.5\text{mm}$ ), the availability of code, ease of application and speed makes use of B-spline registration compelling.

	<b>TRE (mm)</b>
<b>POPI</b>	$1.32 \pm 0.83$
<b>Case 01</b>	$1.45 \pm 1.23$
<b>Case 02</b>	$1.58 \pm 1.91$
<b>Case 03</b>	$1.42 \pm 1.22$
<b>Case 04</b>	$1.97 \pm 1.65$
<b>Case 05</b>	$1.81 \pm 2.01$
<b>Case 06</b>	$1.26 \pm 1.43$
<b>Case 07</b>	$1.33 \pm 0.70$
<b>Case 08</b>	$1.47 \pm 1.13$
<b>Case 09</b>	$1.12 \pm 0.71$
<b>Case 10</b>	$1.28 \pm 1.40$

TABLE 5

The Spearman's correlation coefficient ( $\rho$ ) between  $V_{SPECT}$  and both Jacobian and principal strain values from 4-D CT data for all 11 lung cancer patients. The p-value for all cases is ' $< 0.005$ '.

	$V_{\lambda_1}$	$V_{\lambda_2}$	$V_{\lambda_3}$	$V_J$
1	-0.0274	-0.1581	-0.2996	-0.2336
2	-0.1237	-0.3002	-0.3822	-0.4365
3	-0.2268	-0.2369	-0.3966	-0.3901
4	0.3005	0.2648	-0.5963	-0.3736
5	0.0636	-0.2188	-0.4609	-0.4827
6	0.0470	-0.0674	-0.4435	-0.4315
7	-0.2518	-0.3663	-0.2666	-0.3984
8	0.0616	0.0016	-0.3344	-0.3105
9	-0.2430	-0.0373	-0.2653	-0.2975
10	0.0633	-0.0229	-0.1429	-0.2204
11	0.1220	0.0423	-0.2387	-0.4185
<b>mean</b>	<b>-0.0195</b>	<b>-0.0999</b>	<b>-0.3479</b>	<b>-0.3630</b>

TABLE 6

The Spearman's correlation coefficient ( $\rho$ ) between  $Q_{SPECT}$  and principal strain values from 4-D CT data for all 11 lung cancer patients. The p-value for all cases is ' $< 0.005$ '.

	$V_{\lambda_1}$	$V_{\lambda_2}$	$V_{\lambda_3}$	$V_J$
1	-0.1469	-0.2856	-0.2602	-0.2899
2	-0.1415	-0.3296	-0.3710	-0.4378
3	-0.2346	-0.2581	-0.2857	-0.3567
4	0.2658	0.2556	-0.5995	-0.4080
5	-0.2112	-0.2973	-0.3187	-0.4268
6	0.0047	-0.1240	-0.4080	-0.4557
7	-0.3589	-0.2970	-0.3692	-0.2411
8	-0.0254	-0.0585	-0.3326	-0.3426
9	-0.1227	-0.1792	0.3406	-0.2498
10	-0.1002	-0.0772	-0.1167	-0.1925
11	-0.2392	-0.0933	-0.3719	-0.3881
<b>mean</b>	<b>-0.1191</b>	<b>-0.1586</b>	<b>-0.2812</b>	<b>-0.3445</b>

## CHAPTER 5

### CONCLUSIONS

#### 5.1 Motivations

Radiotherapy involves the use of radiation to the cancer volume for killing or reducing the size of cancer. Radiotherapy is one of most powerful treatments together with surgery and chemotherapy, but inaccurate determination of the target volume for the radiation delivery can cause injury to the health tissue surrounding the cancer area.

In medical image processing, the precise extraction of lung tumor through segmentation is an essential step to increase the efficiency of cancer treatment and reduce the damage to the normal tissue during radiation treatment. Also, correct image segmentation helps clinical experts examine the anatomy and structure and to determine the disease progress. Moreover, accurate estimation of inter-phase breathing motion in the 4-D lung CT is an important task in radiotherapy treatment since the measurement of mechanical properties which are computed from lung motion estimation can lead to interpret the pulmonary function information. With the 3-D lung CT scanning, respiratory lung motion can cause severe anatomical distortion during free breathing. These motion artifacts along the motion of organ or tumor regions can misplace the exact location of target volumes and lead to the risk of radiation injury to health tissues during radiation treatment. 4-D lung CT imaging can be acquired providing the motion of organ and tumor and reducing the motion artifacts. This thesis has contributed to both of these areas.

## 5.2 Contributions

3-D image segmentation via graph-cuts has previously been proposed, but to date little attention has been paid to how the free parameters should be set and how these affect error metrics. We performed a strict comparison of automated segmentations with expert traced boundaries and proposed empirical rules regarding how to set these parameters for 3-D CT lung segmentation for accurate results. Moreover, we developed a robust tool for performing volumetric and temporal analysis of nodules from respiratory gated 4-D CT. The method is accurate and performs 4-D segmentation and tracking under ten minutes. As a result, the volume of nodules through time can easily be determined.

Despite the fact that the image resolution of 4-D CT data is significantly worse than the publicly available 3-D CT data (e.g., the LIDC data set), in comparison to prior 3-D CT studies, the validation results proved utility of the proposed approach. The algorithm performs graph-cuts segmentation with signed distance ASM. Signed distance ASM provides the shape prior information which prevents the unwanted surrounding tissue from merging with the segmented object. The technical novelty of the proposed approach is two folds: one is use of adaptive shape prior during the graph-cuts segmentation which helps more accurately approximate nodule shape in the test data and secondly use of motion information which warps the mean shape to successive phases of the respiratory cycle. It is expected that the same framework will be applicable to other image segmentation problems including 4-D cardiovascular images. Accurate estimation of inter-phase breathing motion in the lung from 4-D lung CT imaging is an important task in radiotherapy treatment. For motion tracking, deformable image registration (DIR) methods find lung motions.

We computed inter-phase (Phase 10 to Phase 50) motion fields via B-spline registration from 4-D CT data and calculated principal strain values in the lung region. We obtained the principal strain values,  $\lambda_1$ ,  $\lambda_2$ , and  $\lambda_3$ , the principal strain vectors,  $V_1$ ,  $V_2$ , and  $V_3$ , and Jacobian  $J$  from lung deformation from calculated motion fields on 4-D CT data for all 20 subjects and analyze the aspect of regional mechanics over five lung lobes. Among five lobes of the lungs, the right lower and the left lower lobes of the lungs have smaller Jacobian values

meaning that there is more contraction. Moreover, maximum strain value  $\lambda_1$  exhibits larger values on the lower right and the lower left lobes of the lungs. We determined how principal strains of deformation computed from 4-D CT data were correlated with both  $V_{SPECT}$  and  $Q_{SPECT}$  scans in 11 patients. The correlation value  $\rho$  between Jacobian and both SPECT images yielded the highest correlation and among principal strain values, the  $\rho$  for  $\lambda_3$  showed higher correlation with both SPECT images than the other strain values.

### 5.3 Future Research

The accurate interpretation of lung region and lung tumor volumes provides a useful guideline for the radiotherapy planning to reduce the risk of radiation injury to the normal tissues. The proposed segmentation method provides a good solution for the extraction of targeted volumes from pulmonary region, nevertheless there is a limitation for the precise interpretation of the tumor region : Lack of functional information from CT data. Positron emission tomography (PET) is nuclear functional imaging which is usually used for clinical oncology. After uptake of radiotracers fluorodeoxyglucose ( $^{18}\text{F}$ -FDG), these become the marker of glucose metabolism, since cells in the body metabolize the glucose energy, if PET observe high intensities on the specific organ or parts, it indicates that those areas have high metabolic activity, for example, the brain or cancer regions. Through monitoring glucose metabolism by PET scanning, it gives the exact location of tumors. Since CT imaging includes anatomical details, including PET and CT will lead to improved tumor detection and segmentation.

The measurement of regional lung functions from 4-D CT data reported in this thesis also has some limitations : 1) The co-registration between CT and SPECT. During co-registration, loss of original image information is inevitable. However, SPECT/CT scanning obtains SPECT and CT imaging and merged together. The registration step is not needed and the more precise match of SPECT and CT would be possible. Moreover, the interpretation of small regions like tiny tumor or the joint of bones is sometimes hard to detect from functional imaging alone due to low resolution and ambiguous geometrical target location.

SPECT/CT scanning can provide the confident guideline to determine the target location.

2) Roughly sectioned five lung lobes. We approximately separated five lung lobes based on the voxel location from the coronal orientation of lung images. Anatomically, actual lung lobes are located oblique to one another. With more accurate segmentation based on lung lobes to isolate the lung lobes, the analysis of regional lung functions over five lung lobes would be more accurate.

For the diagnosis of tumor, it is important to find out the tumor is benign (non-cancerous) or malignant (cancerous). The determination whether benign or malignant is usually performed by a biopsy procedure. Since each type of tumor has specific character, for example, the growth rate, the way of metastasis, the shape of cancer cell, the diagnosis via the medical image interpretation can be considered as a good approach without a biopsy procedure. From 4-D CT imaging, the analysis for the aspect of regional mechanics from the lung deformation showed through different respiratory phases in this thesis. Considering the different features of tumor deformation with normal tissues during the respiratory cycle with calculating the regional mechanics of tumor region, we can make an attempt to the detection of tumor location and the determination of tumor types.

These future studies and our proposed segmentation will provide better guidance for clinical treatments through accurate medical image interpretation of pulmonary region using respiratory information from 4-D CT data.

## REFERENCES

- [1] Empire10 challenge results.
- [2] Rolf Adams and Leanne Bischof. Seeded region growing. *Pattern Analysis and Machine Intelligence, IEEE Transactions on*, 16(6):641–647, 1994.
- [3] Richard K Albert, Stephen G Spiro, James R Jett, et al. *Comprehensive respiratory medicine*. Mosby International Ltd, 1999.
- [4] Amir A Amini, Yasheng Chen, Rupert W Curwen, Vaidy Mani, and Jean Sun. Coupled b-snake grids and constrained thin-plate splines for analysis of 2-d tissue deformations from tagged mri. *IEEE Transactions on Medical Imaging*, 17(3):344–356, 1998.
- [5] Christoph Bernhard Hoog Antink, Tarunraj Singh, Puneet Singla, and Matthew Podgorsak. Evaluation of advanced Lukas-Kanade optical flow on thoracic 4D-CT. *Journal of clinical monitoring and computing*, 27(4):433–441, 2013.
- [6] Samuel G Armato and William F Sensakovic. Automated lung segmentation for thoracic ct: impact on computer-aided diagnosis1. *Academic Radiology*, 11(9):1011–1021, 2004.
- [7] Armato III, Samuel G., McLennan, Geoffrey, Bidaut, Luc, McNitt-Gray, Michael F., Meyer, Charles R., Reeves, Anthony P., Clarke, Laurence P. et al. Data From LIDC-IDRI. The Cancer Imaging Archive. <http://doi.org/10.7937/K9/TCIA.2015.L09QL9SX>, 2015.
- [8] Brian B Avants, Charles L Epstein, Murray Grossman, and James C Gee. Symmetric diffeomorphic image registration with cross-correlation: evaluating automated labeling of elderly and neurodegenerative brain. *Medical image analysis*, 12(1):26–41, 2008.

- [9] Brian B Avants, Nick Tustison, and Gang Song. Advanced normalization tools (ants). *Insight j*, 2:1–35, 2009.
- [10] Pawel Badura and Ewa Pietka. Soft computing approach to 3D lung nodule segmentation in CT. *Computers in biology and medicine*, 53:230–243, 2014.
- [11] John L Barron, David J Fleet, and Steven S Beauchemin. Performance of optical flow techniques. *International journal of computer vision*, 12(1):43–77, 1994.
- [12] Reinhard Beichel, Alexander Bornik, Christian Bauer, and Erich Sorantin. Liver segmentation in contrast enhanced CT data using graph cuts and interactive 3D segmentation refinement methods. *Medical physics*, 39(3):1361–1373, 2012.
- [13] Andrew Blake, Carsten Rother, Matthew Brown, Patrick Perez, and Philip Torr. Interactive image segmentation using an adaptive gmmrf model. In *Computer Vision-ECCV 2004*, pages 428–441. Springer, 2004.
- [14] Vlad Boldea, Gregory C Sharp, Steve B Jiang, and David Sarrut. 4d-ct lung motion estimation with deformable registration: quantification of motion nonlinearity and hysteresis. *Medical physics*, 35(3):1008–1018, 2008.
- [15] Fred L. Bookstein. Principal warps: Thin-plate splines and the decomposition of deformations. *IEEE Transactions on Pattern Analysis & Machine Intelligence*, 11(6):567–585, 1989.
- [16] Y. Boykov and V. Kolmogorov. Computing geodesics and minimal surfaces via graph cuts. In *Computer Vision, 2003. Proceedings. Ninth IEEE International Conference on*, pages 26–33 vol.1, Oct 2003.
- [17] Y. Boykov and V. Kolmogorov. An experimental comparison of min-cut/max- flow algorithms for energy minimization in vision. *Pattern Analysis and Machine Intelligence, IEEE Transactions on*, 26(9):1124–1137, Sept 2004.

- [18] Y. Boykov, O. Veksler, and R. Zabih. Markov random fields with efficient approximations. In *Computer Vision and Pattern Recognition, 1998. Proceedings. 1998 IEEE Computer Society Conference on*, pages 648–655, Jun 1998.
- [19] Y. Boykov, O. Veksler, and R. Zabih. Fast approximate energy minimization via graph cuts. *Pattern Analysis and Machine Intelligence, IEEE Transactions on*, 23(11):1222–1239, Nov 2001.
- [20] Yuri Boykov and Gareth Funka-Lea. Optimal object extraction via constrained graph-cuts. *International Journal of Computer Vision (IJCV)*, 2004.
- [21] Yuri Boykov, Vladimir Kolmogorov, Daniel Cremers, and Andrew Delong. *An integral solution to surface evolution PDEs via geo-cuts*. Springer, 2006.
- [22] Yuri Boykov and Olga Veksler. Graph cuts in vision and graphics: Theories and applications. In *Handbook of mathematical models in computer vision*, pages 79–96. Springer, 2006.
- [23] Y.Y. Boykov and M.-P. Jolly. Interactive graph cuts for optimal boundary and region segmentation of objects in n-d images. In *Computer Vision, 2001. ICCV 2001. Proceedings. Eighth IEEE International Conference on*, volume 1, pages 105–112 vol.1, 2001.
- [24] Matthieu Bray, Pushmeet Kohli, and Philip HS Torr. Posecut: Simultaneous segmentation and 3d pose estimation of humans using dynamic graph-cuts. In *Computer Vision–ECCV 2006*, pages 642–655. Springer, 2006.
- [25] Andrés Bruhn, Joachim Weickert, and Christoph Schnörr. Lucas/kanade meets horn/schunck: Combining local and global optic flow methods. *International Journal of Computer Vision*, 61(3):211–231, 2005.
- [26] Kunlin Cao, Kaifang Du, Kai Ding, Joseph M Reinhardt, and Gary E Christensen. Regularized nonrigid registration of lung CT images by preserving tissue volume and vesselness measure. *Grand Challenges in Medical Image Analysis*, 2010.

- [27] Edward Castillo, Richard Castillo, Josue Martinez, Maithili Shenoy, and Thomas Guerrero. Four-dimensional deformable image registration using trajectory modeling. *Physics in medicine and biology*, 55(1):305, 2009.
- [28] Richard Castillo, Edward Castillo, Josue Martinez, and Thomas Guerrero. Ventilation from four-dimensional computed tomography: density versus jacobian methods. *Physics in medicine and biology*, 55(16):4661, 2010.
- [29] Jungwon Cha, Neal Dunlap, Brian Wang, and Amir Amini. 3D segmentation of lung CT data with graph-cuts: analysis of parameter sensitivities. In *SPIE Medical Imaging*, pages 97882O–97882O. International Society for Optics and Photonics, 2016.
- [30] Jungwon Cha, Mohammad M. Farhangi, Neal Dunlap, and Amir Amini. 4D Lung Tumor Segmentation via Shape Prior and Motion Cues. In *IEEE EMBS Conference, Gainesville, FL*, 2016.
- [31] Jungwon Cha, Mohammad Mehdi Farhangi, Neal Dunlap, and Amir A Amini. Segmentation and tracking of lung nodules via graph-cuts incorporating shape prior and motion from 4D CT. *Medical physics*, 45(1):297–306, 2018.
- [32] Jungwon Cha, Brian Wang, Neal Dunlap, and Amir Amini. 3D segmentation of lung CT data with graph-cuts: analysis of parameter sensitivities. In *SPIE Medical Imaging, San Diego, CA*, 2016.
- [33] Jian Chen and Amir A Amini. Quantifying 3-d vascular structures in mra images using hybrid pde and geometric deformable models. *Medical Imaging, IEEE Transactions on*, 23(10):1251–1262, 2004.
- [34] Xinjian Chen and Ulas Bagci. 3D automatic anatomy segmentation based on iterative graph-cut-ASM. *Medical physics*, 38(8):4610–4622, 2011.
- [35] Vincent Chu and Ghassan Hamarneh. MATLAB-ITK interface for medical image filtering, segmentation, and registration. In *Proc. SPIE*, volume 6144, pages 61443T–1, 2006.

- [36] Laurent D Cohen and Ron Kimmel. Global minimum for active contour models: A minimal path approach. *International journal of computer vision*, 24(1):57–78, 1997.
- [37] Timothy F Cootes, Christopher J Taylor, David H Cooper, and Jim Graham. Active shape models-their training and application. *Computer vision and image understanding*, 61(1):38–59, 1995.
- [38] Martha M Coselmon, James M Balter, Daniel L McShan, and Marc L Kessler. Mutual information based ct registration of the lung at exhale and inhale breathing states using thin-plate splines. *Medical physics*, 31(11):2942–2948, 2004.
- [39] Ingemar J Cox, Satish B Rao, and Yu Zhong. “ratio regions”: a technique for image segmentation. In *Pattern Recognition, 1996., Proceedings of the 13th International Conference on*, volume 2, pages 557–564. IEEE, 1996.
- [40] Daniel Cremers. Image segmentation with shape priors: Explicit versus implicit representations. *Handbook of Mathematical Methods in Imaging*, pages 1909–1944, 2015.
- [41] William R Crum, Thomas Hartkens, and DLG Hill. Non-rigid image registration: theory and practice. *The British Journal of Radiology*, 2014.
- [42] Carl De Boor. On calculating with b-splines. *Journal of Approximation theory*, 6(1):50–62, 1972.
- [43] Jamshid Dehmeshki, Hamdan Amin, Manlio Valdivieso, and Xujiong Ye. Segmentation of pulmonary nodules in thoracic CT scans: a region growing approach. *Medical Imaging, IEEE Transactions on*, 27(4):467–480, 2008.
- [44] EA Dinic. Algorithm for solution of a problem of maximum flow in a network with power estimation, soviet math. doll. 11 (5), 1277-1280,(1970). *English translation by RF. Rinehart*, 1970.

- [45] Masahiro Endo, Takanori Tsunoo, Susumu Kandatsu, Shuji Tanada, Hiroshi Aradate, and Yasuo Saito. Four-dimensional computed tomography (4D CT)-concepts and preliminary development. *Radiation medicine*, 21(1):17–22, 2003.
- [46] Alexandre X Falcão, Jayaram K Udupa, Supun Samarasekera, Shoba Sharma, Bruce Elliot Hirsch, and Roberto de A Lotufo. User-steered image segmentation paradigms: Live wire and live lane. *Graphical models and image processing*, 60(4):233–260, 1998.
- [47] Amal A Farag, Hossam E Abd El Munim, James H Graham, and Aly A Farag. A novel approach for lung nodules segmentation in chest CT using level sets. *IEEE Transactions on Image Processing*, 22(12):5202–5213, 2013.
- [48] M Mehdi Farhangi, Hichem Frigui, Albert Seow, and Amir A Amini. 3D Active Contour Segmentation Based on Sparse Linear Combination of Training Shapes (SCoTS). *IEEE Transactions on Medical Imaging*, in press, DOI:10.1109/TMI.2017.2720119, 36(11), Nov 2017.
- [49] Lester R Ford and Delbert R Fulkerson. Maximal flow through a network. *Canadian journal of Mathematics*, 8(3):399–404, 1956.
- [50] Daniel Freedman and Tao Zhang. Interactive graph cut based segmentation with shape priors. In *Computer Vision and Pattern Recognition, 2005. CVPR 2005. IEEE Computer Society Conference on*, volume 1, pages 755–762. IEEE, 2005.
- [51] Gareth Funka-Lea, Yuri Boykov, Charles Florin, M-P Jolly, Romain Moreau-Gobard, Rana Ramaraj, and Daniel Rinck. Automatic heart isolation for CT coronary visualization using graph-cuts. In *Biomedical Imaging: Nano to Macro, 2006. 3rd IEEE International Symposium on*, pages 614–617. IEEE, 2006.
- [52] Ben Glocker, Nikos Komodakis, Georgios Tziritas, Nassir Navab, and Nikos Paragios. Dense image registration through mrfs and efficient linear programming. *Medical image analysis*, 12(6):731–741, 2008.

- [53] Andrew V Goldberg and Robert E Tarjan. A new approach to the maximum-flow problem. *Journal of the ACM (JACM)*, 35(4):921–940, 1988.
- [54] Leo Grady. Random walks for image segmentation. *Pattern Analysis and Machine Intelligence, IEEE Transactions on*, 28(11):1768–1783, 2006.
- [55] D. M. Greig, B. T. Porteous, and A. H. Seheult. Exact maximum a posteriori estimation for binary images. *Journal of the Royal Statistical Society. Series B (Methodological)*, 51(2):pp. 271–279, 1989.
- [56] Damien Grosgeorge, Caroline Petitjean, J-N Dacher, and Su Ruan. Graph cut segmentation with a statistical shape model in cardiac MRI. *Computer Vision and Image Understanding*, 117(9):1027–1035, 2013.
- [57] Richard Hamming. *Numerical methods for scientists and engineers*. Courier Corporation, 2012.
- [58] Fiona Hegi-Johnson, Paul Keall, Jeff Barber, Chuong Bui, and John Kipritidis. Evaluating the Accuracy of 4D-CT Ventilation Imaging: First Comparison with Technegas SPECT Ventilation. *Medical Physics*, 2017.
- [59] Francis B Hildebrand. *Methods of applied mathematics*. Courier Corporation, 2012.
- [60] Derek LG Hill, Philipp G Batchelor, Mark Holden, and David J Hawkes. Medical image registration. *Physics in medicine and biology*, 46(3):R1, 2001.
- [61] Derek LG Hill, David J Hawkes, JE Crossman, MJ Gleeson, TCS Cox, EECML Bracey, AJ Strong, and P Graves. Registration of mr and ct images for skull base surgery using point-like anatomical features. *The British journal of radiology*, 64(767):1030–1035, 1991.
- [62] SA Hojjatoleslami and Josef Kittler. Region growing: a new approach. *IEEE Transactions on Image processing*, 7(7):1079–1084, 1998.

- [63] Berthold K Horn and Brian G Schunck. Determining optical flow. In *1981 Technical symposium east*, pages 319–331. International Society for Optics and Photonics, 1981.
- [64] N Howlader, AM Noone, M Krapcho, J Garshell, N Neyman, SF Altekruse, C Kosary, M Yu, J Ruhl, Z Tatalovich, et al. Seer cancer statistics review, 1975-2010.[based on the november 2012 seer data submission, posted to the seer web site, april 2013.]. *Bethesda, MD: National Cancer Institute*, 2013.
- [65] Shiyong Hu, Eric A Hoffman, and Joseph M Reinhardt. Automatic lung segmentation for accurate quantitation of volumetric x-ray ct images. *Medical Imaging, IEEE Transactions on*, 20(6):490–498, 2001.
- [66] Jiantao Huang, Dana Abendschein, Victor G Davila-Roman, and Amir A Amini. Spatio-temporal tracking of myocardial deformations with a 4-d b-spline model from tagged mri. *Medical Imaging, IEEE Transactions on*, 18(10):957–972, 1999.
- [67] Hugo, Geoffrey D., Weiss, Elisabeth, Sleeman, William C., Balik, Salim, Keall, Paul J., Lu, Jun, and Williamson, Jeffrey F. . Data from 4D Lung Imaging of NSCLC Patients. The Cancer Imaging Archive. <http://doi.org/10.7937/K9/TCIA.2016.ELN8YGLE>, 2016.
- [68] Mohamed Hussein, Amitabh Varshney, and Larry Davis. On implementing graph cuts on cuda. In *First Workshop on General Purpose Processing on Graphics Processing Units*, volume 2007, 2007.
- [69] Hiroshi Ishikawa. Exact optimization for markov random fields with convex priors. *Pattern Analysis and Machine Intelligence, IEEE Transactions on*, 25(10):1333–1336, 2003.
- [70] Hiroshi Ishikawa and Davi Geiger. Segmentation by grouping junctions. In *Computer Vision and Pattern Recognition, 1998. Proceedings. 1998 IEEE Computer Society Conference on*, pages 125–131. IEEE, 1998.

- [71] Ian H Jermyn and Hiroshi Ishikawa. Globally optimal regions and boundaries. In *Computer Vision, 1999. The Proceedings of the Seventh IEEE International Conference on*, volume 2, pages 904–910. IEEE, 1999.
- [72] Olivier Juan and Yuri Boykov. Active graph cuts. In *Computer Vision and Pattern Recognition, 2006 IEEE Computer Society Conference on*, volume 1, pages 1023–1029. IEEE, 2006.
- [73] Sven Kabus and Cristian Lorenz. Fast elastic image registration. *Medical Image Analysis for the Clinic: A Grand Challenge*, pages 81–89, 2010.
- [74] Michael Kass, Andrew Witkin, and Demetri Terzopoulos. Snakes: Active contour models. *International journal of computer vision*, 1(4):321–331, 1988.
- [75] Paul Keall. 4-dimensional computed tomography imaging and treatment planning. In *Seminars in radiation oncology*, volume 14, pages 81–90. Elsevier, 2004.
- [76] Pushmeet Kohli and Philip HS Torr. Efficiently solving dynamic markov random fields using graph cuts. In *Computer Vision, 2005. ICCV 2005. Tenth IEEE International Conference on*, volume 2, pages 922–929. IEEE, 2005.
- [77] Vladimir Kolmogorov and Yuri Boykov. What metrics can be approximated by geo-cuts, or global optimization of length/area and flux. In *Computer Vision, 2005. ICCV 2005. Tenth IEEE International Conference on*, volume 1, pages 564–571. IEEE, 2005.
- [78] Vladimir Kolmogorov, Antonio Criminisi, Andrew Blake, Geoffrey Cross, and Carsten Rother. Bi-layer segmentation of binocular stereo video. In *Computer Vision and Pattern Recognition, 2005. CVPR 2005. IEEE Computer Society Conference on*, volume 2, pages 407–414. IEEE, 2005.
- [79] Vladimir Kolmogorov and Ramin Zabini. What energy functions can be minimized via graph cuts? *Pattern Analysis and Machine Intelligence, IEEE Transactions on*, 26(2):147–159, 2004.

- [80] William J Kostis, Anthony P Reeves, David F Yankelevitz, and Claudia I Henschke. Three-dimensional segmentation and growth-rate estimation of small pulmonary nodules in helical CT images. *IEEE transactions on medical imaging*, 22(10):1259–1274, 2003.
- [81] M.E. Leventon, W.E.L. Grimson, and O. Faugeras. Statistical shape influence in geodesic active contours. In *Computer Vision and Pattern Recognition, 2000. Proceedings. IEEE Conference on*, volume 1, pages 316–323 vol.1, 2000.
- [82] Baojun Li, Gary E Christensen, Eric A Hoffman, Geoffrey McLennan, and Joseph M Reinhardt. Establishing a normative atlas of the human lung: intersubject warping and registration of volumetric ct images. *Academic Radiology*, 10(3):255–265, 2003.
- [83] Kang Li, Xiaodong Wu, Danny Z Chen, and Milan Sonka. Optimal surface segmentation in volumetric images—a graph-theoretic approach. *Pattern Analysis and Machine Intelligence, IEEE Transactions on*, 28(1):119–134, 2006.
- [84] Yin Li, Jian Sun, and Heung-Yeung Shum. Video object cut and paste. *ACM Transactions on Graphics (TOG)*, 24(3):595–600, 2005.
- [85] Marius George Linguraru, John A Pura, Vivek Pamulapati, and Ronald M Summers. Statistical 4D graphs for multi-organ abdominal segmentation from multiphase CT. *Medical image analysis*, 16(4):904–914, 2012.
- [86] Dirk Loeckx, Pieter Slagmolen, Frederik Maes, Dirk Vandermeulen, and Paul Suetens. Nonrigid image registration using conditional mutual information. *Medical Imaging, IEEE Transactions on*, 29(1):19–29, 2010.
- [87] Herve Lombaert, Yiyong Sun, Leo Grady, and Chenyang Xu. A multilevel banded graph cuts method for fast image segmentation. In *Computer Vision, 2005. ICCV 2005. Tenth IEEE International Conference on*, volume 1, pages 259–265. IEEE, 2005.

- [88] Weiguo Lu, Ming-Li Chen, Gustavo H Olivera, Kenneth J Ruchala, and Thomas R Mackie. Fast free-form deformable registration via calculus of variations. *Physics in Medicine and Biology*, 49(14):3067, 2004.
- [89] Bruce D Lucas, Takeo Kanade, et al. An iterative image registration technique with an application to stereo vision. In *IJCAI*, volume 81, pages 674–679, 1981.
- [90] Frederik Maes, Andre Collignon, Dirk Vandermeulen, Guy Marchal, and Paul Suetens. Multimodality image registration by maximization of mutual information. *Medical Imaging, IEEE Transactions on*, 16(2):187–198, 1997.
- [91] Gig S Mageras, Alex Pevsner, Ellen D Yorke, Kenneth E Rosenzweig, Eric C Ford, Agung Hertanto, Steven M Larson, D Michael Lovelock, Yusuf E Erdi, Sadek A Nehmeh, et al. Measurement of lung tumor motion using respiration-correlated ct. *International Journal of Radiation Oncology\* Biology\* Physics*, 60(3):933–941, 2004.
- [92] JB Antoine Maintz and Max A Viergever. A survey of medical image registration. *Medical image analysis*, 2(1):1–36, 1998.
- [93] Alan P Mangan and Ross T Whitaker. Partitioning 3d surface meshes using watershed segmentation. *Visualization and Computer Graphics, IEEE Transactions on*, 5(4):308–321, 1999.
- [94] Laurent Massoptier and Sergio Casciari. Fully automatic liver segmentation through graph-cut technique. In *2007 29th Annual International Conference of the IEEE Engineering in Medicine and Biology Society*, pages 5243–5246. IEEE, 2007.
- [95] Tim McInerney and Demetri Terzopoulos. A dynamic finite element surface model for segmentation and tracking in multidimensional medical images with application to cardiac 4d image analysis. *Computerized Medical Imaging and Graphics*, 19(1):69–83, 1995.

- [96] Nihad Mesanovic, Mislav Grgic, Haris Huseinagic, Matija Males, Emir Skejic, and Muamer Smajlovic. Automatic ct image segmentation of the lungs with region growing algorithm. In *18th International Conference on Systems, Signals and Image Processing-IWSSIP*, pages 395–400, 2011.
- [97] Temesguen Messay, Russell C Hardie, and Timothy R Tuinstra. Segmentation of pulmonary nodules in computed tomography using a regression neural network approach and its application to the lung image database consortium and image database resource initiative dataset. *Medical image analysis*, 22(1):48–62, 2015.
- [98] Charles R Meyer, Jennifer L Boes, Boklye Kim, Peyton H Bland, Kenneth R Zasadny, Paul V Kison, Kenneth Koral, Kirk A Frey, and Richard L Wahl. Demonstration of accuracy and clinical versatility of mutual information for automatic multimodality image fusion using affine and thin-plate spline warped geometric deformations. *Medical image analysis*, 1(3):195–206, 1997.
- [99] Eric N Mortensen and William A Barrett. Interactive segmentation with intelligent scissors. *Graphical models and image processing*, 60(5):349–384, 1998.
- [100] Michael E. Mortenson. *Geometric Modeling*. John Wiley & Sons, Inc., New York, NY, USA, 1985.
- [101] Keelin Murphy, Bram Van Ginneken, J Reinhardt, Sven Kabus, Kai Ding, Xiang Deng, and J Pluim. Evaluation of methods for pulmonary image registration: The empire10 study. *Grand Challenges in Medical Image Analysis*, 2010, 2010.
- [102] Keelin Murphy, Bram Van Ginneken, Joseph M Reinhardt, Sven Kabus, Kai Ding, Xiang Deng, Kunlin Cao, Kaifang Du, Gary E Christensen, Vincent Garcia, et al. Evaluation of registration methods on thoracic CT: the EMPIRE10 challenge. *IEEE transactions on medical imaging*, 30(11):1901–1920, 2011.
- [103] Keelin Murphy, Bram van Ginneken, Arnold MR Schilham, BJ De Hoop, HA Gietema, and Mathias Prokop. A large-scale evaluation of automatic pulmonary nodule detection

- in chest CT using local image features and k-nearest-neighbour classification. *Medical image analysis*, 13(5):757–770, 2009.
- [104] Keita Nakagomi, Akinobu Shimizu, Hidefumi Kobatake, Masahiro Yakami, Koji Fujimoto, and Kaori Togashi. Multi-shape graph cuts with neighbor prior constraints and its application to lung segmentation from a chest CT volume. *Medical image analysis*, 17(1):62–77, 2013.
- [105] Mohammadreza Negahdar. *The technical underpinnings of Graph cuts and its applications to segmentation of anatomical objects from medical images*. University of Louisville, 2009.
- [106] Mohammadreza Negahdar, Neal Dunlap, Albert Zacarias, A Cahid Civelek, Shiao Y Woo, and Amir A Amini. Comparison of indices of regional lung function from 4-D X-ray CT: Jacobian vs. strain of deformation. In *Biomedical Imaging (ISBI), 2013 IEEE 10th International Symposium on*, pages 648–651. IEEE, 2013.
- [107] U.S. National Institutes of Health. National Cancer Institute. State cancer profiles, <http://statecancerprofiles.cancer.gov>.
- [108] Francisco PM Oliveira and João Manuel RS Tavares. Medical image registration: a review. *Computer methods in biomechanics and biomedical engineering*, 17(2):73–93, 2014.
- [109] David Ost, Alan M Fein, and Steven H Feinsilver. The solitary pulmonary nodule. *New England Journal of Medicine*, 348(25):2535–2542, 2003.
- [110] Tinsu Pan. Comparison of helical and cine acquisitions for 4d-ct imaging with multislice ct. *Medical physics*, 32(2):627–634, 2005.
- [111] Charles A Pelizzari, George TY Chen, Danny R Spelbring, Ralph R Weichselbaum, and Chin-Tu Chen. Accurate three-dimensional registration of ct, pet, and/or mr images of the brain. *Journal of computer assisted tomography*, 13(1):20–26, 1989.

- [112] Josien PW Pluim, JB Antoine Maintz, and Max A Viergever. Mutual-information-based registration of medical images: a survey. *Medical Imaging, IEEE Transactions on*, 22(8):986–1004, 2003.
- [113] Regina Pohle and Klaus D Toennies. Segmentation of medical images using adaptive region growing. In *Medical Imaging 2001*, pages 1337–1346. International Society for Optics and Photonics, 2001.
- [114] Petia Radeva, Amir Amini, Jiantao Huang, and Enric Marti. Deformable b-solids and implicit snakes for localization and tracking of spamm mri-data. In *Mathematical Methods in Biomedical Image Analysis, 1996., Proceedings of the Workshop on*, pages 192–201. IEEE, 1996.
- [115] Petia Radeva, Amir A. Amini, and Jiantao Huang. Deformable b-solids and implicit snakes for 3d localization and tracking of spamm mri data. *Comput. Vis. Image Underst.*, 66(2):163–178, May 1997.
- [116] Anthony P Reeves, Antoni B Chan, David F Yankelevitz, Claudia I Henschke, Bryan Kressler, and William J Kostis. On measuring the change in size of pulmonary nodules. *IEEE transactions on medical imaging*, 25(4):435–450, 2006.
- [117] Eike Rietzel, Tinsu Pan, and George TY Chen. Four-dimensional computed tomography: image formation and clinical protocol. *Medical physics*, 32(4):874–889, 2005.
- [118] Paul J Roach, Geoffrey P Schembri, and Dale L Bailey. V/q scanning using spect and spect/ct. *Journal of Nuclear Medicine*, 54(9):1588–1596, 2013.
- [119] Carsten Rother, Vladimir Kolmogorov, and Andrew Blake. Grabcut -interactive foreground extraction using iterated graph cuts. *ACM Transactions on Graphics (SIGGRAPH)*, August 2004.
- [120] Sébastien Roy and Ingemar J Cox. A maximum-flow formulation of the n-camera stereo correspondence problem. In *Computer Vision, 1998. Sixth International Conference on*, pages 492–499. IEEE, 1998.

- [121] Daniel Rueckert, Luke I Sonoda, Carmel Hayes, Derek LG Hill, Martin O Leach, and David J Hawkes. Nonrigid registration using free-form deformations: application to breast mr images. *IEEE transactions on medical imaging*, 18(8):712–721, 1999.
- [122] Jan Ruhaak, Thomas Polzin, Stefan Heldmann, Ivor Simpson, Heinz Handels, Jan Modersitzki, and Mattias Paul Heinrich. Estimation of Large Motion in Lung CT by Integrating Regularized Keypoint Correspondences into Dense Deformable Registration. *IEEE Transactions on Medical Imaging*, 2017.
- [123] Jianbo Shi and Jitendra Malik. Normalized cuts and image segmentation. *Pattern Analysis and Machine Intelligence, IEEE Transactions on*, 22(8):888–905, 2000.
- [124] Rushin Shojaii, Javad Alirezaie, and Paul Babyn. Automatic lung segmentation in ct images using watershed transform. In *Image Processing, 2005. ICIP 2005. IEEE International Conference on*, volume 2, pages II–1270. IEEE, 2005.
- [125] Greg Slabaugh and Gozde Unal. Graph cuts segmentation using an elliptical shape prior. In *Image Processing, 2005. ICIP 2005. IEEE International Conference on*, volume 2, pages II–1222. IEEE, 2005.
- [126] Dan Snow, Paul Viola, and Ramin Zabih. Exact voxel occupancy with graph cuts. In *Computer Vision and Pattern Recognition, 2000. Proceedings. IEEE Conference on*, volume 1, pages 345–352. IEEE, 2000.
- [127] American Cancer Society. What is non-small cell lung cancer?, <http://www.cancer.org/cancer/lungcancer-non-smallcell/detailedguide/non-small-cell-lung-cancer-what-is-non-small-cell-lung-cancer>.
- [128] Gang Song, Nicholas Tustison, Brian Avants, and James C Gee. Lung ct image registration using diffeomorphic transformation models. *Medical image analysis for the clinic: a grand challenge*, pages 23–32, 2010.

- [129] Milan Sonka and J Michael Fitzpatrick. Handbook of medical imaging(volume 2, medical image processing and analysis). In *Handbook of medical imaging*, pages 449–506. SPIE- The international society for optical engineering, 2000.
- [130] Xuejun Sun, Haibo Zhang, and Huichuan Duan. 3d computerized segmentation of lung volume with computed tomography. *Academic radiology*, 13(6):670–677, 2006.
- [131] Scott J Swanson, Michael T Jaklitsch, Steven J Mentzer, Raphael Bueno, Jeanne M Lukanich, and David J Sugarbaker. Management of the solitary pulmonary nodule: role of thoracoscopy in diagnosis and therapy. *CHEST Journal*, 116(suppl\_3):523S–524S, 1999.
- [132] Varian Medical Systems. Real-time position management (rpm) - varian medical systems, Jun 2016.
- [133] Bethany B Tan, Kevin R Flaherty, Ella A Kazerooni, and Mark D Iannettoni. The solitary pulmonary nodule. *Chest Journal*, 123(1\_suppl):89S–96S, 2003.
- [134] Meng Tang, Lena Gorelick, Olga Veksler, and Yuri Boykov. Grabcut in one cut. In *Proceedings of the IEEE International Conference on Computer Vision*, pages 1769–1776, 2013.
- [135] Tommy WH Tang and Albert CS Chung. Non-rigid image registration using graph-cuts. In *Medical Image Computing and Computer-Assisted Intervention–MICCAI 2007*, pages 916–924. Springer, 2007.
- [136] J-P Thirion. Image matching as a diffusion process: an analogy with maxwell’s demons. *Medical image analysis*, 2(3):243–260, 1998.
- [137] Alain Tremeau and Nathalie Borel. A region growing and merging algorithm to color segmentation. *Pattern recognition*, 30(7):1191–1203, 1997.

- [138] Nicholas J Tustison, Brian B Avants, and James C Gee. Directly manipulated free-form deformation image registration. *Image Processing, IEEE Transactions on*, 18(3):624–635, 2009.
- [139] Jayaram K Udupa and Supun Samarasekera. Fuzzy connectedness and object definition: theory, algorithms, and applications in image segmentation. *Graphical models and image processing*, 58(3):246–261, 1996.
- [140] René WM Underberg, Frank J Lagerwaard, Johan P Cuijpers, Ben J Slotman, John R Van Sörnsen De Koste, and Suresh Senan. Four-dimensional ct scans for treatment planning in stereotactic radiotherapy for stage i lung cancer. *International Journal of Radiation Oncology\* Biology\* Physics*, 60(4):1283–1290, 2004.
- [141] Bram Van Ginneken. Supervised probabilistic segmentation of pulmonary nodules in CT scans. *Medical Image Computing and Computer-Assisted Intervention–MICCAI 2006*, pages 912–919, 2006.
- [142] Jef Vandemeulebroucke, David Sarrut, Patrick Clarysse, et al. The POPI-model, a point-validated pixel-based breathing thorax model. In *XVth international conference on the use of computers in radiation therapy (ICCR)*, volume 2, pages 195–199, 2007.
- [143] Olga Veksler. Image segmentation by nested cuts. In *Computer Vision and Pattern Recognition, 2000. Proceedings. IEEE Conference on*, volume 1, pages 339–344. IEEE, 2000.
- [144] Paul Viola and William M Wells III. Alignment by maximization of mutual information. *International journal of computer vision*, 24(2):137–154, 1997.
- [145] Jue Wang, Pravin Bhat, R Alex Colburn, Maneesh Agrawala, and Michael F Cohen. Interactive video cutout. *ACM Transactions on Graphics (TOG)*, 24(3):585–594, 2005.
- [146] Ted W Way, Lubomir M Hadjiiski, Berkman Sahiner, Heang-Ping Chan, Philip N Cascade, Ella A Kazerooni, Naama Bogot, and Chuan Zhou. Computer-aided diagnosis

- of pulmonary nodules on CT scans: Segmentation and classification using 3D active contours. *Medical Physics*, 33(7):2323–2337, 2006.
- [147] Zhenyu Wu and Richard Leahy. An optimal graph theoretic approach to data clustering: Theory and its application to image segmentation. *Pattern Analysis and Machine Intelligence, IEEE Transactions on*, 15(11):1101–1113, 1993.
- [148] Chenyang Xu and Jerry L Prince. Snakes, shapes, and gradient vector flow. *IEEE Transactions on image processing*, 7(3):359–369, 1998.
- [149] Ziyue Xu, Ulas Bagci, Brent Foster, Awais Mansoor, and Daniel J Mollura. Spatially constrained random walk approach for accurate estimation of airway wall surfaces. In *International Conference on Medical Image Computing and Computer-Assisted Intervention*, pages 559–566. Springer, 2013.
- [150] Tokihiro Yamamoto, Sven Kabus, Cristian Lorenz, Erik Mittra, Julian C Hong, Melody Chung, Neville Eclov, Jacqueline To, Maximilian Diehn, Billy W Loo, et al. Pulmonary ventilation imaging based on 4-dimensional computed tomography: comparison with pulmonary function tests and SPECT ventilation images. *International Journal of Radiation Oncology\* Biology\* Physics*, 90(2):414–422, 2014.
- [151] Xujiang Ye, Gareth Beddoe, and Greg Slabaugh. Automatic graph cut segmentation of lesions in CT using mean shift superpixels. *Journal of Biomedical Imaging*, 2010:19, 2010.
- [152] Youbing Yin, Eric A Hoffman, Kai Ding, Joseph M Reinhardt, and Ching-Long Lin. A cubic b-spline-based hybrid registration of lung ct images for a dynamic airway geometric model with large deformation. *Physics in medicine and biology*, 56(1):203, 2010.
- [153] Li Zhang and Joseph M Reinhardt. 3d pulmonary ct image registration with a standard lung atlas. In *Medical Imaging 2000*, pages 67–77. International Society for Optics and Photonics, 2000.

# CURRICULUM VITAE

NAME : Jungwon Cha

ADDRESS : Medical Imaging Lab,  
Electrical and Computer Engineering Department  
University of Louisville,  
Louisville, KY 40292

EMAIL : j0cha001@louisville.edu

---

## RESEARCH INTERESTS

---

Medical Imaging, Deformable Image Registration, Image Segmentation, Physiologic imaging including assessment of pulmonary mechanics, Image processing.

---

## EDUCATION

---

**Ph.D., University of Louisville**, Louisville, KY USA May 2018

Department of Electrical and Computer Engineering

Advisor: Dr. Amir Amini

Committee Members: Dr. Amir Amini, Dr. Jacek Zurada, Dr. Tamer Inanc, Dr. Hichem Frigui, Dr. Neal Dunlap, and Dr. Brian Wang

Dissertation: Segmentation, Tracking, and Kinematics of Lung Parenchyma and Lung Tumors from 4D CT with Application to Radiation Treatment Planning

**Ph.D. candidate, University of Louisville**, Louisville, KY USA 2015 - 2018

Department of Electrical and Computer Engineering

Advisor: Dr. Amir Amini

**Ph.D. student, University of Louisville**, Louisville, KY USA 2010 -2014

Electrical and Computer engineering Graduate Program

Advisor: Dr. Amir Amini

**M.S., Yonsei University**, South Korea August 2008

Physics Graduate Program

Advisor: Dr. Keun Nahm

Thesis: *Magnetic Susceptibilities of the Single Crystal Nd<sub>3</sub>Se<sub>4</sub>*

**B.S., Yonsei University**, South Korea August 2006

Major: Physics

---

### ACADEMIC HONORS

---

Electrical Engineering Outstanding Graduate Student Award at the J.B. Speed School of Engineering Annual Honors and Awards Program, University of Louisville, KY 2018

Speed School of Engineering Scholarship, University of Louisville, KY 2010

BrainKorea21 Research Fellowship award, Yonsei University, South Korea 2008

---

### PROFESSIONAL EXPERIENCE

---

**Graduate Research Assistant, University of Louisville**, Louisville, KY USA 2014 - 2018

- Software engineer working on development of segmentation of the lung boundary and lung

modules by graph cut method from 3-D or 4-D CT data using MATLAB

- Analyzing 4-D CT and SPECT data to compute regional mechanics in the pulmonary region using MATLAB
- Performing deep learning research for classification of lung tumor malignancy using Python

**Graduate Research Assistant, University of Louisville, Louisville, KY USA** 2010 - 2014

- Performing the phantom studies for 4-D flow MR imaging in the presence of random unsteady and turbulent blood flow distal to a narrowing

**Graduate Teaching Assistant, University of Louisville, Louisville, KY USA**

Spring 2013, Spring 2015, Fall 2016

- ECE618/635, Digital Image Processing
- Assisted students and professor with programming MATLAB for research projects

**Graduate Teaching Assistant, Yonsei University, South Korea** 2006 - 2008

- General Physics
- Assisted students and professor with lectures and laboratories on the basics of measurement, instrumentation, analysis, design and execution of experiments, and written reports

---

## COMPUTER SKILLS

---

Languages: MATLAB, Python, L<sup>A</sup>T<sub>E</sub>X, R

Operating Systems: Windows, Linux

**Jungwon Cha**, Neal Dunlap & Amir A. Amini. Statistical correlation between CT ventilation imaging and SPECT V/Q scans in patients with lung cancer. In *15th IEEE International Symposium on Biomedical Imaging (ISBI), Washington, D.C., April 2018*. (Expanded version in preparation for journal)

**Jungwon Cha**, Alexander Henn, Marcus Stoddard & Amir Amini. 3D segmentation of the ascending and descending aorta from CT data via graph-cuts. In *Society for Photo-optical Instrumentation Engineers (SPIE) Medical Imaging, Houston, TX, pages 105781R. February 2018*.

**Jungwon Cha**, Mohammad Mehdi Farhangi, Neal Dunlap & Amir A. Amini. Segmentation and Tracking of Lung Nodules via Graph-Cuts Incorporating Shape Prior and Motion from 4-D CT. *Medical Physics, 45(1): 297-306. 2018*

**Jung won Cha**, M Mehdi Farhangi, Neal Dunlap, & Amir Amini. Volumetric analysis of respiratory gated whole lung and liver CT data with motion-constrained graph cuts segmentation. In *Engineering in Medicine and Biology Society (EMBC), 39th Annual International Conference of the IEEE, Jeju Island, Korea, pages 3405-3408. IEEE, July 2017*.

**Jungwon Cha**, Mohammad M Farhangi, Neal Dunlap, & Amir Amini. 4D lung tumor segmentation via shape prior and motion cues. In *Engineering in Medicine and Biology Society (EMBC), 38th Annual International Conference of the IEEE, Orlando, FL, pages 1284-1287. IEEE, August 2016*.

**Jungwon Cha**, Neal Dunlap, Brian Wang, & Amir Amini. 3D segmentation of lung CT data with graph-cuts: analysis of parameter sensitivities. In *Society for Photo-optical Instrumentation Engineers (SPIE) Medical Imaging, San Diego, CA, pages 97882O. March 2016*.

Mo Kadbi, MJ Negahdar, **Jungwon Cha**, Melanie Traughber, Peter Martin, Marcus F Stoddard, & Amir A Amini. 4D UTE flow: a phase-contrast MRI technique for assessment and visualization of stenotic flows. *Magnetic resonance in medicine, 73(3):939-950*.

2015.

MJ Negahdar, Mo Kadbi, **J Cha**, J Cebra, & A Amini. Noninvasive 3D pressure calculation from PC-MRI via non-iterative harmonics-based orthogonal projection: constant flow experiment. In *Engineering in Medicine and Biology Society (EMBC), 35th Annual International Conference of the IEEE, Osaka, Japan, pages 4390-4393. IEEE, July 2013.*

Mo Kadbi, MJ Negahdar, **Jungwon Cha**, Melanie Traugber, Peter Martin, & Amir A Amini. Validation of 3D ultra-short TE (UTE) phase-contrast MRI for imaging of steady flow: initial phantom experiments. In *Engineering in Medicine and Biology Society (EMBC), 34th Annual International Conference of the IEEE, San Diego, CA, pages 372-376. IEEE, September 2012.*

MJ Negahdar, **Jungwon Cha**, Mostafa Shakeri, M Kendrick, Motaz Alshaher, Iman Khodarahimi, MK Sharp, A Yancey, J Heidenreich, & A Amini. Effect of Venc on accuracy of velocity profiles in multi-slice phase-contrast MR imaging of stenotic flow. In *9th IEEE International Symposium on Biomedical Imaging (ISBI), Barcelona, Spain, pages 820-823. IEEE, May 2012.*

---

## ABSTRACTS

---

Andrew Justice, Sean Callahan, **Jungwon Cha** & Amir A. Amini. Phase Unwrapping of 4D Flow Data with Graph Cuts. In *2018 International Society for Magnetic Resonance in Medicine (ISMRM), Paris, France, June 2018.*

**Jungwon Cha**, Neal Dunlap, Brian Wang, Shiao Y Woo, & Amir Amini. Heterogeneous pattern of 2D lung deformations revealed through deformable registration of 4D CT data. In *11th IEEE International Symposium on Biomedical Imaging (ISBI), Beijing, China, May 2014.*

MJ Negahdar, M. Kadbi, **J. Cha**, J. Cebal, & A. Amini. A fast 3D non-iterative approach to pressure calculation from PC-MRI: Phantom experiments. In *2013 International Society of Magnetic Resonance in Medicine Annual Meeting (ISMRM), 2013*.